Boundary mixing in non-tidal basins: Observations from the Baltic Sea

Dissertation
zur Erlangung des akademischen Grades
doctor rerum naturalium (Dr. rer. nat.)
der Mathematisch-Naturwissenschaftlichen Fakultät
der Universität Rostock

vorgelegt von
Chris Lappe
aus Rostock

urn:nbn:de:gbv:28-diss2018-0025-6

Gutachter:

1. **Gutachter:**
   PD Dr. Lars Umlauf
   Leibniz Institute for Baltic Sea Research, Warnemünde

2. **Gutachter:**
   Prof. Dr. Lars Arneborg
   Swedish Meteorological and Hydrological Institute, Gothenburg

Datum der Einreichung: 23. August 2017
Datum der Verteidigung: 12. Januar 2018

Abstract

Diapycnal mixing is important to close the overturning circulation in the Baltic Sea and to explain the vertical transport of tracers. This thesis is focused on boundary mixing in a non-tidal basin. This is a diapycnal mixing process that is presently not well understood. The investigations are based on two data sets from the Bornholm Basin (southern Baltic Sea), which were obtained during different seasons and include high-resolution CTD, shear microstructure, and velocity data. In summer, a highly turbulent and strongly stratified bottom boundary layer (BBL) of a few meters thickness develops, which exhibits high mixing rates and a bulk mixing efficiency that is comparable to the interior value of $\Gamma = 0.2$. Near-inertial wave motions were identified as the main energy source for these boundary mixing processes. The contribution of the BBL mixing region to the overall diapycnal mixing and energy dissipation exceeds the contribution of the interior region. However, the BBL turbulence was found to be suppressed within the halocline, and does therefore not contribute to cross-halocline mixing in this region.

In winter, a BBL of similar thickness to the summer situation could be identified, characterized by large bulk mixing efficiencies. Different from the summer situation, the BBL was not suppressed within the halocline and shear-induced turbulence was found to destabilize the halocline close to the sloping walls of the basin, potentially increasing turbulent transport across the halocline in this region. The results of this thesis are likely to be relevant also for other non-tidal system, for example large lakes and inland seas.

Zusammenfassung

Diapyknische Vermischungsprozesse schließen die thermohaline Zirkulation der Ostsee und sind verantwortlich für den vertikalen Transport gelöster Stoffe (Tracer). Diese Arbeit beschäftigt sich mit dem noch wenig verstandenem Aspekt der Randmischung in einem nicht gezeitengetriebenem Becken. Die Untersuchung stützt sich auf zwei zu verschiedenen Jahreszeiten erhobenen Datensätzen aus dem Bornholm Becken (südliche Ostsee), umfasst zeitlich und räumlich hochaufgelöste CTD-Daten sowie Schermikrostruktur- und Geschwindigkeitsmessungen. Im Sommer war die Bodengrenzschicht (BBL) wenige Meter dick und zeichnete sich sowohl durch erhöhte Turbulenz als auch durch erhöhte Mischungsraten aus. Die mittlere Mischungseffizenz der Grenzschicht erreichte dabei einen Wert, der ungefähr dem Wert der internen Mischung $\Gamma = 0.2$ entspricht. Interne Wellen nahe der Trägheitsfrequenz sind die wichtigste Energiequelle für die beobachtete Randmischung. Der in der Grenzschicht geleistete Beitrag zur Energiedissipation und Mischung überstieg jeweils den Beitrag aus dem Innern des Beckens. Im Bereich der Haloklinen jedoch wird die turbulente BBL unterdrückt. Ein Beitrag zur Mischung durch die Halokline leistete die BBL somit nicht. Im Winter ließ sich ebenfalls eine Bodengrenzschicht beobachten, die der BBL des Sommers ähnelte und erhöhte Mischungseffizenzen aufwies. Im Gegensatz zum Sommer fand keine Unterdrückung der BBL in der Haloklinen statt. Zusätzlich erfolgte eine Destabilisierung der Haloklinen durch scherungsbedingte Turbulenz am Beckenrand. Beide Prozesse erhöhten die turbulenten Transportraten durch die Halokline. Die Ergebnisse dieser Untersuchung sind ebenfalls relevant für andere nicht gezeitengetriebene Systeme wie große Seen oder Binnenmeere.

Acknowledgements

This thesis and all the work involved in the completion would still be in process without the support I received from the following women, men and children in the last years and, especially, in the last months before submission.

I especially thank my supervisor Lars Umlauf, who spent so much time to explain oceanographic concepts to me, contributed ideas for data analysis and checked talks, abstracts and presentations. He always found critical aspects and had useful tips. He also made sure that presentations, physical considerations, posters and talk preparations were done properly. His advice and notes not only helped to recognize the story of the paper and this thesis but also improved both writs.

I am grateful for the help of my colleagues Torsten Seifert, who preprocessed the meteorologic data from the DWD, and Eefke van der Lee, who gave me some processed data from the center of the Bornholm Basin. Thanks to the technician Toralf Heene for answering all questions about ADCP and MSS issues and for doing all the re-processing of ADCP data which I requested. I would like to thank Frederic Cyr for all his work related to his stay in Rostock in December 2015. He processed the NIOZ temperature chain data and had so many good ideas. A special thanks goes to Peter Holtermann. I do not know how often I spent time with the processing tools of the MSS profiler to improve the turbulence data close to the bottom or to find features somewhere in the data or processing tools. Nevertheless, it was always a good idea to talk to Peter and to have a cup of coffee or something similar. I like to thank Martin Schmidt and Wolfgang Fennel, who supervised me during my Master program. They helped me to understand some of the most important basics in oceanography. Thanks to Hans Burchard, who continuously had an open door for questions. Thanks to Elisabeth Schulz, Ulf Gräwe, and Knut Klingbeil for these small things that made the job easier. Thanks to all the fantastic persons who shared their office with me in the last years and helped me to create this magic room 214 atmosphere, where questions are always welcome and mostly answered: Johannes Becherer, Kaveh Purkiani, Mahdi Mohammadi-Aragh, Georgy Gevorkov, Merten Siegfried, Selina Müller and Madline Kniebusch. Special thanks to Kirstin Schulz for jointly mastering the PhD time in room 214. She checked my English wordings in presentations and emails and is the only one who has a clue about boundary layers on slopes.

I am deeply appreciative of the support of my family. They took care about all the things I cannot even enumerate. Thanks to Fenja and Alma, who did not care

about work and writing. They brought me down to earth nearly every single day. I particularly thank my wife Julia, who made so much possible in the last years. She took care of the children during the cruises and conferences. She also handled most of the family life in the last months while I spent more time in front of my laptop than with Fenja, Alma and her. A special thanks goes to my parents and grandparents who have supported me since my childhood. A big thanks to my sister Christin and my friends Jule, Selina, Eefke and Kiki, who revised and improved the English of this thesis instead of doing their jobs. I am also grateful for the babysitter service of my parents-in-law and my friends Paul and (again) Mel, while I was working on this thesis.

And the last thing I would like to acknowledging mention is, of course, the Baltic Sea that was a fresh place after cycling throughout the whole time. It still surprised me with different turbidity, salinity, temperature and floor conditions every morning. I enjoyed the last years and I have to admit that I am a bit sad that the Baltic Sea will no longer be next to my door.

This work was funded by the Leibniz Association (WGL grant SAW-2012-IAP-4).

Contents

Chapter 1.

Introduction

1.1. Motivation

The maritime system of the Baltic Sea strongly depends on the vertical salinity gradient and the corresponding strong stratification, which limits the exchange between the brackish and therefore lighter surface waters, and the salty near-bottom water pool. The halocline separating these two water masses suppresses vertical turbulent mixing and limits the oxygen supply to the deeper layers. The deep-water volume is therefore almost exclusively ventilated by inflows of salty and oxygen rich water masses, which have their origin in the North Sea. These inflow events happen at irregular intervals (Mohrholz et al. 2015), and therefore do not guarantee a continuous supply of oxygen. Hence, anoxic zones occur regularly in the deep layers of the Baltic Sea and their spatial extent has grown in the last decades (Feistel et al. 2016). The amount of salt imported by such inflows is balanced by an outflow of brackish surface waters to the North Sea. Both processes are part of an overturning circulation that is closed by various diapycnal mixing processes which transport salt from the near-bottom salt water pool through the halocline towards the surface layer. Diapycnal mixing is also important for the transport of other dissolved tracers. Phosphorus as an example for an ecologically relevant tracer released from the sediments under anoxic conditions (Hille et al. 2005) is transported into the euphotic zone, where it may trigger cyanobacteria blooms. It has also been suggested that diapycnal mixing may generate a transition zone between oxygen-rich intruding waters and the anoxic and methane-enriched surroundings thus increasing the abundance of methane-oxidizing bacteria (Schmale et al. 2016).

All in all, a diapycnal salt transport of $30\,\mathrm{kg\,m^{-2}\,a^{-1}}$ (Reissmann et al. 2009) through the halocline is needed to close the overturning circulation. This salt transport corresponds to a turbulent diffusivity of approximately $2 \times 10^{-6}\,\mathrm{m^2\,s^{-1}}$ (Reissmann et al. 2009) in the halocline for the conditions in the Gotland Basin. The diffusivities needed to close the budget and to explain observed structures in salinity and temperature are even higher, in fact of order $10^{-5}\,\mathrm{m^2\,s^{-1}}$, in the deeper parts of the Gotland Basin (Holtermann et al. 2012), because of the smaller gradients. In contrast to the Gotland Basin, where basin-scale topographic waves dominate deep-water motions (Holtermann et al. 2012), near-inertial waves have been shown to be the most energetic class of motions in the Bornholm Basin (van der Lee and Umlauf 2011). Therefore, van der Lee and Umlauf (2011) also investigated the role of near-inertial wave mixing with the help of direct turbulence measurements in the center of the Bornholm Basin. They found bands of enhanced turbulence in the halocline correlated with near-inertial shear layers. The calculated diffusivities rarely exceed the threshold of $10^{-6}\,\mathrm{m^2\,s^{-1}}$. The processes responsible for boundary mixing as well as their relevance for the overall energetics and net vertical transport are still not sufficiently investigated at the moment although previous research clearly suggests that these processes are important. E.g., Holtermann et al. (2012) investigated the spreading of an artificial tracer below the halocline in the Gotland Basin, and found indirect evidence for the importance of boundary mixing. In their study, vertical diffusivities show a dramatic increase by the time the tracer comes in contact with the lateral boundaries of the basin.

Motivated by the results of van der Lee and Umlauf (2011) and Holtermann et al. (2012), the studies presented in this thesis are focused on boundary mixing processes, based on direct turbulence measurements at lateral slopes in the Bornholm Basin. The corresponding boundary data were collected parallel to the data from the basin center discussed in van der Lee and Umlauf (2011) during cruises in 2008 and 2010. The results presented in this thesis do not only provide some first insights into the boundary mixing processes in the Bornholm Basin of the Baltic Sea, they may also be relevant for other systems dominated by near-inertial motions, including lakes, inland seas, and some continental shelves, where diapycnal mixing at boundaries might be important as well.

1.2. Outline

Chapter 1 outlines basic properties of the Baltic Sea and of internal waves. Several mixing processes are discussed in the context of the Baltic Sea overturning circulation. Particular attention is payed to internal wave and boundary mixing, because these processes are essential for the understanding of the main part. The study area, the instrumentation and the methods to derive mixing parameters are discussed in chapter 2. Chapter 3 of this thesis concentrates on bottom boundary mixing at lateral slopes forced by near-inertial waves during summer conditions, focusing in particular on the efficiency of mixing in sloping bottom boundary layers. This investigation was published in *Journal of Geophysical Research: Oceans* under the title "Efficient boundary mixing due to near-inertial waves in a non-tidal basin: Observations from the Baltic Sea" (Lappe and Umlauf 2016). Chapter 4 is focused on boundary mixing processes during winter condition, emphasizing the role of a strong halocline intersecting with the lateral slopes of the basin. This work is part of a manuscript in preparation.

1.3. The Baltic Sea

The Baltic Sea is a non-tidal semi-enclosed sea in the northern part of Europe. It has an area of $4.2 \times 10^5\,\mathrm{km}^2$ and a volume of $22 \times 10^3\,\mathrm{km}^3$ (HELCOM 2002). The Baltic Sea can be subdivided into the following sub-areas (Fig. 1.1): Skagerrak (SR), where it is connected to the North Sea, Kattegat (KG), Belt Sea (Bt), Arkona Sea (AS), Bornholm Sea (BS), Western Gotland Sea (WGS), Eastern Gotland Sea (EGS), Gulf of Riga (GR), Gulf of Finland (GF), Bothnian Sea (BoS) and Bothnian Bay (BoB). Despite the connection to the North Sea, the Baltic Sea is brackish and differs strongly in its species composition from the North Sea. The positive freshwater input, precipitation ($237\,\mathrm{km}^2$) and river runoff ($428\,\mathrm{km}^2$) exceed evaporation ($184\,\mathrm{km}^2$) (Feistel et al. 2008), is responsible for the strongly reduced salinity compared to the ocean. Additionally, the exchange to the North Sea is limited by three narrow straights [Danish Straits (Little and Great Belt) and Sound] in combination with two shallow sills, the Darss Sill (depth of $18\,\mathrm{m}$) and the Drodgen Sill (depth of $8\,\mathrm{m}$) (Feistel et al. 2008).

The freshwater input is dominated by the river runoff which primarily (about 70%) enters in the Gulf of Riga, Gulf of Finland and Gulfs of Bothnia (Bergström and Carlsson 1994). The freshwater remains in the surface layer as its density is lower, where it

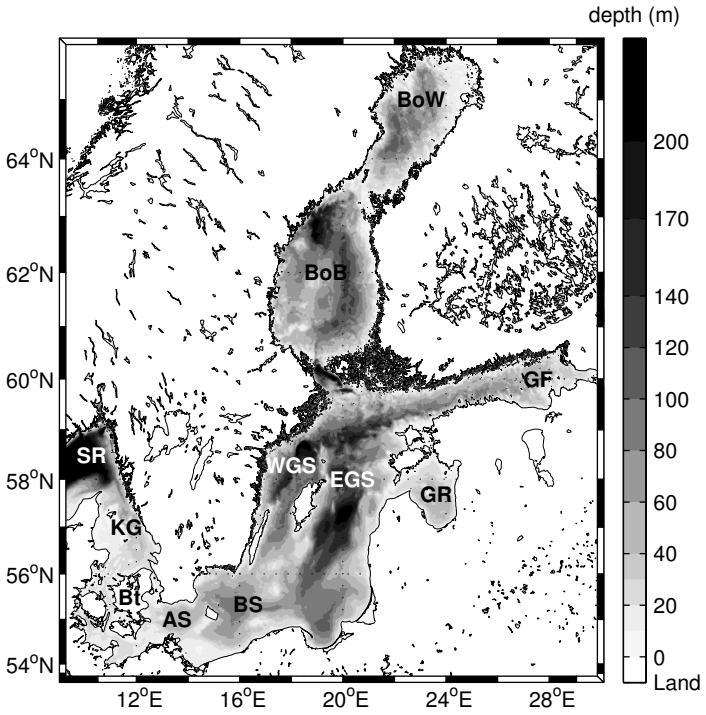

Figure 1.1.: Topography of the Baltic Sea. Shortcuts are explained in the beginning of section 1.3.

is partly mixed with the surrounding waters. Surface salinities vary between $25\,\mathrm{g\,kg^{-1}}$ in the Kattegat and $5\,\mathrm{g\,kg^{-1}}$ in the Gulf of Bothnia (Reissmann et al. 2009). A second effect of the freshwater surplus is the positive long-term sea level anomaly which leads to a barotropic pressure gradient and an outflow of brackish surface water into the North Sea. The inflow of saltier and therefore denser waters of the North Sea is hindered by the sills mentioned above. Nevertheless, there are conditions that force inflows of North Sea water into the Baltic Sea. It is usual to distinguish between barotropic and baroclinic types of inflows:

- Barotropic inflows are driven by barotropic pressure gradients, which are triggered by meteorological conditions. So-called Major Baltic Inflows are characterized by their large volumes ($100\,\mathrm{km^3}$ to $250\,\mathrm{km^3}$) and high salinities ($17\,\mathrm{g\,kg^{-1}}$ to $25\,\mathrm{g\,kg^{-1}}$) (Feistel et al. 2008). The conditions for a Major Baltic Inflow prevail if a longer period of easterly winds results in a sea level drop of some decimeters in the Baltic Proper in relation to the Kattegat sea level state (Reissmann et al. 2009), followed by westerly winds for 5 days or longer. Barotropic inflows occur mostly in winter and early spring (Matthäus and Franck 1992).

- Baroclinic inflows are characterized by baroclinic pressure gradients caused by horizontal salinity differences across the Danish straits. They appear under calm wind conditions which usually occur in late summer (Feistel et al. 2008). The inflow volume is much smaller than for Major Baltic inflows. The following example taken from Feistel et al. (2008) compares barotropic and baroclinic effects: The pressure difference at the bottom of two $28\,\mathrm{m}$ deep water columns with homogeneous salinities of $25\,\mathrm{g\,kg^{-1}}$ and $8\,\mathrm{g\,kg^{-1}}$ corresponds to a difference of $40\,\mathrm{cm}$ in sea level.

The inflowing water interleaves in the Baltic Sea corresponding to its density. If the water is dense enough, it forms a bottom gravity current and replenishes, step by step, the bottom waters of the Arkona Basin, the Bornholm Basin, and the Gotland Basin. The step-like character of the Baltic Sea topography from the Belt Sea to the Eastern Gotland Basin is shown in Figure 1.1. Only a Major Baltic Inflow renews the deep water to a significant degree (Schinke and Matthäus 1998), like it happened in beginning of 2015 (Mohrholz et al. 2015). The inflowing water changes its properties on its way from the Belt Sea to the Gotland Basin because it entrains surrounding waters (Lass and Mohrholz 2003), which leads to an increasing volume and a decreasing salinity. In addition to the salt transport into the basins the inflow also ventilates the near-bottom waters. These areas are separated from the ventilated surface waters by a persistent halocline that limits the exchange of dissolved tracers like salt, oxygen or nutrients. The halocline is located in $35\,\mathrm{m}$ to $40\,\mathrm{m}$ depth (Stigebrandt 1987) in the Arkona Basin in comparison to a depth of $50\,\mathrm{m}$ to $60\,\mathrm{m}$ in the Bornholm Basin or to a depth of $70\,\mathrm{m}$ to $90\,\mathrm{m}$ (Stigebrandt 1987) in the Eastern Gotland Basin. These differences in depth are a result of sills in the connecting channels. A seasonal thermocline develops in addition to the halocline during spring and summer. It separates the warm surface layer from the cold winter water in a depth of $10\,\mathrm{m}$ to $30\,\mathrm{m}$. Accordingly, the water column can be approximated by a 2-layer system in winter, where vertical mode-1 motions are dominant and a 3-layer system with dominant mode-2 motions in summer (van der Lee and Umlauf 2011). In summer the halocline becomes broader and less stratified because of diapycnal mixing processes and the isolation from surface-layer turbulence (entrainment) due to the sheltering effect of the seasonal thermocline. During winter the thermocline erodes and the halocline is sharpened by a combination of surface layer turbulence and winter convection (Reissmann et al. 2009).

The Baltic Sea exhibits an overturning circulation. The outflow of brackish surface water and the corresponding export of $4\,\mathrm{Gt}$ salt per year (Feistel and Feistel 2006)

is balanced by irregular inflow events on the long-term average. The circulation is closed by diapycnal mixing processes, which transport salt with a transport rate of $30\,\mathrm{kg\,m^{-2}\,a^{-1}}$ (Feistel et al. 2008) through the halocline. On the basis of this salt budget a diffusivity of $2 \times 10^{-6}\,\mathrm{m^2\,s^{-1}}$ (Reissmann et al. 2009) can be calculated in the halocline of the Gotland Basin. A short discussion of mixing processes follows in section 1.5. The overturning circulation has a time scale of decades that can be derived from the typical residence times (Feistel et al. 2006; Meier et al. 2006).

The overturning circulation strongly affects the ecosystem of the Baltic Sea. The crucial point is the occurrence of Major Baltic Inflows to ventilate the deep waters of the deep basins. A frequently cited example is the reproduction of cod. The reproduction is most efficient in regions where the salinity is larger than $11\,\mathrm{g\,kg^{-1}}$ and the oxygen concentration exceeds $2\,\mathrm{ml\,l^{-1}}$ (Plikshs et al. 1993). These conditions can only be fulfilled in the deep basins where oxygen is limited. The frequent occurrence of Major Baltic Inflows stopped in the beginning of the 1980s and was replaced by single events and longer stagnation periods (Mohrholz et al. 2015). As a result, zones of anoxic conditions grew in the last decades (Feistel et al. 2016). In addition to the absence of oxygen, toxic hydrogen sulphide occurs and reduces sediment bounded iron-3-hydroxophosphate complexes (Hille et al. 2005). As a consequence, phosphate and iron(II)ions accumulate in the deep layers. Diapycnal mixing processes transport phosphate into the surface layer and increase the phosphorus concentration in the euphotic zone. In summer, when nitrogen is depleted after the spring bloom in the surface layer, cyanobacteria take up the phosphate and fixate nitrogen from the atmosphere. Thus increased phosphate concentrations are a main condition for cyanobacteria blooms. These blooms are potentially toxic and therefore of socioeconomic interest (Wasmund et al. 2000). The dead organisms sink down after the bloom. The remineralisation process consumes oxygen and therefore accelerates the oxygen depletion and the spreading of anoxic zones, where as well phosphate is released from the sediments. It is a self-sustaining “vicious circle” (Vahtera et al. 2007). This feedback loop is stopped by a Major Baltic Inflow because phosphate is partly buried in the sediments (Balzer 1984) under oxic conditions.

1.4. Internal waves

Internal waves are omnipresent in the ocean and the Baltic Sea and are also known to provide a crucial contribution to diapycnal mixing at many locations. As these internal motions are central to this thesis, their properties are briefly revisited in the following. Their relation to mixing is discussed in section 1.5.1

1.4.1. Internal waves in an unbounded ocean

It is convenient to use the linearized momentum equations to describe internal waves in a stratified and rotating system (Kundu and Cohen 2008, p. 599):

$$\frac{\partial u}{\partial t} - fv = -\frac{1}{\varrho_0}\frac{\partial p'}{\partial x} \tag{1.1}$$

$$\frac{\partial v}{\partial t} + fu = -\frac{1}{\varrho_0}\frac{\partial p'}{\partial y} \tag{1.2}$$

$$\frac{\partial w}{\partial t} = -\frac{1}{\varrho_0}\frac{\partial p'}{\partial z} - \frac{\rho'}{\varrho_0}g \tag{1.3}$$

$$0 = \frac{\partial u}{\partial x} + \frac{\partial v}{\partial y} + \frac{\partial w}{\partial z} \tag{1.4}$$

$$0 = \frac{\partial \rho'}{\partial t} - \frac{\varrho_0 N^2 w}{g} \quad , \tag{1.5}$$

where the velocity vector (u, v, w), the corresponding position vector with the components x (eastward), y (northward) and z (upward), the time t, the Coriolis frequency f, the perturbation pressure p', the perturbation density ρ', a constant reference density ϱ_0, the buoyancy frequency N and the gravity acceleration g are introduced. The system of equations is composed of the momentum equations (1.1) – (1.3), the continuity equation (1.4) and the density equation (1.5). The perturbation density in (1.5) is the deviation from the background density $\bar{\rho}$, that fulfills the hydrostatic equation,

$$\frac{\partial p_b}{\partial z} = -\bar{\rho}g \quad , \tag{1.6}$$

where p_b is the hydrostatic pressure. The perturbation pressure denotes the deviation from the above introduced p_b. The background stratification is described by the

buoyancy frequency (Brunt-Väisälä frequency) squared

$$N^2 = -(g/\varrho_0)\partial\bar{\rho}/\partial z. \tag{1.7}$$

Combining equations (1.1)–(1.5), the wave equation

$$\frac{\partial^2}{\partial t^2}\nabla^2 w + \left(N^2\nabla_h^2 + f^2\frac{\partial^2}{\partial z^2}\right) w = 0 \tag{1.8}$$

can be derived. The Nabla operator is defined by $\nabla = (\partial/\partial x)\mathbf{e}_x + (\partial/\partial y)\mathbf{e}_y + (\partial/\partial z)\mathbf{e}_z$, where $\mathbf{e}$ is the unit vector and subscript h stand for horizontal. The equation (1.8) can be solved for an unbounded ocean by assuming a plain-wave ansatz for the vertical velocity $w = w_0 \exp[i(kx + ly + mz - \omega t])$. The waves that solve equation (1.8) are characterized by the dispersion relation

$$\omega^2 = \frac{N^2k_h^2 + f^2m^2}{k_h^2 + m^2} \quad . \tag{1.9}$$

Please note that the Brunt-Väisälä-Frequency N was required to be constant, because the exponential ansatz can only be used for constant coefficients. Here, k, l, m are the wave numbers in x, y and z directions. The horizontal wave number is defined as $k_h^2 = k^2 + l^2$. It can be shown, using the WKBJ (Wentzel, Kramers, Brillouin and Jeffreys) method (e.g. Olbers et al. 2012), that the dispersion relation remains the same for variable $N(z)$. This approach is valid as long as wave length and periods are short in comparison to spatial and temporal scales in the mean fields (e.g. Olbers et al. 2012). The dispersion relation can be reorganized to an equation for the vertical wave number

$$m = \sqrt{(k^2 + l^2)\frac{(N^2 - \omega^2)}{(\omega^2 - f^2)}} \quad , \tag{1.10}$$

which is real in the frequency range $f < \omega < N$. "Thus the ocean constitutes a bandpass waveguide for internal waves, and allows a propagation only between the two characteristic frequencies N and f" (Apel 1995). It should be noted that these limitations in frequency are given by the equations used in the beginning. If the non-traditional assumption is used, see Gerkema et al. (2008), the internal wave range extends.

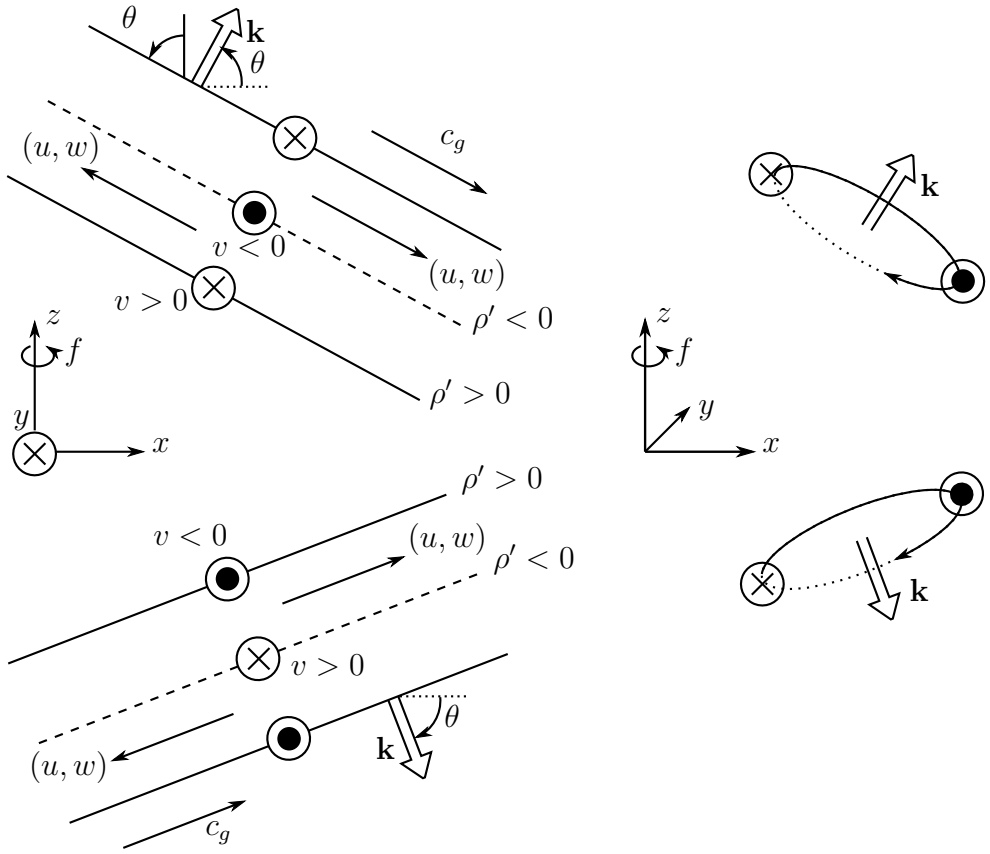

Figure 1.2.: redrawn from Sutherland (2010): The left hand side shows the relationship between the velocities, density and the interface elevation for an internal wave with upward (top) and downward (bottom) phase vector k. The right hand side illustrates the anticyclonic orbits of a fluid parcel that is advected by the internal waves beside it.

Based on the dispersion relation (1.9) the group velocity $\mathbf{c_g}$ and phase velocity $\mathbf{c_p}$ of internal waves can be calculated:

$$\begin{aligned}
\mathbf{c_g} &= \partial_k \omega \mathbf{e_k} + \partial_l \omega \mathbf{e_l} + \partial_m \omega \mathbf{e_m} \quad \text{with } \partial_k = \frac{\partial}{\partial k} \\
&= \frac{k}{\omega}\left[\frac{N^2}{k^2} - \frac{\omega^2}{k^2}\right]\mathbf{e_k} + \frac{l}{\omega}\left[\frac{N^2}{k^2} - \frac{\omega^2}{k^2}\right]\mathbf{e_l} + \frac{m}{\omega}\left[\frac{f^2}{k^2} - \frac{\omega^2}{k^2}\right]\mathbf{e_m} \qquad (1.11) \\
\mathbf{c_p} &= \frac{\omega}{|\mathbf{k}|^2}\mathbf{k} \\
&= \sqrt{\frac{N^2 k_h^2 + f^2 m^2}{k^6}}\mathbf{k} \quad . \qquad (1.12)
\end{aligned}$$

Both velocities are perpendicular to each other, thus the scalar product vanishes. Furthermore, the vertical component of the group velocity is derived by Olbers et al.

(2012) as:

$$\mathbf{c_{g3}} = -\left(\frac{N^2 - f^2}{\omega}\frac{k_h^2}{(k_h^2 + m^2)^2}\right) m\mathbf{e_m} \quad . \tag{1.13}$$

The phase velocity in equation (1.12) points to the same direction as the wavenumber. The direction of the vertical component of the group velocity points to the opposite direction of the vertical wavenumber due to the negative sign in the equation (1.13). This results in a characteristic property: A downward traveling internal wave has upward moving crests and troughs and vice versa. In Figure 1.2, which is redrawn from Sutherland (2010), the propagation of an internal wave is explained in more detail, assuming no variation in y direction. The individual quantities like u, v, w, ρ' vary sinusoidally as a result of the plane wave estimate. The density variation is given by the idealized crests (black lines show $\rho' > 0$) and troughs (black dashed line indicate $\rho' < 0$) for an internal wave characterized by an upward wave vector $\mathbf{k}$ and therefore a downward group velocity c_g (Fig. 1.2: top, left) . The crests and troughs are moving upward as $\mathbf{k}$ indicates. The velocity v varies like the density, as indicated. The velocities u and v are zero at the crest and trough. Furthermore, they vary as the vector arrows (u, w) are directed perpendicular to k in between. In this velocity field a fluid parcel rotates anticyclonically as shown on the right hand side. The explanation of the plain wave with downward wave vector is analogous.

1.4.2. Internal waves in a bounded ocean

The already discussed solution of the equation (1.8) does not include the effect of boundaries, which will be considered in the following. In the first step, lateral boundaries will be ignored, assuming that horizontal distances are much larger than vertical ones. Furthermore, the ocean is assumed to have a constant depth H. The plain-wave ansatz used before is slightly modified to $w = \hat{w}(z)\exp\left[i(kx + ly - \omega t)\right]$, which can be interpreted as the product of a vertical mode $\hat{w}(z)$ and a horizontal plain wave. From the ansatz and (1.8) it follows

$$\frac{\partial^2 \hat{w}}{\partial z^2} + \underbrace{(k^2 + l^2)\frac{(N(z)^2 - \omega^2)}{(\omega^2 - f^2)}}_{=m^2}\hat{w} = 0 \quad , \tag{1.14}$$

where the term in front of $\hat{w}$ defines the vertical wavenumber m squared, which also satisfies the dispersion relation (1.9). Equation (1.14) is a wave equation for the vertical mode $\hat{w}$. The boundary conditions are set to $w(-H) = 0$ at the bottom and $w(0) = 0$ for the surface. The surface condition is valid for the rigid lid case, where surface elevations are not allowed. This assumption induces an error of approximately $0.2\,\%$ (Olbers et al. 2012) in comparison to the free surface. Furthermore, a constant buoyancy frequency N is assumed. As a consequence, the vertical wave number is restricted to $n\pi/H$ where $n = 1, 2, \ldots$ is a non-negative integer, which stands for a standing mode. The dispersion relation becomes

$$\omega_n^2 = f^2 \left(\frac{1 + k_h^2 R_n^2}{1 + \dfrac{k_h^2 H^2}{n^2 \pi^2}} \right), \text{ with } R_n = \frac{NH}{fn\pi} = \frac{c_n}{f} \quad . \tag{1.15}$$

The internal Rossby radius R_n and the propagation speed $c_n = NH/(n\pi)$ of the vertical mode were introduced in equation (1.15). Typically, the Brunt-Väisälä-Frequency is much larger than the Coriolis frequency ($N \gg f$) which leads to $R_n = \dfrac{NH}{fn\pi} \gg \dfrac{H}{n\pi} = \dfrac{1}{m}$. Thus, the Rossby radius is much larger than the inverse of the vertical wavenumber (wavelength). Based on these considerations, internal waves can be divided (e.g. Kundu and Cohen 2008) into three ranges:

- **long wave range**: $k_h \lesssim \dfrac{1}{R_n} \Rightarrow k_h \ll \dfrac{n\pi}{H}$ (Waves are longer than the Rossby radius and the horizontal wavenumber is much smaller than the vertical), the dispersion relation (1.9) results in

$$\omega_n^2 \approx f^2 + f^2 R_n^2 k_h^2 = f^2 + c_n^2 k_h^2 \quad . \tag{1.16}$$

  In this case the waves are dispersive. This dispersion relation is the well known solution of internal Poincaré waves by Kundu and Cohen (2008) or inertial waves by Fennel and Lass (1989). The higher modes are characterized by frequencies close to the inertial frequency. As a consequence they are referred to as near-inertial waves.

- **intermediate range**: $\frac{1}{R_n} \ll k_h \ll \frac{n\pi}{H}$ (Waves are shorter than the Rossby radius and the horizontal wavenumber is much smaller than the vertical)

$$\omega_n^2 \approx \frac{N^2 k_h^2}{\frac{n^2\pi^2}{H^2}} \quad . \tag{1.17}$$

  These waves are non-dispersive.

- **short waves**: $k_h \gtrsim \frac{n\pi}{H}$ and $k_h \gg \frac{1}{R_n}$ (Waves are shorter than the Rossby Radius and the horizontal wavenumber is bigger than the vertical wavenumber, but they are in the same order (non-hydrostatic))

$$\omega_n^2 \approx \frac{N^2 k_h^2}{k_n^2 + \frac{n^2\pi^2}{H^2}} \quad . \tag{1.18}$$

  The waves are dispersive and rotation effects are negligible.

1.4.3. Internal waves in a bounded ocean forced by wind

Besides considering lateral boundaries, the ocean response to wind is also outlined in this section. The interaction of both is of particular importance for the description of near-inertial wave motions in the Baltic Sea, where wind is the main energy source and distances to lateral boundaries are small. Hence, the linearized momentum equations (1.1) – (1.5) must be extended by source terms that transfer the wind momentum into the water. This can be done by the introduction of volume forces (Fennel and Lass 1989), or vertical friction (Kundu et al. 1983). Both approaches result in the same Ekman transports in the surface layer. However, in the first case a mixing depth and in the second case a vertical diffusivity has to be estimated.

According to Fennel and Lass (1989) the equations (1.1) and (1.2) have to be extended by the source terms X and Y on the right hand side that obey

$$\int_{-H_{\mathrm{mix}}}^{\eta} \varrho_0(X, Y)\, \mathrm{d}z = (\tau^{(x)}, \tau^{(y)}) \quad , \tag{1.19}$$

where $\tau^{(x)}$ and $\tau^{(y)}$ are the wind stress components in the x and y directions, η is the surface elevation, and H_{mix} is the mixing depth of the wind. To separate the z-

dependence of the whole system of equations vertical modes $F_n(z)$ were introduced, that form a complete set and satisfy the orthonormality condition:

$$\frac{1}{H}\int_{-H}^{0} F_n F_m \,\mathrm{d}z = \delta_{nm} \;, \quad \text{where } \delta_{nm} = \begin{cases} 1 & \text{for } n = m \\ 0 & \text{otherwise} \end{cases} \quad . \tag{1.20}$$

The quantities u, v, p, X and Y can be expanded in the new basis according the rule:

$$\Phi(x,y,z,t) = \sum_{n=0}^{\infty} \Phi_n(x,y,t) F_n(z) \quad . \tag{1.21}$$

Based on these steps and the hydrostatic approximation, the set of equations result in (Fennel and Lass 1989)

$$u_{tn} - f v_n + \frac{p'_{xn}}{\varrho_0} = X_n \quad , \tag{1.22}$$

$$v_{tn} + f u_n + \frac{p'_{yn}}{\varrho_0} = Y_n \quad , \tag{1.23}$$

$$\frac{u_{xn} + v_{yn}}{p'_{nt}} \varrho_0 = -\lambda_n^2 \quad , \tag{1.24}$$

$$-\lambda_n^2 F_n(z) = \frac{\partial}{\partial z}\frac{1}{N^2(z)}\frac{\partial}{\partial z} F_n(z) \quad . \tag{1.25}$$

A condensed notation is used in equations (1.22) – (1.24), where the subscripts denote the derivations with respect to x, y and t. Equation (1.25) is a Sturm-Liouville eigenvalue equation with the eigenvalues λ_n and the corresponding eigenfunctions $F_n(z)$. It can be solved independently and can also be rewritten in a more common form by introducing $Z_n(z) = N^{-2}(z)\ (\partial/\partial z) F_n(z)$:

$$\frac{\partial^2 Z_n(z)}{\partial z^2} + \lambda_n^2 N^2(z) Z_n(z) = 0 \quad . \tag{1.26}$$

Equation (1.14) has the same form if, consistent with the hydrostatic approximation, ω^2 is much smaller than N^2. The eigenvalues and eigenfunctions can be derived analytically for constant stratification by using the boundary conditions $(\partial/\partial z) F_n(-H) = 0$

and $(\partial/\partial z)F(0) + (N^2/g)F(0) = 0$ (Fennel and Lass 1989):

$$\lambda_0^2 = \frac{1}{gH} \tag{1.27}$$

$$\lambda_n = \frac{n\pi}{NH} \quad \text{for } n \geq 1 \tag{1.28}$$

$$F_0(z) = 1 - \frac{N^2 H}{g}\left(\frac{z}{H} + \frac{1}{2}\left(\frac{z}{H}\right)^2\right) \tag{1.29}$$

$$F_n(z) = (-1)^n\sqrt{2}\cos\left(n\pi\frac{z}{H}\right) \quad \text{for } n \geq 1 \quad . \tag{1.30}$$

The modes speeds c_n are the inverse of the eigenvalues λ_n. The barotropic mode F_0 travels with the highest, the shallow water velocity $\sqrt{gH}$. The following baroclinic modes travel with decreasing velocities with increasing mode numbers. The mode number coincides with the zero crossings of the vertical mode profile, which can nicely be seen in the argument of the cosine in equation (1.30). For realistic stratification the eigenvalue equation (1.25) has to be solved numerically and the vertical mode profiles are not sinusoidal anymore, but the number of zero crossings further coincides with the mode number. In the Baltic Sea, the general stratification is characterized by the permanent halocline and a seasonal thermocline. Consequently, the winter is dominated by vertical mode-1 motions and the summer by mode-2 motions, see van der Lee and Umlauf (2011). Combining equations (1.22)–(1.24) a differential equation for v can be derived:

$$v_{tttn} + f^2 v_{nt} - \frac{1}{\lambda_n^2}\left(v_{nxxt} + v_{nyyt}\right) = \frac{1}{\lambda_n^2}\left(X_{nxy} - Y_{nxx}\right) + Y_{ntt} - fX_{nt} \quad . \tag{1.31}$$

This differential equation can be solved analytically for different boundary conditions and for different kinds of wind forcing. The wave-like solutions obey the dispersion relation (1.16). The conclusions from the analytical theory (Fennel and Lass 1989) that are relevant for this work will be summarized in the following. Let us consider an infinitely long coast at $y = 0\,\mathrm{m}$ and homogeneous wind that blows in the negative x-direction and starts at $t = 0\,\mathrm{s}$. The onset of the wind immediately leads to inertial oscillations and an offshore Ekman transport in the surface layer of the ocean. Internal wave modes are generated at the coast and start to propagate offshore. The barotropic mode is the fastest and reaches an arbitrary chosen reference position first. It reduces the surface inertial oscillation and establishes a $180°$ phase-shifted oscillation in the layer below the surface layer. Subsequently, internal-wave modes arrive and minimize the oscillations above and below the mixing depth and lead to a blue

shift in the frequency. The precise contribution of the mode at a specific position and time is determined by the weighting factor $\Phi_n(x, y, t)$, see eq. (1.21). It should also be mentioned that the higher modes establish the shear in areas where pycnoclines exist as it was shown by van der Lee and Umlauf (2011) for the center of the Bornholm Basin.

Back to the analytical model: after all modes arrived, the non-oscillatory solution emerge. This is a typical Rossby adjustment problem, where the information of a inhomogeneity e.g. a coast, or variations in the wind field are propagated by waves to a reference position. The non-oscillatory solution (Fennel and Lass 1989) includes, besides water that is advected offshore by Ekman transport in the surface layer, an Ekman compensation flow in the layer below. Upwelling occurs near the coast, within the first baroclinic Rossby radius R_1. Furthermore, an along shore current in wind direction, called coastal jet, is found in the surface layer within R_1. Both processes are shown schematically in the upper right corner of Figure 1.3.

Additional effect may become important if the setting becomes more complicated. For an infinitely long channel, which is a good first-order model for some positions in the Baltic Sea, the onset of homogeneous along-shore winds generates internal-waves modes at both coasts. A superposition of modes from both sides explains the velocities at an arbitrary position in the channel. Moreover, the modes will be reflected at the channel walls and pass the reference position again (Fennel 1989). Inhomogeneities in the wind or at the coast lead to the generation of Kelvin waves, which damp or even change the upwelling to a downwelling signal in the upwelling favorable region and propagate this upwelling signal to other regions (Fennel et al. 2010).

1.5. Mixing processes

It was mentioned in section 1.3 that diapycnal mixing processes are important to understand the overturning circulation of the Baltic Sea. These processes will be summarized and discussed more in detail in the following. Figure 1.3, redrawn from Reissmann et al. (2009), provides a conceptual view of the overturning circulation and highlights the most important mixing processes. Internal wave and boundary mixing are in the focus of this thesis and will be discussed first, followed by a short introduction to the other processes. The role of bio-mixing (i.e., mixing by moving organisms), as discussed by Dewar (2009), is ignored.

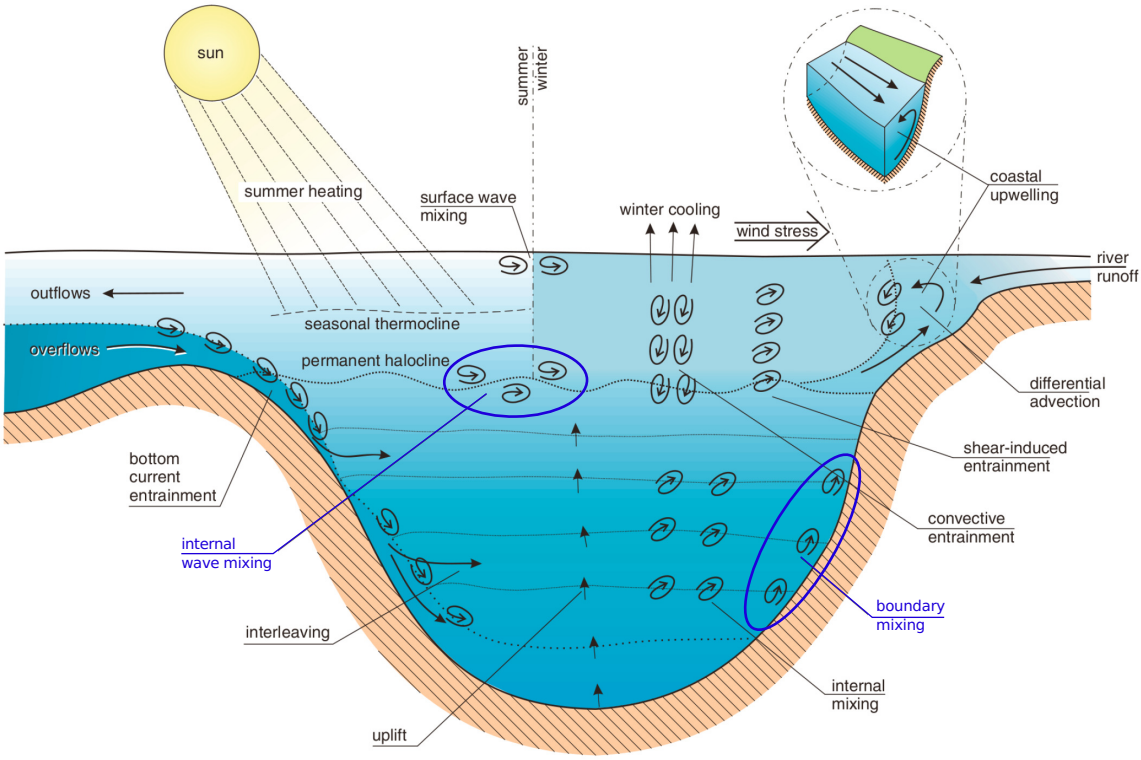

Figure 1.3.: Sketch modified after Reissmann et al. (2009). The schematic overview shows the Baltic Sea overturning circulation. Sporadic inflow events of saline North sea water import salt into the deep layers. The salt is transported to the surface by diapycnal mixing processes including internal wave mixing and boundary mixing at lateral slopes. The surface water is brackish caused by a positive freshwater balance and is exported to the North Sea.

1.5.1. Internal wave mixing

Internal waves were produced locally by the tides (Kelly et al. 2012), changing winds (Kundu et al. 1983), decaying mesoscale eddies (Clément et al. 2016), and transport their energy to a different location, where it may be released and made available for mixing.

Internal wave breaking in shear flows

Up to now, only internal waves without background flow (section 1.4) have been considered. Similar to the small perturbation equations (1.1)–(1.5), a system of equations can be derived that includes a background flow with purely vertical shear and ignores earth rotation, see e.g. Olbers et al. (2012). It can be shown that the resulting equa-

tions can be combined into the Taylor-Goldstein equation (Olbers et al. 2012)

$$\partial_z \partial_z \hat{w} + \left[\frac{N^2}{(U-c)^2} - \frac{\partial_z \partial_z U}{U-c} - k_h^2 \right] \hat{w} = 0 \quad , \tag{1.32}$$

where the phase velocity $c = \omega / k_h$ and the background velocity $U = (\mathbf{U}(z) \cdot \mathbf{k}_h)/k_h$ appear. The derivation further includes the ansatz $X = \hat{X}(z) \exp[i(\mathbf{k}_h \cdot \mathbf{x} - \omega t)]$ for the quantities $X = \{\mathrm{u}, w, p, \rho'\}$. Equation (1.32) is equal to (1.8) if the background flow and the inertial frequency f are set to zero. The Taylor-Goldstein equation and the boundary conditions ($\hat{w}(0) = 0$ and $\hat{w}(-H) = 0$) define a vertical eigenvalue problem. In comparison to the Sturm-Liouville eigenvalue equation (1.25) the solutions for ω, $\hat{w}$ and c do not have to be real. A non-dimensional parameter can be derived, called local Richardson number

$$\mathrm{Ri} = \frac{N^2}{(\partial_z U)^2} \tag{1.33}$$

that becomes smaller than 0.25 if the phase velocity in equation (1.32) is imaginary. This is a necessary criterion for shear instability. The occurrence of imaginary phase speed c_i is interesting because the exponential term of the ansatz can also be written as $\exp[k_h c_i t + i k_h (\hat{x} - c_r t)]$, where c_r is the real part of the phase velocity, $\hat{x}$ the rotated coordinate in direction of k_h, and $k_h c_i$ appears as a growth rate. In the case of $c_i k_h = 0$ the growth rate vanishes. The system is neutrally stable because the exponential term is purely oscillatory. For $c_i k_h < 0$ small perturbations are damped out in time and in the critical case $c_i k_h > 0$ small perturbations grow in time. The initially linear instabilities grow, become non-linear and ultimately result in turbulence. This internal wave breaking and the corresponding mixing is probably the most important mixing process in the oceans (Waterhouse et al. 2014).

Based on the same equations, Carpenter et al. (2011) provide a physical interpretation of instabilities in shear flows. Internal gravity and vorticity waves exist in a stratified system with shear. Three kinds of instabilities occur: Kelvin-Helmholtz instabilities (interaction of two vorticity waves), Holmboe instability (interaction of an internal wave and a vorticity wave) and Taylor-Caulfield instability (interaction of two internal waves). The Kelvin-Helmholtz instability results in overturning billows at the density and shear interface. The Holmboe instability shows propagating cusp-like waves that occur if the shear interface is thicker than the density interface.

Regardless of the exact mixing process, mixing leads to an increase of the background potential energy, or, in other words, it shifts the center of mass of the water column upwards. The actual mixing process is done directly at the interface between the different fluids on viscous scales. The overall mixing of fluids can be accelerated by turbulence, that does not influence the molecular mixing, but increases the surface between the fluids and, consequently, increases the places where molecular mixing works by orders of magnitude. The characterization of turbulence is done by the turbulent kinetic energy (TKE) equation (e.g. Kundu and Cohen 2008)

$$\begin{aligned}\frac{\mathrm{D}}{\mathrm{D}t}\frac{1}{2}\langle u_j' u_j'\rangle + \underbrace{\frac{\partial}{\partial x_i}\left(\frac{1}{\varrho_0}\langle u_i' p'\rangle + \frac{1}{2}\langle u_i' u_j' u_j'\rangle - \nu\langle u_j'\sigma_{ij}\rangle\right)}_{\mathrm{T}} = \\ = \underbrace{-\langle u_j' u_i'\rangle\frac{\partial}{\partial x_i}U_j}_{\mathrm{P}} + \underbrace{\langle b' w'\rangle}_{\mathrm{G}} \underbrace{-\frac{1}{2}\nu\sigma_{ij}\sigma_{ij}}_{\varepsilon} \quad ,\end{aligned} \tag{1.34}$$

here, in indical notation ($u_1' = u'$, $u_2' = v'$, $u_3' = w'$). Equation (1.34) introduces the turbulent part of the velocity u_j', the shear tensor of velocity fluctuations $\sigma_{ij} = (\partial u_i'/\partial x_j + \partial u_j'/\partial x_i)/2$, the perturbation of the buoyancy $b = -g\rho'/\varrho_0$ and the Reynolds average $\langle\cdot\rangle$. The TKE can be changed by transport terms T, where the pressure transport, the transport by turbulent motions and the viscous transport are listed in order of appearance. The shear production term P is the actual source term of TKE, it extracts energy from the mean flow. In contrast, the turbulent buoyancy flux G describes the conversion of TKE into potential energy. It is the physical mixing quantity, provided that the flux describes a irreversible conversion in background potential energy. This assumption is not always true as explained by the following example: A turbulent eddy advects a water parcel vertically in a stratified environment. This process is explained by the buoyancy flux. First, this process is a reversible process that increases the available potential energy. As a second step, the water parcel can be mixed with the sounding, which means a transformation from available in background potential energy, or, as a further opportunity, the water parcel is restratified. In general, the first opportunity of step two is assumed, ignoring a possible restratification. However, the buoyancy flux is the main quantity in the discussion of mixing. Although the buoyancy flux is usually not measured directly. In this work the buoyancy flux is determined via a parametrization that depends on the dissipation rate ε of TKE and is explained more in detail in section 2.5.2. The dissipation rate ε describes the conversion of TKE into

internal energy. This quantity can be estimated from shear microstructure measurements (see also section A.1.2.)

Near-inertial wave mixing in the Baltic Sea

Van der Lee and Umlauf (2011) investigate the role of near-inertial wave mixing for summer and winter stratification by direct turbulence measurements in the center of the Bornholm Basin. They calculated modes according to the Sturm-Liouville eigenvalue problem (1.25) and decompose the velocity field in corresponding contributions. As a result, the lowest modes carry most of the energy, but the vertical shear is established by higher modes. This internal wave shear occurs in band-like structures in the halocline and coincides with layers of enhanced dissipation rates. This process is listed in Figure 1.3 as internal wave mixing. A dissipation rate parametrization, developed by MacKinnon and Gregg (2005) for shelf seas, was adjusted to the data set. Calculated diffusivities rarely exceed the threshold of $1 \times 10^{-6}\,\mathrm{m\,s^{-2}}$ in the halocline.

1.5.2. Boundary mixing

Boundary mixing (Fig. 1.3) summarizes various classes of mixing processes at the boundary, including the collapse of a mesoscale eddy (section 1.5.3) or the critical breaking of internal waves at a slope. Internal waves break at a lateral boundary, if the slope angle β satisfies the condition for critical reflection (e.g., Munk 1981)

$$\tan\beta = \left[\frac{\omega^2 - f^2}{N^2(z) - \omega^2}\right]^{\frac{1}{2}} \quad . \tag{1.35}$$

This contribution to mixing is of particular importance at slopes that are critical for an internal tide that carries energy at a single frequency (Moum et al. 2002). In the virtual absence of tides, like in the Baltic Sea, the contribution to mixing of this effect is unknown. Moreover, internal waves may also interact with slopes in additional ways, as discussed in this section.

Specifically, boundary mixing is a consequence of the boundary conditions. Bottom friction forces the velocity to decrease towards the boundary to fulfill the no-slip condition at the boundary. The resulting shear leads to turbulence. Based on the *law of the wall* the following parametrization for the log layer can be made in unstratified

environments:

$$u = \frac{u_*}{\kappa} \ln(\frac{z}{z_0}), \qquad \varepsilon = \frac{u_*^3}{\kappa z} \quad , \tag{1.36}$$

where the velocity u outside the boundary layer, the friction velocity u_*, the von Kármán constant κ, the distance z to the boundary, the roughness parameter z_0 and the dissipation rate ε are introduced. This parametrization loses its validity in the presence of stratification, which has to be expected near sloping topography as indicated in Figure 1.3. However, an unstratified layer develops close to the bottom also in stratified environments, where the *law of the wall* is still valid.

Before dealing with processes that lead to mixing at a lateral slope, some general properties are listed. Isopycnals rise in the boundary layer of a slope as a result of increased mixing (Phillips et al. 1986) before they intersect perpendicularly with the bottom to fulfill the zero-flux condition. Similarly, a pycnocline, e.g. thermocline or halocline in the Baltic Sea, is spread in the boundary layer as a consequence of increased diffusivities (Phillips et al. 1986). The spreading is strongest in the center of the pycnocline. Buoyancy forces induced by a deviation from stably stratified conditions result in an upward cross slope flow in the boundary layer below the pycnocline and a downward flow above (Fig.1.4), respectively. Both flows converge in the center of the pycnocline. A measured evidence is given by Kunze et al. (2012) based on turbidity measurements.

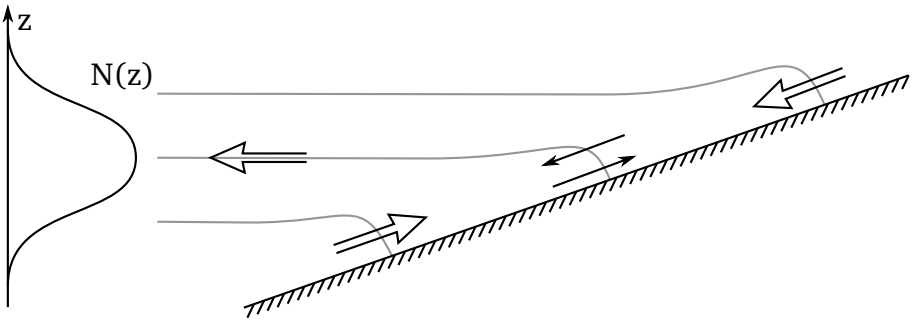

Figure 1.4.: Sketch modified from Garrett (1991). Isopycnals (gray) indicate the spreading of a pycnocline at a sloping boundary. The spreading is largest in the center of the pycnocline. Thin arrows denote the secondary circulation, that tries to flatten the isopycnals. The tertiary circulation is indicated by the broad arrows and tries to restore the stratification.

This situation becomes more complicated if oscillatory currents are considered, like internal tides, internal seiches or other types of internal waves that force an alternating

up- and down-slope movement of isopycnals. During the upslope phase denser water is pushed above lighter water (Lorke et al. 2005), because of the near-bottom shear. This process causes convective turbulence, but its impact on mixing is not straightforward to quantify, as mixing efficiency is generally unknown in boundary mixing processes. In general, an Osborn-like relation (eq. 2.3) is used to describe the dependence of the buoyancy flux on the dissipation rate of turbulent kinetic energy, where the flux coefficient γ (constant of proportionality) is a function of dissipation and stratification as explained more in detail in section 2.5.2. During the downslope phase, bottom shear leads to a shear-induced compression of isopycnals. As a consequence, stratification increases and turbulence is suppressed, but γ is not necessarily reduced as in the first case (Becherer and Umlauf 2011). Besides this mechanism, convection is possible in the down-slope phase. The down-slope Ekman velocity, which is induced by an along slope current in the Ekman layer, increases towards the bottom until the bottom friction stops and inverse the growth. This process moves lighter water beneath denser water, hence leading to convection (Moum et al. 2004). Holtermann and Umlauf (2012) referred to the latter process in the boundary layer of the Gotland Basin. Finally, upward and downward moving isopycnals alternate in an oscillation forcing and provide processes that lead to turbulence and, probably, mixing. The relevance of boundary mixing is still unclear, based on the unresolved issues of the flux coefficient close to the boundary.

Evidence for the relevance of boundary mixing in the Baltic Sea is given by Holtermann et al. (2012), who analyzed data from the Baltic Sea Tracer Release Experiment (BaTRE), where a passive tracer was released below the halocline and outside the bottom boundary layer in the center of the Eastern Gotland Sea (Fig. 1.1). This region is characterized by weak turbulence, because it is protected from surface layer turbulence and winter convection by the halocline. Diapycnal diffusivities, calculated on the basis of tracer spreading rates, were in the order of $1 \times 10^{-6}\,\mathrm{m^2\,s^{-1}}$ in the beginning of the experiment and increased by one order of magnitude after some months. This increase was interpreted as the result of the transition from interior to boundary mixing (Holtermann et al. 2012).

Two length scales are important to describe turbulence near a boundary. Both are based on considerations about eddy sizes. It is obvious that the size of an eddy is limited by the distance ζ to the boundary. The corresponding length scale is:

$$l = \kappa\zeta \quad , \tag{1.37}$$

where κ is the von Kármán constant. This limitation applies in the classical non-stratified, turbulent bottom boundary layer described by equation (1.36). In the presence of stratification the Ozmidov length scale

$$L_O = \sqrt{\frac{\varepsilon}{N^3}} \quad , \tag{1.38}$$

which describes the limitation of turbulent overturns in a stratified environment, forms a second potentially relevant length scale. The comparison of both length scales allows to decide which process limits the turbulent length scales. As a result the flux coefficient parametrization SKIF, listed in Table 2.3, which is valid in stratified environments, can also be used in the stratification dominated turbulence close to the boundary. It cannot be considered that the parametrizations for the flux coefficients as well as for the buoyancy fluxes (2.3) are valid where l limits the turbulence.

1.5.3. Further processes

Mixing in the surface layer

The upper boundary layer of the ocean is characterized by the exchange of heat, momentum and matter with the atmosphere. The seasonal variation in heat fluxes has a crucial influence on the properties of the surface layer. During summer, the upper layer is heated, the water density decreases, and a thermocline develops due to the effect of near-surface mixing processes (Fig. 1.3). During the cooling period in winter, the surface layer loses heat to the atmosphere, leading to convection. This is an efficient process to homogenize the surface layer and erode the thermocline. Alternating periods of heating and cooling with associated impacts on the surface layer also occur during the diurnal cycle (Smyth et al. 1996). Additionally, breaking surface waves, Langmuir circulation, shear induced turbulence and breaking internal waves (Thorpe 2005) may contribute to mixing in the surface layer. The momentum and mass transfers between the atmosphere and the ocean are associated with the effect of surface waves. E.g. the growth of surface waves depends on wind speed and forcing period, which are usually translated to a fetch (distance to the coast) (Holthuijsen 2007). Breaking surface waves generate turbulence and mixing. They also transfer momentum to the mean flow and generate bubbles (Thorpe 2005) that are important for the exchange of gases between atmosphere and ocean. The input of momentum leads to

vertical shear concentrated at the mixed layer base (Moum and Smyth 2001), where shear instabilities result in mixing (Fig. 1.3). Further, counter-rotating vortices aligned with the wind direction, often called Langmuir circulations, may occur in the mixed layer if waves are large enough, and distribute fluid and turbulence vertically (Moum and Smyth 2001). These motions are also responsible for the accumulation of bubbles or algae in surface streaks parallel to the wind direction as a result of near-surface convergence. Langmuir circulation is related to the Stokes drift and shear (Moum and Smyth 2001). The interaction of these processes have a tendency to homogenize the surface layer.

Mixing by mesoscale eddies

Mesoscale eddies are horizontally rotating gyres in quasi-geostrophic balance. Their dimension is determined by the first baroclinic Rossby radius $R_1 = c_1/f$ ($\approx 5\,\mathrm{km}$ in the Bornholm Basin), where c_1 is the speed of the first baroclinic mode (solution of the Sturm-Liouville eigenvalue problem (e.g. Olbers et al. 2012)) and f the inertial frequency. Mesoscale eddies in the Baltic Sea have a rotational speed of $20\,\mathrm{cm\,s^{-1}}$ to $30\,\mathrm{cm\,s^{-1}}$. They can drift with a velocity of several centimeters per second (Reissmann et al. 2009) and take trapped water with them. Eddies can be divided into two groups: anticyclonic eddies with vertically stretched isopycnals in their interior, as seen by Lass and Mohrholz (2003), and cyclonic eddies with compressed isopycnals (Lass et al. 2003). Mesoscale eddies may contribute in various ways to diapycnal mixing in the Baltic Sea. E.g. modified stratification and velocities inside eddies may force internal waves to scatter or break (Sheen et al. 2015). Due to the limited spatial extend of the major basins, Baltic Sea mesoscale eddies also frequently interact with the boundaries during their lifetime of approximately 4 months (Reissmann et al. 2009). The decay process or collapse releases the stored potential (isopycnal displacements) and kinetic energy. As a consequence, energy is available for turbulence and thus diapycnal mixing as well as for internal-wave radiation (Clément et al. 2016). The latter implies an indirect contribution to mixing as internal waves will break somewhere, and release their energy to turbulence. Reissmann et al. (2009) estimated a number of 15 coexisting eddies in the Bornholm Basin, suggesting that they are frequently occurring features in the Baltic Sea.

Mixing associated with dense bottom currents

Dense bottom currents, as displayed in Figure 1.3, are a crucial part of the overturning circulation, because the import of salt and oxygen into the deep layers is done by these currents. A Major Baltic Inflow, that is strongly connected with the ventilation of the deep layers in the Baltic Sea, passes several basins, sills and straights until it enters the Eastern Gotland Basin. This process causes an uplift of the ambient waters as shown in Figure 1.3. If the inflow interleaves in the deep part of a basin, the displacement will force an overflow of elevated water over an existing sill and therefore generates a bottom current that enters a following channel or basin, where a similar chain reaction will start. The elevation of water or isopycnals and the following overflow over a sill can also be done by waves, currents or even vertical mixing.

Furthermore, the properties of a bottom current are continuously changed by mixing. At the front of the inflow, denser inflow water is advected above lighter ambient water (Lass and Mohrholz 2003; van Aken 1986) as a result of the bottom shear (velocity decreases towards the bottom to fulfill the no-slip boundary condition). This process is called differential advection, where turbulence and mixing are a result of convection. Further, lighter ambient water (Fig. 1.3) is entrained into the bottom plume (Stigebrandt 1987; Arneborg et al. 2007), caused by the interfacial shear between bottom current water and the waters above. This process leads to decreasing salinity and density of the bottom current but also increases its water volume. Moreover, surface mixing can interact with the interface in shallower parts (Lass and Mohrholz 2003). A detailed understanding of these mixing processes is of particular importance by the development of Baltic Sea models. A reasonable model has to include these processes, either by resolving them or by an appropriate parametrization, otherwise the vertical density profiles in the different basins and also the interleaving of the current as shown in Figure 1.3 cannot be reproduced, even less predicted. Consequently it is important to investigate the spatial and temporal variability of entrainment (mentioned in Reissmann et al. 2009) and to explore processes that occur inside the bottom current. E.g. the current is not homogeneous, it shows a transverse density structure and a transverse circulation in the plume by passing a channel (Umlauf and Arneborg 2009). The inflow is characterized by increased turbulence in comparison to the ambient water. Enhanced values are found in the pycnocline where shear is highest and in the bottom layer (Umlauf and Arneborg 2009).

Coastal upwelling

Coastal upwelling, as displayed in Figure 1.3, is a process that occur in several regions e.g. Benguela Upwelling System (Summerhayes et al. 1995) all over the world. The general properties that can explained by linear theory are discussed in section 1.4.3. This section concentrates on the aspect of mixing that is not covered in the analytical theory. In the Baltic Sea there does not exist a classical upwelling region, where coastal upwelling is present most of the year. However, there are 22 regions (Bychkova et al. 1988) where upwelling occurs frequently corresponding to the wind forcing.

In contrast to the analytical theory, coastal upwelling influences the stratification. Isopycnals are forced to lift by upward velocities at the boundary. The Ekman transport advects upwelled water and isopycnals off-shore over lighter surface waters. This instability is degraded by convection. Independently, isopycnals are forced to move upward over sloping topography which results in shear induced convection in the BBL (Reissmann et al. 2009). Both processes lead to a mixing of waters, but they do not necessarily contribute to the diapycnal transport of dissolved tracers from the saline bottom pool to the surface. In summer, the surface layer extents to the thermocline. As long as the thermocline and the mixing depth of the actual wind coincide, the upwelling transports winter water from the layer between thermocline and halocline to the surface. As a consequence, temperature differences of more than $10\,^{\circ}\mathrm{C}$ (Lehmann and Myrberg 2008) can be reached at the surface. This process is important to transport nutrients from the winter water into the euphotic zone. An uplift of waters from the saline bottom pool does not occur, because these waters are protected by the halocline. The conditions change in winter after the erosion of the thermocline. As soon as the surface layer extents to the halocline, an upwelling of saline bottom water into the surface layer is the consequence to upwelling favorable winds. The contribution of upwelling to the whole mixing budget is unknown (Lehmann and Myrberg 2008).

Chapter 2.

Study area, instrumentation and methods

2.1. Study Area

The data sets were collected during cruises in the Bornholm Basin in late summer 2008 (R/V Poseidon) and in late winter 2010 (R/V Alkor). The Bornholm Basin is one of the main Baltic Sea basins, located in the south-western part of the Baltic Sea (Fig. 2.1a) with a depth of $95\,\mathrm{m}$ and a spatial extent of approximately $100\,\mathrm{km}$. The inertial period is about $14.56\,\mathrm{h}$ for a latitude of $55\,^{\circ}\mathrm{N}$. The basin, as shown in Figure 2.1b, is connected to the shallower Arkona Basin via the Bornholm Channel (BC) in the west, and with the larger and deeper Gotland Basin via the Stolpe Furrow (SF) in the east. Figures 2.1c,d show the transect area T1, which is located in the south-east of the basin at a lateral slope. A combination of ship-based transect measurements and moorings was used to investigate mixing processes near the lateral slope. During the cruises, measurements were performed also in the center of the basin near station S1, focusing on mixing processes in the stratified interior, far away from the lateral slopes, as described in detail in van der Lee and Umlauf (2011).

The Bornholm Basin is characterized by a near-bottom pool of saltier water, which has its origin in the North Sea (Reissmann et al. 2009, or section 1.3). The resulting halocline is located at a depth of approximately $60\,\mathrm{m}$ (Fig. 2.2). The halocline varies in depth and width depending on the season and position. However, the presented winter example (station T1A) is comparable to station S1 during winter conditions (van der Lee and Umlauf 2011). In summer, a sharp seasonal thermocline located at a depth of

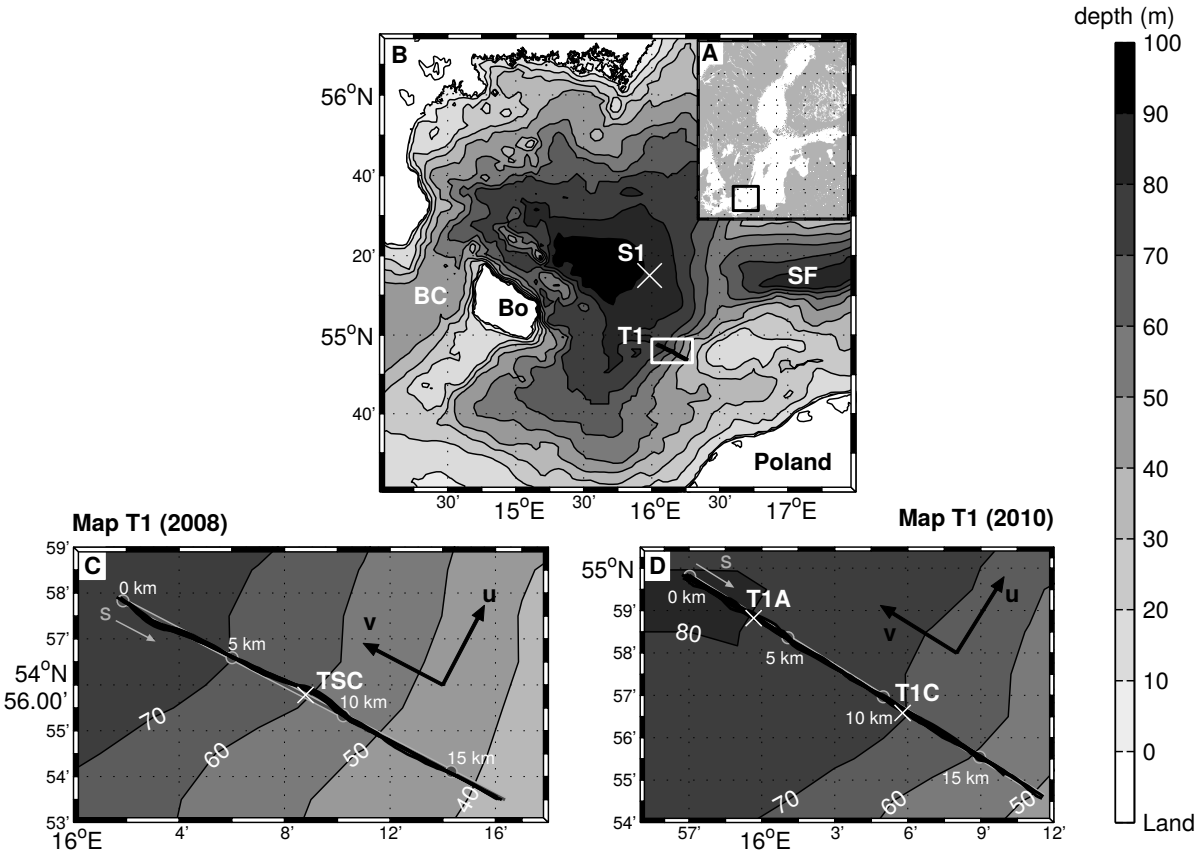

Figure 2.1.: Maps of the Baltic Sea and the study area: (a) Baltic Sea including the Bornholm Basin marked by a rectangle, (b) Bornholm Basin with station S1 and the transect (T1) marked by a rectangle, and (c,d) transect area with transect T1 (transect coordinate s in gray), ship tracks along T1 (black lines), and station and mooring positions (white crosses) in summer 2008 (c) and winter 2010 (d). Note, transect coordinates are not exactly the same in (c) and (d). The rotated coordinate system shown in (c,d) denotes the local along-slope and cross-slope directions (rotation angle: (c) $62°$, (d) $58°$). Exact station positions are described in Tab. 2.2. The abbreviations stand for: BC = Bornholm Channel, Bo = Bornholm Island and SF = Stolpe Furrow. The Figure is modified from Lappe and Umlauf (2016)

approximately $30\,\mathrm{m}$ separates the warm surface layer from a cold intermediate layer. The intermediate water is a remnant of the last cooling period. The potential density σ_θ (Fig. 2.2c) mirrors the described three-layered structure of the water column in summer and is important for the modal structure of the internal-wave field (van der Lee and Umlauf 2011, discussed below). The buoyancy frequency squared is largest in the halocline and reaches values of $N^2 = 5 \times 10^{-3}\,\mathrm{s}^{-2}$ in the center of the basin.

The winter halocline at station T1A (slope region), where the buoyancy frequency squared exceeds values of $N^2 = 6 \times 10^{-3}\,\mathrm{s}^{-2}$, is more strongly stratified and deeper

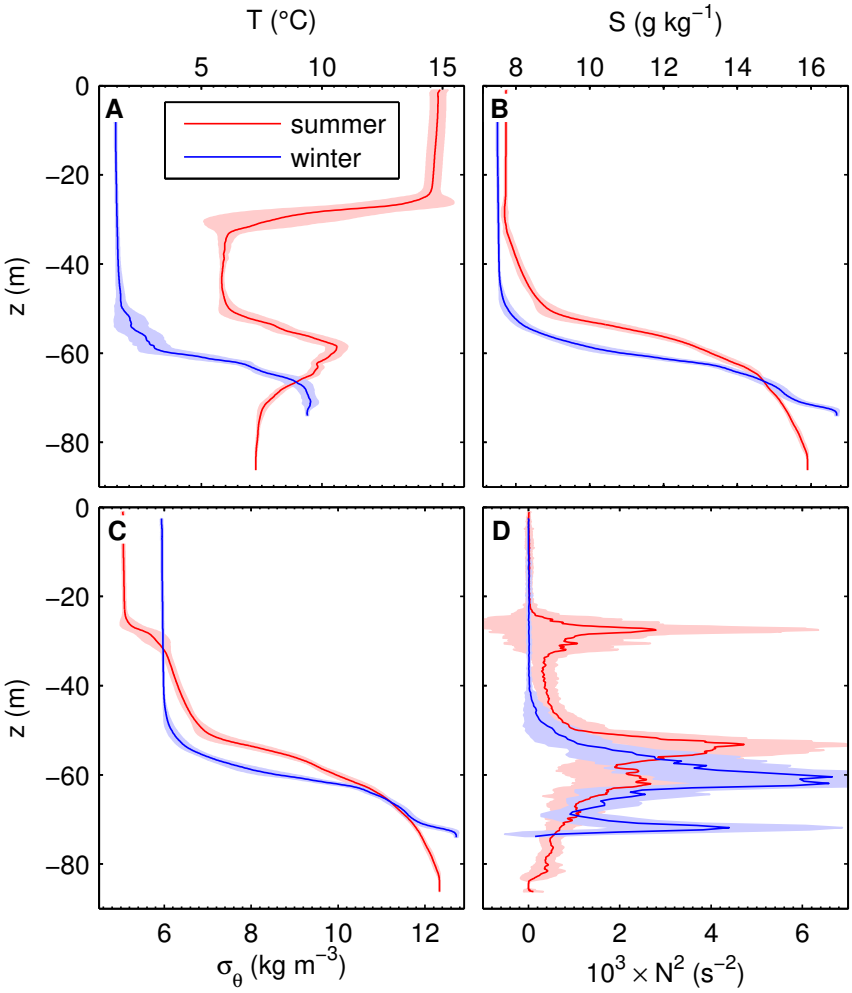

Figure 2.2.: Vertical profiles of (a) in-situ temperature, (b) salinity, (c) potential density $\sigma_\theta - 1000$ kg m^{-3}, and (d) buoyancy frequency squared for station S1 (summer data 2008) and station T1A (winter data 2010). Lines indicate the average profile. Standard deviations marked by shaded surfaces. All profiles are averaged over 407 (158) MSS casts within a $2\,\mathrm{km}$ radius around station S1 (T1A) between yeardays 262.34 and 264.16 (63.90 and 64.59) in 2008 (2010). The profiles of station S1 are taken from Lappe and Umlauf (2016).

by up to $10\,\mathrm{m}$ in comparison to the summer data. In comparison to the slope data (summer) presented in chapter 3, the depth difference increases to $20\,\mathrm{m}$. There, a broad halocline existed, characterized by two less-pronounced maxima at $40\,\mathrm{m}$ and $55\,\mathrm{m}$ depth (Fig. 3.3). During winter conditions, the thermocline erodes and the halocline is sharpened by a combination of winter convection and wind mixing (Reissmann et al. 2009) which is the situation reflected in Figs. 2.2a,b. Near-inertial wave motions, dominated by a mode-2 motion in summer, switch to mode-1 patterns due to

the missing thermocline (van der Lee and Umlauf 2011). Stratification is dominated by the salinity structure in the halocline region, however, with a potentially significant compensation due to inverse temperature stratification (Fig. 2.2a). This point will be discussed in more detail below. Finally, a weakly stratified bottom boundary layer can be identified, topped by a density interface approximately $4\,\mathrm{m}$ above the bottom.

This study is focused on the approximately $17\,\mathrm{km}$ long cross-slope transect T1 in the southern part of the Bornholm Basin (Fig. 2.1c,d).

2.2. Ship-based measurements

During the transects, three instruments were operated from the ship: A free falling turbulence microstructure profiler (MSS) equipped with shear probes and fast responding temperature and CTD sensors, that was operated in yo-yo mode from the stern of the ship, and a vessel-mounted Acoustic Doppler Current Profiler (VMADCP) to obtain current velocity profiles. During some of the transects, current velocities were also measured with an ADCP towed behind the ship (TLADCP, see table 2.1). With the ship steaming at $1 - 2\mathrm{kn}$, the measurements for the whole transect took $5.5\,\mathrm{h}$ to $7\,\mathrm{h}$, which corresponds to approximately half of the inertial period in the Bornholm Basin ($14.56\,\mathrm{h}$, $55\,^{\circ}\mathrm{N}$). This should be kept in mind when comparing measurements that were carried out far away from each other on the transect, as they cannot be directly compared.

In addition to the long transects across the slope of the Bornholm Basin, shorter transects of approximately $80\,\mathrm{min}$ were performed within a $1\,\mathrm{km}$ radius around single mooring stations (Tab. 2.2). These measurements should give a good representation of the dynamics at the mooring location.

2.2.1. Turbulence microstructure profiler

Vertical profiles of turbulence microstructure were performed with a loosely-tethered MSS90-L turbulence microstructure profiler (ISW Wassermesstechnik, Germany). The profiler was deployed from the stern of the ship in a yo-yo mode with a sinking speed of $0.5\,\mathrm{m\,s^{-1}}$ to $0.7\,\mathrm{m\,s^{-1}}$. Depending on the water depth, one profile could be obtained

Table 2.1.: Deployment periods, number of MSS cast and number of ship surveys along transect T1 and near the stations S1 and T1A (also see maps in Figs. 2.1). Times are given in decimal days, 262.00 (62.00) is equivalent to 00:00 UTC on 19 September 2008 (4 March 2010). Gray shaded rows denote station measurements at fixed locations, the exact coordinates are listed Tab. 2.2. Ship surveys complemented by TLADCP measurements are given in parenthesis.

ID	year	deploy period (decimal day)	profiles	transects (with TLADCP)
S1	2008	262.34–264.34	407	
T1	2008	264.70–267.10	797	7 (3–7)
T1A	2010	63.90–64.59	158	
T1	2010	62.77–66.30	694	9 (3–8)

approximately every $5\,\mathrm{min}$. During these measurements, the ship moved with a speed of up to $2\,\mathrm{kn}$ against wind and waves.

The profiler was equipped with high-resolution CTD sensors (Sea and Sun Technology, Germany), a fast response temperature sensor of type FP07, two airfoil shear probes of type PNS06 (ISW Wassermesstechnik, Germany). A sensor protection cage made it possible to obtain vertical profiles down to $0.1\,\mathrm{m}$ above the ground, which is crucial for the estimation of near-bottom mixing rates. The data were sampled at $1024\,\mathrm{Hz}$ resolution. During post-processing, the data were despiked and averaged to $256\,\mathrm{Hz}$ for noise reduction. Differences in response times between temperature and conductivity measurements were taken into account to avoid spikes in the salinity profiles. Finally, the CTD data were averaged to $0.1\,\mathrm{m}$ vertical resolution. The buoyancy frequency derived from the CTD data was averaged to $0.5\,\mathrm{m}$ vertical resolution. Microstructure shear data were divided into 128-point segments and each segment was weighted by a "Hanning window" and zero padded to 256-points in order to increase spectral resolution. The corresponding shear spectra were integrated between 2 cpm (cycles per meter) and an upper bound that was iteratively determined as a function of the Kolmogorov wavenumber (Fer 2006) to obtain estimates of the dissipation rate ε. These estimates were corrected for lost variance (Moum et al. 1995), and finally averaged into $0.5\,\mathrm{m}$ depth bins. The noise level is $\varepsilon \approx 10^{-9}$ W kg^{-1}.

2.2.2. Velocity measurements

The following paragraph is taken from Lappe and Umlauf (2016):
Vertical velocity profiles were obtained at a frequency of $1\,\mathrm{Hz}$ in $2\,\mathrm{m}$ vertical bins with a 300-kHz vessel-mounted Acoustic Doppler Current Profiler (broad-band ADCP from RDI, USA), referred to as VMADCP in the following. Near-bottom velocity data were obtained with a 600-kHz broad-band ADCP from RDI (USA), equipped with a purpose-built depressor wing such that it could be towed, parallel to the microstructure measurements, behind the ship at a given distance above the ground. Data from this towed and lowered ADCP (TLADCP) were transmitted online to the ship, allowing us to adjust the bottom distance as required (typically 20-$30\,\mathrm{m}$). Single-ping velocity estimates from the TLADCP were obtained in 0.5-m bins vertically moving with the instrument, which were ping-wise interpolated to a fixed 0.5-m vertical grid for further processing. Data from both the VMADCP and the TLADCP were finally averaged to 2-minute intervals to decrease the measurement uncertainty.

During the cruise in summer 2008, the salinity of the VMADCP and TLADCP was erroneously set to $35\,\mathrm{PSU}$. As a result the speed of sound and, consequently, the classification of the velocities into the vertical depth bins is incorrect. To minimize the impact of this mistake the speed of sound and the depth bins are corrected as explained in appendix A.2.

2.3. Moored instruments

Several devices were deployed to record velocity, temperature and salinity time series during the cruises in late summer 2008 and early spring 2010. The mooring setups are explained in the following. Mooring positions and deployment times are compiled in Tab. 2.2. The positions are also marked in the maps (Fig. 2.1).

S1 mooring

The following paragraph is taken from Lappe and Umlauf (2016):
A 300-kHz RDI Workhorse Sentinel was deployed between 19 and 27 September 2008, sampling the entire water column (except the surface and bottom blanking regions)

Table 2.2.: Deployment periods, positions and depth of the used moorings (also see maps in Fig. 2.1).

Stations	year	deployment times (decimal day)	Latitude (°N)	Longitude (°E)	depth (m)
S1	2008	262.26–270.55	15.983	55.250	88
TSC	2008	264.54–267.34	16.147	54.930	57.5
T1C	2010	62.63–65.34	54.946	16.097	66.2

at a frequency of 1 Hz in 2-m vertical bins. Data from this instrument were discussed in detail in van der Lee and Umlauf (2011).

TSC mooring

The following paragraphs are taken from Lappe and Umlauf (2016):
A mooring array was deployed that included a bottom-mounted instrument frame with an upward-looking 600-kHz broad-band ADCP from RDI (USA), and a 1.5-MHz Acoustic Doppler Profiler (ADP) from Sontek (USA). Both current profilers provided single-ping estimates at a frequency of 1 Hz, which were averaged over 5 minutes (ADCP) and 2 minutes (ADP), respectively, to reduce the measurement uncertainty. The ADCP sampled the lowest 32 m of the water column with 0.5-m depth bins, while the ADP used 0.05-m to resolve the near-bottom velocity in the lowest 2.7 m.

This instrument frame was accompanied by a nearby CTD chain, recording temperature and salinity at sampling intervals of 15 s. The CTD chain was equipped with three SBE 16 and seven SBE 37-SM CTD loggers from Seabird Electronics (USA), and two TR-1060 temperature sensors from RBR Ltd (Canada), distributed over the lower 31 m of the water column (sensor positions are marked on the y-axis of Fig. 3.2). At a distance of 1 m above the bottom, an upward-looking 600-kHz ADCP (broad-band from RDI) was integrated into this instrument chain, providing velocity estimates at a frequency of 1 Hz in 1-m vertical bins.

T1C mooring

Additionally, a very high-resolution temperature chain equipped with 150 sensors, equally distributed over the first $30\,\mathrm{m}$ above the ground, was deployed at station T1C. These measurements started at 15:00 UTC on 4 March 2010 (yearday 62.625). The sensors were an in-house development of the Royal Netherlands Institute for Sea Research (NIOZ), exhibit an extremely low measurement uncertainty, and use synchronized internal clocks to avoid random vertical time shifts (van Haren et al. 2009). However, during the deployment the sampling rate was erroneously set to $5\,\mathrm{Hz}$, which was too high and therefore caused internal electronic problems resulting in spikes. Data were despiked and time resolution was reduced by averaging to $1\,\mathrm{Hz}$ during post-processing. Corrupted data were blanked and replaced afterwards by a vertical linear interpolation of neighboring sensors.

2.4. Meteorological data

Meteorological data are based on short-term ($12\,\mathrm{h}$) predictions from the high-resolution LME/COSMO-EU model of the German Weather Service (DWD), averaged over a "representative" area of $100\,\mathrm{km} \times 100\,\mathrm{km}$ across the center of the Bornholm Basin. Further, data obtained from the weather station on board of the ship is used in chapter 4. Its resolution was reduced from $1\,\mathrm{min}$ to $1\,\mathrm{h}$ by a third order low-pass filter for noise reduction. The measured wind speed and direction data were found to be in good agreement with the short-term predictions.

2.5. Determination of turbulence parameters

2.5.1. Dissipation rate

The dissipation rate ε of turbulent kinetic energy (TKE), as introduced in equation (1.34), can be estimated for isotropic turbulence based on microstructure shear measurements. Isotropic means that statistical variables are invariant against arbitrary coordinate translations, rotations and reflections. In case of isotropic turbulence, the Reynolds stress tensor $\langle u_i' u_j' \rangle$ satisfies the conditions $\langle u'^2 \rangle = \langle v'^2 \rangle = \langle w'^2 \rangle$ and $\langle u_i' u_j' \rangle = 0$

for $i \neq j$. Considering all turbulent motions in the ocean, isotropic turbulence is an exception. As already indicated in (1.34) the TKE is fed by shear in the mean velocity field, which generates large scale eddies. When turbulent kinetic energy is transfered to smaller scales, i.e. smaller eddies are generated and the anisotropy vanishes. On a molecular level, the TKE is converted in internal energy and background potential energy. This conversion is quantified by the dissipation rate ε and the buoyancy flux G, respectively. The dip of the shear probe has a size of some millimeters and measures the vertical microstucture shear (Appendix A.1.3) generated by turbulence on scales small enough to assume isotropy. The relation between dissipation rate and vertical shear for isotropic turbulence is given as

$$\varepsilon = \frac{15}{2}\nu\left\langle\left(\frac{\partial\tilde{u'}}{\partial z}\right)^2\right\rangle \tag{2.1}$$

$$= \frac{15}{2}\nu\int_0^\infty S(m)\,\mathrm{d}m \quad , \tag{2.2}$$

where ν denotes the molecular viscosity, $\tilde{u'}$ the horizontal velocity fluctuation, z the vertical direction, m the corresponding wave number, and $S(m)$ the vertical shear spectrum. A detailed derivation of equation (2.2) can be found in the Appendix (A.1.1). The dissipation rate is calculated by using (2.2) adapted to the limited measurement resolution as explained in section 2.2.1

2.5.2. Buoyancy flux and flux coefficient

Based on the turbulent kinetic energy (TKE) equation (1.34), Osborn (1980) considered a steady state situation, assuming that the turbulent shear production is balanced by the dissipation rate ε and the buoyancy flux G. This consideration finally results in

$$G = -\gamma\varepsilon \quad , \tag{2.3}$$

where γ is the flux coefficient. Osborn (1980) argues that $\gamma = 0.2$ provides an upper bound for this parameter in many practically relevant situations.

More recent studies (Dunckley et al. 2012; Davis and Monismith 2011; Bluteau et al. 2013; Walter et al. 2014) suggest that the flux coefficient γ exhibits a dependency on the buoyancy Reynolds number $Re_b = \varepsilon/(\nu N^2)$ (ν is the molecular viscosity) in energetic flows. The buoyancy Reynolds number compares the damping scale of

Table 2.3.: Flux coefficient γ parametrization adapted from Osborn (1980), Shih et al. (2005) (SKIF) and Bouffard and Boegman (2013) (BB). Note that SKIF was derived for a Prandtl number of $Pr = 0.7$ (air), but is also well validated for temperature stratified water ($Pr = 7$). BB was derived for $Pr = 700$ (salinity stratified water). The parameterizations are illustrated in Fig. 2.3.

	Molecular	Buoyancy controlled	Transitional	Energetic
BB				
range	$Re_b < 0.18$	$0.18 < Re_b < 96.56$	$96.56 < Re_b < 100$	$100 < Re_b$
γ	0	$0.1 Pr^{-1/2} Re_b^{1/2}$	0.2	$2 Re_b^{-1/2}$
original SKIF				
range	$Re_b < 7$		$7 < Re_b < 100$	$100 < Re_b$
γ	0		0.2	$2 Re_b^{-1/2}$
SKIF				
range	$Re_b < 7$		$7 < Re_b < 100$	$100 < Re_b$
γ	0.2		0.2	$2 Re_b^{-1/2}$
Osborn				
γ	0.2			

stratification $1/N$ with the time scale of fully developed turbulence $\sqrt{\varepsilon/\nu}$ (Ivey et al. 2008). Alternatively, Re_b is the ratio of the Ozmidov to the Kolmogorov length scales to the power of $4/3$ and is therefore a measure of the inertial subrange extent. A $\gamma(Re_b)$-parametrization is given by Shih et al. (2005) and has been shown to yield good results in the ocean for high buoyancy Reynolds numbers (e.g. Walter et al. 2014; Bluteau et al. 2013). Interestingly, this parametrization was derived based on model data for a Prandtl number of $Pr = 0.7$ (air). In Table 2.3 two slightly different versions of this parametrization are given. Both follow Osborn (1980) for moderate buoyancy Reynolds numbers ($7 < Re_b < 100$) and reduce the flux coefficient according to $\gamma = 2 Re_b^{-1/2}$ in the energetic regime. A reduction of the buoyancy flux also occurs for small Re_b because small scale motions are damped by viscous effects. This reduction is considered by a vanishing flux coefficient in the parametrization of Shih et al. (2005, hereinafter referred to as original SKIF) in the molecular regime ($Re_b < 7$). The original SKIF parametrization is often reduced by neglecting the molecular regime, hereafter denoted by SKIF, (in field studies e.g. Fer and Widell 2007; van der Lee and Umlauf 2011; Cyr et al. 2015). For energetic flows this simplification is obvious, but for salinity stratified systems ($Pr \approx 700$) the approach of pure molecular mixing in the

range $Re_b < 7$ is not reasonable since the molecular diffusivity of temperature does not coincide with the turbulent diffusivity of salinity (figure 1 of de Lavergne et al. 2016) for small Re_b. However, turbulent diffusivities of salt and temperature coincide for higher Re_b (Jackson and Rehmann 2014).

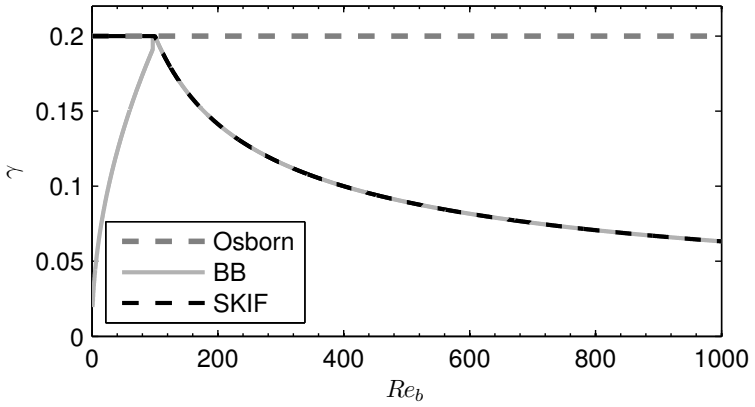

Figure 2.3.: The flux coefficient γ depending on the buoyancy Reynolds number Re_b, see also Tab. 2.3.

Bouffard and Boegman (2013) (hereinafter referred to as BB) recently added a buoyancy controlled regime to original SKIF parametrization based on laboratory and numerical data to guarantee a smooth transition between the molecular and the transitional regime, see also Table 2.3 and Figure 2.3. Moreover, they extended the whole parametrization for salinity stratified waters by introducing a buoyancy controlled regime depending on the buoyancy Reynolds number and the Prandtl number. The data of Salehipour and Peltier (2015) indicates also an additional dependency of the flux coefficient γ on the Prandtl number in the buoyancy controlled regime. The flux coefficients (Fig. 2.3) are reduced in the buoyancy controlled regime, because of turbulent restratification and slow mixing rates. Nevertheless, the γ-parametrization of BB is not well validated yet. In this thesis, the flux coefficient parametrization SKIF is used, because of its validity for mediate and large buoyancy Reynolds numbers, despite the possible overestimation of the flux coefficient at small buoyancy Reynolds numbers.

2.5.3. The bottom boundary layer

The bottom boundary layer (BBL) is defined as the contiguous near-bottom region with $\varepsilon > 8 \times 10^{-9}\,\mathrm{W\,kg^{-1}}$ introduced by Lappe and Umlauf (2016). Summer and winter

data are characterized by patches of bottom-generated turbulence that can clearly by distinguished from the weakly turbulent interior. BBL definitions based on the law of the wall (1.36) or weakly stratified near-bottom layers were found to be inadequate, because the near-bottom layer stays stratified in many regions, even though enhanced turbulence is active.

2.5.4. The mixing efficiency at sloping boundaries

The procedure to approximate the mixing efficiency for realistic slopes and vertical variable stratification was described by Lappe and Umlauf (2016). The following discretion draws heavily on this publication.

Mixing efficiency for an idealized slope

The mixing efficiency

$$\Gamma = \frac{\mathcal{E}_p}{\mathcal{E}} \tag{2.4}$$

is given by Winters et al. (1995) as a ratio of $\mathcal{E}_p$, the rate of irreversible increase of background potential energy due to mixing and $\mathcal{E}$ the rate of irreversible kinetic energy dissipation. Complimenting the generally valid definition for mixing in stratified Boussinesq fluids (2.4), expressions for $\mathcal{E}_p$ and $\mathcal{E}$ are derived by Umlauf et al. (2015):

$$\mathcal{E}_p = \int_0^{h_{\mathrm{BBL}}} \frac{\chi_b}{2N_\infty^2} d\zeta \quad , \tag{2.5}$$

$$\mathcal{E} = \int_0^{h_{\mathrm{BBL}}} \varepsilon d\zeta \quad , \tag{2.6}$$

for an idealized BBL with constant slope angle, constant BBL thickness h_{BBL}, and constant interior stratification N_∞, where χ_b denotes the molecular mixing rate, ε the dissipation rate and ζ the distance to the bottom. The molecular mixing rate is defined as

$$\chi_b = 2\nu_b \Big\langle \frac{\partial b'}{\partial x_i} \frac{\partial b'}{\partial x_i} \Big\rangle \, , \tag{2.7}$$

where ν_b indicates the molecular diffusivity of the stratifying scalar (in the case of the Baltic Sea salinity), b' the fluctuation of buoyancy, $\langle\cdot\rangle$ the Reynolds average and x_i some arbitrary orthogonal coordinates (Umlauf et al. 2015; Umlauf and Burchard 2011). Note that a summation is implied over repeated indices. The advantage of equations (2.5) and (2.6) is that they include the important processes restratification and shear-induced modification of near-bottom shear (Umlauf et al. 2015). Furthermore, the required quantities can be determined by the MSS-profiler provided that a parametrization for the molecular mixing rate is found. The disadvantage is the limited validity of mixing rates and mixing efficiencies for realistic slopes because of the very idealized geometry.

Measurement devices presented in section 2.2 do not enable a direct measurement of the molecular mixing rate (2.7) as can be done from microscale salinity spectra. A parametrization can be found, (a) assuming that the production term in the buoyancy variance equation (e.g. Umlauf et al. 2015) is dominated by the vertical turbulent buoyancy flux as given by Osborn and Cox (1972) as:

$$\chi_b = -2\langle w'b'\rangle N^2 = -2GN^2 \ , \tag{2.8}$$

and (b) using equation (2.3). As a result, the irreversible increase of background potential energy due to boundary mixing is approximated by Lappe and Umlauf (2016) as

$$\mathcal{E}_p = \int_0^{h_{\mathrm{BBL}}} \gamma\varepsilon \frac{N^2}{N_\infty^2} d\zeta \ . \tag{2.9}$$

The latter equation is valid for stably stratified systems, because the Osborn Cox model (2.8) restricts the former validity for arbitrary stratification in (2.5).

Based on the derivations above, the mixing efficiency is defined by Lappe and Umlauf (2016) as

$$\Gamma = \frac{\displaystyle\int_0^{h_{\mathrm{BBL}}} \gamma\varepsilon \frac{N^2}{N_\infty^2} d\zeta}{\displaystyle\int_0^{h_{\mathrm{BBL}}} \varepsilon d\zeta} \ . \tag{2.10}$$

The quotient N/N_∞^2 describing the relationship between stratification within the BBL and far away from the BBL is of particular importance as can be seen in chapters 3 and 4. Starting with the expected case that the stratification is reduced in the BBL,

$N \ll N_\infty$, the mixing efficiency in the BBL is much smaller than the interior value of $\Gamma = 0.2$ (Osborn 1980). This case meets the expectations of Garrett (1979) who stated that boundary mixing is not efficient since it mainly stirs already mixed water. Another approach is that energy is converted into available potential energy. This aspect is analogous to the reduction of mixing efficiency described by Arneborg (2002), where a mixing patch is restratified in a stratified fluid. In contrast, it is also possible that $N \gg N_\infty$ and the bulk mixing efficiency Γ exceeds the single contributions of reduced local flux coefficients and mixing becomes very efficient in the BBL. Furthermore, equation (2.4) also describes the special case $\Gamma = \gamma$. This applies if $N = N_\infty$ and the flux coefficient γ is constant.

Mixing efficiency for realistic conditions

The former equations are valid for an idealized setup including a constant slope angle, a constant stratification in the interior and a BBL that does not vary along the slope. In a realistic setup, these conditions can be assumed to be accurate in limited sections of the slope. A "representative" volume is introduced, bounded by an upper and a lower isopycnal as it was done by Lappe and Umlauf (2016). According to the definitions in (2.5) and (2.6) the average of the mixing and dissipation rates are defined by Lappe and Umlauf (2016) as

$$2N_\infty^2 \overline{\mathcal{E}}_p = \frac{1}{M} \sum_{i=1}^{M} \chi_b^{(i)} \,, \quad \overline{\mathcal{E}} = \frac{1}{M} \sum_{i=1}^{M} \varepsilon^{(i)} \,, \tag{2.11}$$

where $\chi_b^{(i)}$ and $\varepsilon^{(i)}$ indicate single estimates of the mixing and dissipation rate within the BBL sub-volume and M denotes the total number of available estimates in the sub-volume. Mixing rates $\chi_b^{(i)}$ are calculated according to equations (2.7) and (2.3). An exception is made in unstable regions, because they do not contribute to mixing in the BBL (Umlauf and Burchard 2011; Umlauf et al. 2015) and $\chi_b^{(i)}$ is set to zero accordingly. Close to the bottom, turbulence is limited by the distance to the boundary, as described at the end of section 1.5.2. This effect is not included in the parametrization for the flux coefficient γ (section 2.5.2). The uncertainty of the estimated bulk mixing rate $\Gamma = \overline{\mathcal{E}}_p / \overline{\mathcal{E}}$ is illustrated by presenting two extreme cases in chapter 3 and 4: a) single estimates of $\chi_b^{(i)}$ are calculated as described above and are not influenced by the fact that $L_O > \kappa\zeta$, and b) $\chi_b^{(i)} = 0$ for $L_O > \kappa\zeta$.

The determination of a representative value for N_∞^2 is of particular importance due to the impact to the mixing efficiency in (2.10) discussed above. In the investigations, the stratification is averaged between the upper and lower isopycnal (see also "representative" volume above) at some distance to the sloping boundary. As a reason, Lappe and Umlauf (2016) stated: "BBL mixing inside a given density range will ultimately modify interior stratification in the same density range."

Chapter 3.

Boundary mixing under summer conditions

This chapter is focused on bottom boundary mixing at lateral slopes forced by near-inertial waves during summer conditions. Parts of the results presented here are already published in *Journal of Geophysical Research: Oceans* under the title "Efficient boundary mixing due to near-inertial waves in a non-tidal basin: Observations from the Baltic Sea" (Lappe and Umlauf 2016). Individual aspects of the published study, which are not within the scope of this thesis, are left out or only shortly summarized, a detailed derivation can be found in Lappe and Umlauf (2016). If not noted otherwise, all of the here presented data analysis were performed by myself, findings from other studies are clearly marked and referred to. There is no conflicting interest with the Co-Author of the above mentioned publication.

3.1. Introduction

The data presented in this chapter were collected during an extensive field campaign in the center and at the lateral boundary of the Bornholm Basin in summer 2008. The study site is characterized by typical summer stratification as discussed in section 2.1. The data include moored and ship-based ADCP measurements, high resolution turbulence microstructure observations, as well as time series of moored salinity and temperature loggers (sections 2.2 and 2.3). The study presented in the following chapter is focused on the processes within the bottom boundary layer (BBL, section 2.5.3) at the lateral slope.

The chapter is structured as follows: In section 3.2, velocity time series, successively recorded at the center of the basin and at the slope, are compared. The data of the center position were analyzed by van der Lee and Umlauf (2011) and are shortly summarized here. Near inertial wave motions dominate the velocity field in the center (van der Lee and Umlauf 2011) and they are also omnipresent at the slope. The temporal and spatial variations in the velocity field, the stratification, and energy dissipation at the slope are investigated in section 3.3. Several near-bottom regions with different characteristic features are identified and analyzed in section 3.4. High mixing rates and a bulk mixing efficiency comparable to the mixing efficiency of the interior is found in a near-bottom region above the halocline. It is shown that the overall energy dissipation and mixing in the Bornholm Basin above the halocline is dominated by boundary layer mixing (section 3.5). The chapter is closed with the conclusions in section 3.6.

3.2. Current velocity structure in the Bornholm Basin

3.2.1. Temporal variability at the basin center

Velocity series obtained with a moored ADCP (see section 2.3) provide an overview of the current velocity structure at station S1 in the center of the Bornholm Basin (Fig. 2.1). As visible in Figure 3.1, the velocity field is dominated by near-inertial wave motions, oscillating with a frequency slightly above the inertial frequency (van der Lee and Umlauf 2011). These kind of oscillations are characterized by vertical phase shifts in stratified environments, indicating here the presence of the sharp thermocline at approximately $30\,\mathrm{m}$ depth and the broad halocline in the depth range between $50\,\mathrm{m}$ and $70\,\mathrm{m}$. Figure 3.1 is based on the data set analyzed in detail by van der Lee and Umlauf (2011). The authors decomposed the velocity field in eigenfunctions and eigenvalues as explained in section 1.4.3 and showed that it is energetically dominated by baroclinic mode-2 near-inertial waves. The near-inertial waves are generated at the lateral boundaries as a response to increased winds and propagate to the basin center. Incoming near-inertial wave modes are characterized by an increase in velocities and kinetic energy within the water column between yearday 266 and 267. Van der Lee and Umlauf (2011) found that the analytical solution for a stratified ocean bounded by a coast and forced by wind under strongly simplified assumptions (constant depth, vertical walls as lateral boundaries and a well-defined increase in wind, see e.g. Kundu

et al. 1983) already well explains the observed motions in the center of the Bornholm Basin.

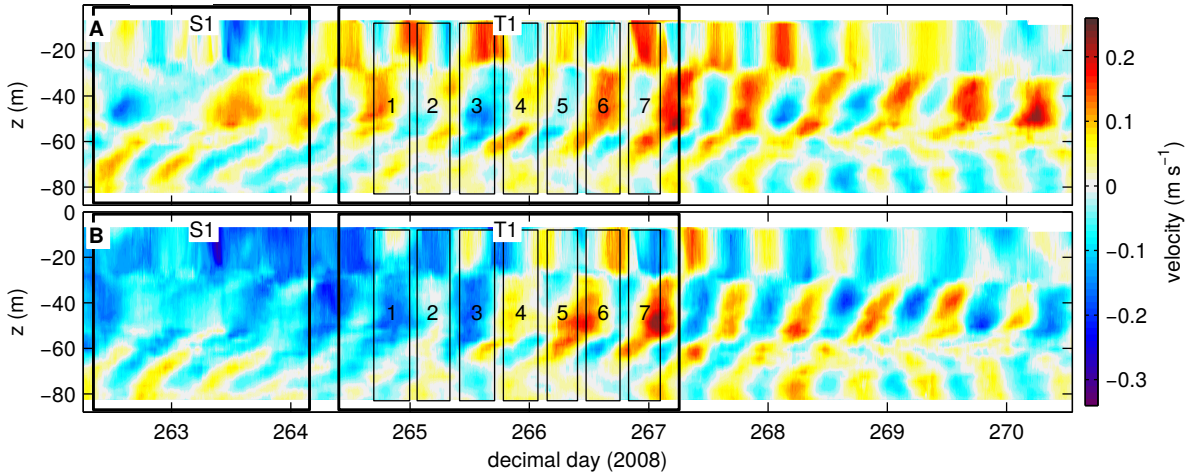

Figure 3.1.: Time series of (a) eastward velocity and (b) northward velocity from the bottom-mounted ADCP at the central station S1 (Fig. 2.1). Bold rectangles denote the periods of ship-based measurements near station S1, and the overall mooring deployment times on transect T1, respectively. Light rectangles show the times of the seven individual ship surveys along transect T1. The Figure is modified from Lappe and Umlauf (2016).

Van der Lee and Umlauf (2011) show that shear layers within the halocline are established by higher baroclinic near-inertial wave modes. These shear layers are closely associated with narrow bands of enhanced dissipation rates and provide an important contribution to cross halocline mixing in the water column. This investigation was based on turbulence measurements performed by van der Lee and Umlauf (2011) at the center station S1 in the time interval marked by the rectangle labeled “S1” in Figure 3.1.

The dominance of low-mode near-inertial motions, explained above, is not a general property of the Baltic Sea. For example, in the central Baltic Sea basin-scale topographic waves (sub-inertial motions) contribute a large fraction to the kinetic energy (Holtermann and Umlauf 2012; Holtermann et al. 2014).

3.2.2. Temporal variability at the slope

At the slope, a combination of three different ADCPs and CTD sensors (section 2.3) was deployed at station TSC (Fig. 2.1). The total measurement duration is indicated in

Figure 3.1 by the ”T1“ marked rectangle. Along-slope and cross-slope (cross-isobath) velocities (Figs. 3.2, 2.1) exhibit clock-wise-rotating, near-inertial wave motions, similar to the ones found at station S1. Velocities are characterized by a distinct $180°$ phase shift across the thermocline and a smooth shift across the broad halocline. The presence of dominant mode-2 near-inertial waves can be clearly seen. The high variability of the velocity patterns in the halocline is caused by higher near-inertial wave modes. Velocity amplitudes are of the order of $0.15\,\mathrm{m\,s^{-1}}$, a bit lower than at station S1 (Fig. 3.1). Near-inertial motion amplitudes below the halocline are largest on day 265, two days before amplitudes reach maximum values at the center position, possibly as a response to a former increase in winds (not shown). This feature is in line with the idea that near-inertial waves are generated at the lateral boundaries rather than in the interior (van der Lee and Umlauf 2011).

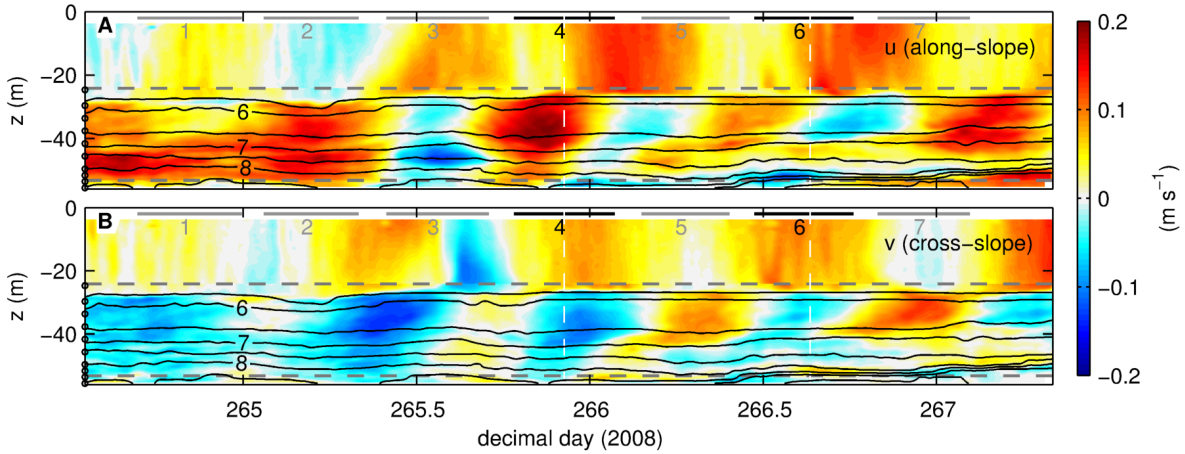

Figure 3.2.: Time series of (a) along-slope velocity, (b) cross-slope velocity (Fig. 2.1). The velocity data are a composite from three bottom-mounted instruments, separated by the dashed gray lines: low-resolution 600-kHz ADCP (top), high-resolution 600-kHz ADCP (middle), and 1.5-MHz ADP (bottom). Black contour lines indicate isopycnals every half $\mathrm{kg\,m^{-3}}$ derived from moored CTD loggers (positions denoted by black circles). All data are 1-h low-pass filtered to remove high-frequency motions. Individual ship surveys (MSS,VMADCP and TLADCP) along transect T1 are marked by horizontal bars at the top; times when the ship passed mooring position TSC are indicated as white dashed lines. The Figure is modified from Lappe and Umlauf (2016).

A weak signal of near-inertial waves was also found in the isopycnal motions (Fig. 3.2) computed from 10 CTD loggers distributed between thermocline and bottom. Individual loggers are marked by small circles on the left hand side of the panels in Figure 3.2. Vertical isopycnal displacements are mostly smaller than $2\,\mathrm{m}$, indicating

that fluctuations in potential energy are small. This property and the fact that the Burger number fulfills $S_i \ll 1$ (Lappe and Umlauf 2016, $S_i = c_i/(Lf)$, where c_i denotes the mode speed, L the lateral scale of the basin and f the Coriolis parameter) for the lowermost modes match the theory for near-inertial motions in closed basins (Antenucci and Imberger 2001; Csanady 1967), where the ratio of potential and kinetic energy becomes small if $S_i \ll 1$. Furthermore, a strong up- and downwelling, and a compression of isopycnals is observed in the lowest meters above the bottom as a result of up and down-slope moving isopycnals (see also Fig. 3.3). Cross-slope velocities and density gradients in the near-bottom region explain this behavior.

Shear bands deduced from the velocities in Figure 3.2 had a width of several meters and are correlated over time scales comparable to the inertial period (Lappe and Umlauf 2016). It was also shown in Lappe and Umlauf (2016) that the Richardson number $Ri = N^2/S^2$ (ratio of shear squared and buoyancy frequency squared) measured in the shear bands may be close to the threshold for shear-instabilities.

3.3. Spatial variation at the slope

Seven cross-slope ship surveys were performed along transect T1 (Fig. 2.1c) to investigate the spatial variability of boundary mixing along the basin slope. The individual measurement intervals are marked by a numbered box/bar in Figures 3.1 and 3.2. Turbulence microstructure observations were complemented by a combination of VMADCP and TLADCP measurements, as described in more detail in section 2.2. The investigated near bottom turbulence varies strongly along the transect and also between the individual surveys. A comparison between data from survey 4 and 6 (gray bars in Fig. 3.2) clearly illustrates this variability: The measurements during survey 4 exhibit strongly enhanced energy dissipation within a broad BBL. In contrast, the energy dissipation during survey 6 is weaker and the BBL volume is significantly smaller. Turbulence in the BBL during the remaining surveys lies in between these extreme cases.

3.3.1. Situation with strong boundary mixing (survey 4)

The general properties of the flow regime, as discussed in section 2.1 can also be found in the observational data along the transect of survey 4. The vertical stratifi-

cation (Fig. 3.3c) is characterized by a sharp thermocline at a depth of approximately $30\,\mathrm{m}$ and a broad halocline split in an upper branch at a depth of $40\,\mathrm{m}$ and a lower part between $45\,\mathrm{m}$ and $60\,\mathrm{m}$. In the shallower part of the transect, the thermocline and the upper branch of the halocline are lifted. This is a feature commonly found to different extents in every survey and may be the result of the cross-slope Ekman transport in the surface layer generated by north-easterly winds during the measurements (Lappe and Umlauf 2016). The along-slope and cross-slope velocities are shown in Figure 3.3a,b. As a reminder, a single survey was measured within $7\,\mathrm{h}$, which is approximately half of the inertial period ($T_f = 14.56\,\mathrm{h}$). Consequently, the velocity data is strongly influenced by the dominating signal of near-inertial wave oscillations. Nevertheless, velocity patterns (Fig. 3.3a,b) indicate the presence of a) a strong shear layer in the thermocline, b) several shear layers within the halocline, and c) shear above the sloping bottom, which is not resolved by the velocity data (see unresolved velocities above the bottom). Strong shear can be still assumed in the unresolved part because the lowermost measured velocities has to vanish to the bottom. A prominent shear layer in the halocline is marked by region I. This shear layer coincides with a thin band of enhanced dissipation (Fig. 3.3d) and is an example for an interior mixing region as mentioned above and as discussed by van der Lee and Umlauf (2011). This bands are stable in time for several hours (van der Lee and Umlauf 2011; Lappe and Umlauf 2016) and can have a spatial extent of a few kilometers (Fig. 3.3a,b,d). Lappe and Umlauf (2016) suggest that this band may be related to high-frequency wave-like motions.

Besides thin bands of enhanced dissipation rates in the interior and strong turbulence in the surface layer, strongly enhanced energy dissipation is found directly above the bottom. Enhanced near-bottom turbulence is mostly confined to the BBL (see definition in section 2.5.3), marked with a gray line in all panels of Figure 3.3. Enhanced turbulence levels and the vertical extent of the turbulent BBL coincide with regions of enhanced near-bottom shear (Fig. 3.3a,b,d) which is induced to a large extent by near-inertial motions. Isopycnals (Fig. 3.3) exhibit no characteristic of large scale overturns related to the critical reflection of internal waves (Eq. (1.35)). It is therefore valid to assume that near-bottom turbulence is caused by frictional effects.

The turbulent BBL is characterized by enhanced dissipation (Fig. 3.3d) and by small stratification (Fig. 3.3c) in the deeper part of the transect, where slope angles are small. This region is marked by IV and is located below the halocline. The properties of this BBL are similar to the properties found in the BBL of the center (van der Lee and

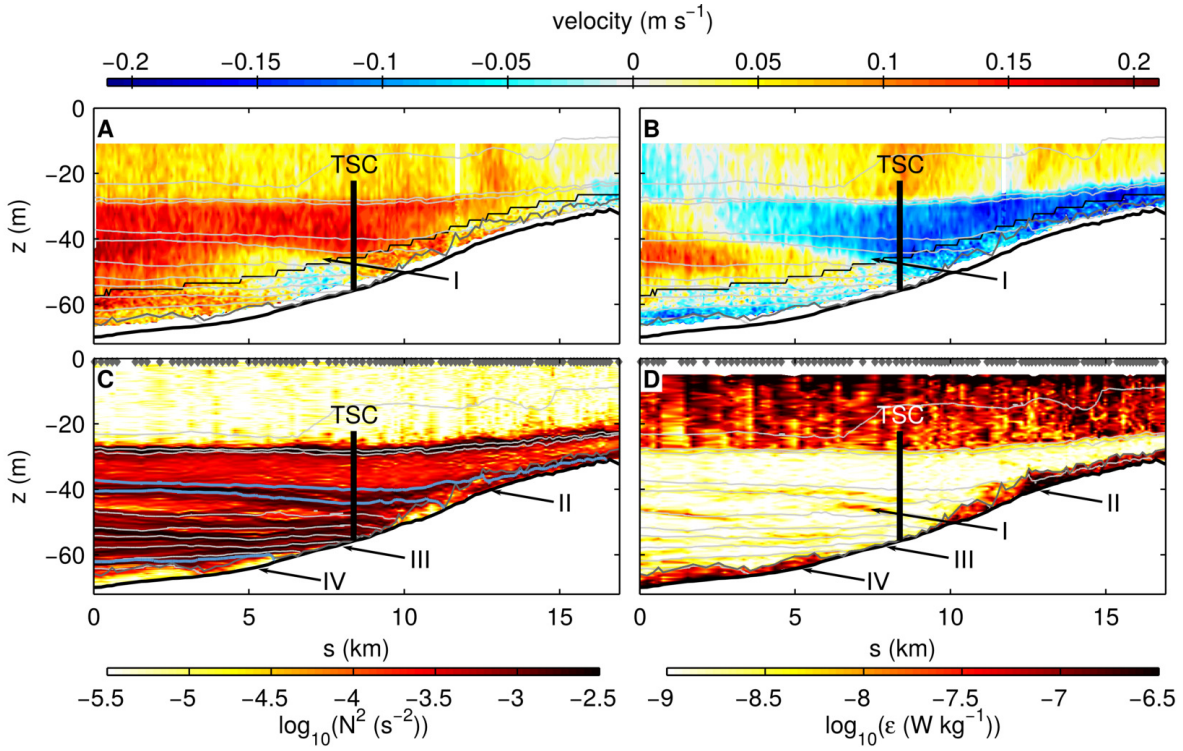

Figure 3.3.: Cross-slope transect of (a) along-slope velocity, (b) cross-slope velocity, (c) buoyancy frequency squared, and (d) dissipation rate. Data are taken along transect T1 during ship survey 4 (numbering of surveys is indicated in Figs. 3.1 and 3.2). Light gray lines denote isopycnals at 0.5 kg m^{-3} intervals, starting with $\sigma_\theta = 5$ kg m^{-3} at the top (some selected isopycnals are marked in blue, see Tab. 3.1). The BBL thickness is indicated by the dark gray line. Velocities in panels (a) and (b) are a composite of the vessel-mounted (above black line) and towed ADCPs. Along- and cross-slope directions are indicated in Fig. 2.1c. Gray markers at the top of panels (c) and (d) indicate individual microstructure casts. Vertical black lines illustrate the location and extent of the CTD chain at position TSC (see Fig. 2.1c). The Figure is taken from (Lappe and Umlauf 2016).

Umlauf 2011). Thus, region IV can be seen as an example of a classical entrainment driven BBL over a flat bottom. The structure of the BBL is different above the halocline in region II. Here, strong stratification and enhanced dissipation occur jointly, indicating high mixing rates that will be discussed below. Interestingly, the stratification is maintained in region II during all seven ship surveys. The reason for this effective restratification is the upslope advection of the upper part of the halocline. A restratification of the BBL in the vicinity of a sloping bottom was already found in (Umlauf and Burchard 2011). The authors also observed that steep slopes are more favorable for this restratification. Weak turbulence is found in region III where the broad halocline intersects with the sloping boundary. The development of a BBL is prevented by strong

restratification and the damped near bottom shear resulting from the low velocities in the halocline, which is an inflection point for internal waves modes (van der Lee and Umlauf 2011) in this area. In consequence, the vanishing BBL does not contribute to cross halocline mixing.

The introduced regions II – IV (e.g. Fig. 3.3) can be identified in every ship survey along transect T1 (Fig. 2.1) although near-bottom turbulence exhibits a strong spatial and temporal variability.

3.3.2. Situation with weak boundary mixing (survey 6)

Dissipation rates (Fig. 3.4d) are evidently increased in the surface layer during survey 6 as a consequence of stronger wind forcing (Lappe and Umlauf 2016). Increased wind speeds are typically followed by an intensification of velocities in the water column, after the arrival of internal waves that are generated at the boundary (analytical theory, section 1.4.3). However, a corresponding energy transfer is not visible in the observed data, and had presumably not happened yet. Velocities (Fig. 3.4a,b) are even weaker than in the case discussed above. Accordingly, turbulence levels are reduced in the water column below the thermocline and also in the BBL. In fact, the BBL turbulence level observed during this survey is lowest among all measurements that were carried out. Nevertheless, shear layers of several kilometers length are found in the halocline, coinciding with bands of enhanced dissipation rates. Two examples are marked by I in Figure 3.4a,b,d. Lappe and Umlauf (2016) showed that the band of enhanced dissipation rates passing the TSC mooring is also stable in time for several hours. Dissipation rates and stratification are again enhanced in the BBL region II, above the halocline. Region IV, characterized by a BBL with enhanced dissipation rates and low stratification, is found below the halocline as in survey 4. However, the BBL volume in this specific region is small compared to the corresponding region in survey 4. Turbulence levels of region IV are marginally larger than in region III, where near-bottom turbulence is suppressed by stronger stratification within halocline.

In contrast to the other surveys, a special feature can be found between the broad and the upper branch of the halocline near the slope, marked by V (Fig. 3.3c,d). This feature is characterized by large isopycnal excursions and patches of reduced stratification, increased strain rates and increased turbulence levels. The data set does not permit to identify the origin of this feature, but it can be speculated that it is a result

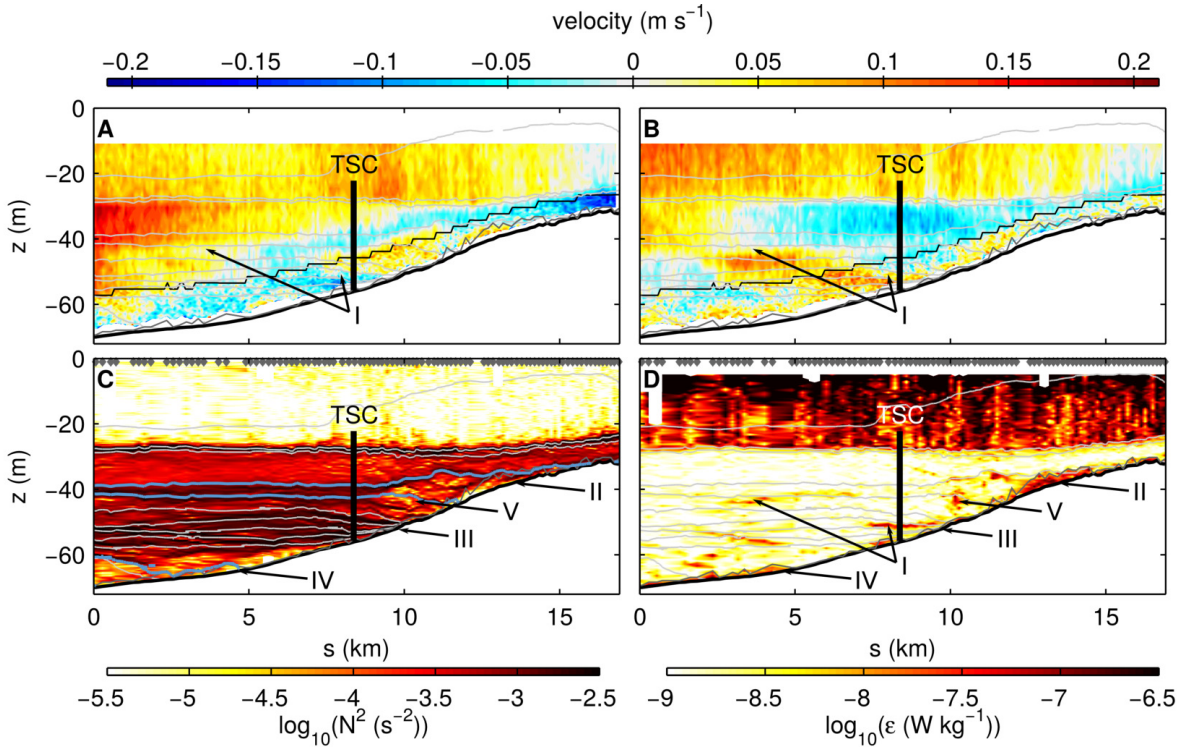

Figure 3.4.: As in Fig. 3.3 but now for ship survey 6. The Figure is taken from Lappe and Umlauf (2016).

of a near-critical interaction of internal waves with the slope. According to equation (1.35), the condition for critical reflection is partly fulfilled for the given slope angle range and parts of the broad-band frequency range of near-inertial motions. However, a feature of this kind only occurred in survey 6, and thus its overall contribution to boundary mixing at all seems to be low.

3.4. Mixing and mixing efficiency in the BBL

The two surveys presented in the last section exemplarily illustrate the temporal and spatial variability of near-bottom turbulence (Figs. 3.3d, 3.4d) along transect T1 (Fig. 2.1). Two different BBL regions above (II) and below (IV) the halocline were identified as areas with enhanced levels of turbulence and therefore potential candidates for enhanced mixing. Both regions are characterized by the existence of distinct BBLs above and below the halocline for every survey. As a reminder, the BBL vanished within the halocline region. Based on the explanations in section 2.5.4, boundary mixing is evaluated in the following. All estimates for the local mixing efficiency χ_b

are illustrated in a scatter plot for both BBL regions and all seven ship surveys in Figure 3.5. Individual χ_b's are calculated according to equation $\chi_b = \gamma \varepsilon N^2$ (Eqs. (2.8), (2.3)). The flux coefficient γ is determined by the SKIF-parametrization (Tab. 2.3).

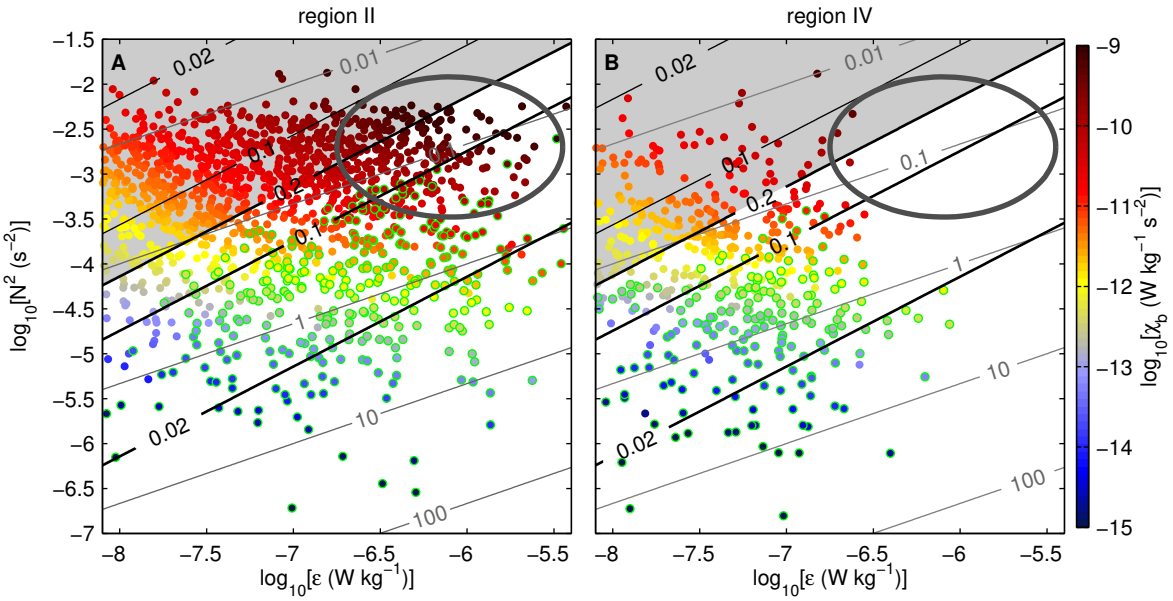

Figure 3.5.: Mixing rate χ_b inside the BBL as a function of stratification and dissipation rate for data points (a) inside region II and (b) inside region IV (data include all seven ship surveys on transect T1). Gray lines show the Ozmidov scale L_O (in meters). Thick black lines indicate the flux coefficient γ according to SKIF (Tab. 2.3), where the gray area corresponds to $\gamma = 0.2$ (SKIF). Thin black lines inside the gray area indicate the reduced mixing efficiencies suggested by Bouffard and Boegman (2013) (BB in Tab. 2.3) for salinity-stratified flow at low Re_b. Data points affected by wall turbulence ($L_O > \kappa\zeta$) are marked in green. The Figure is taken from Lappe and Umlauf (2016).

Region II, located above the halocline, is characterized by dissipation rates and buoyancy frequencies covering several orders of magnitude, respectively. Highest mixing rates are found where enhanced dissipation rates coincide with strong stratification. The corresponding area is marked by an ellipse in the scatter plot (Fig. 3.5a) and provides the largest contribution to BBL mixing. The stratification in the BBL is in the order of $N^2 = 10^{-3}\,\mathrm{s}^{-1}$, comparable to (or even higher than) the stratification in the interior region (Fig. 2.2). The vertical scale of turbulent eddies is described by the Ozmidov scale L_O (1.38) in a stratified surrounding. It ranges between centimeters and a few decimeters in the BBL (see gray lines in Fig. 3.5). Accordingly, turbulent overturns are not influenced by the presence of the bottom in a large part of the BBL. This is not the case for areas where the eddy size is limited by the distance to the bottom

(Eq. 1.37), i.e. , where $L_O > \kappa\zeta$ applies. Corresponding data is marked by green circles in Figure 3.5, and is almost exclusively located in the lowermost bins, directly above the bottom. As a reminder, all data discussed in this section is defined in the center of a $0.5\,\mathrm{m}$ vertical bin (see also section 2.2.1). The flux coefficients γ (Tab. 2.3) are larger than 0.1 (black lines in Fig. 3.5), also for strongly enhanced dissipation rates, because strong stratification suppresses a strong increase in buoyancy Reynolds numbers in the BBL. It was mentioned in the discussion above that the strong stratification in region II is a consequence of the upslope advection of the upper part of the halocline (Fig. 3.3c). Moreover, Lappe and Umlauf (2016) suspect that the internal pressure gradient induced by the presence of a sloping bottom leads to BBL restratification (e.g. Garrett 1991; Umlauf and Burchard 2011).

The determination of the bulk mixing efficiency Γ at sloping boundaries was explained in section 2.5.4. As a first step, "representative" sub volumes are defined in the BBL region II. The water volume contained in the "representative" part, as well as the bounding isopycnals, is listed in table 3.1, respectively. These isopycnals are also marked in Figures 3.3c and 3.4c. A "representative" interior stratification N^2_∞ (Tab. 3.1) is found by averaging the stratification of the central station S1 (Fig. 2.2) in the listed density range (Tab. 3.1) for every survey. Estimates of the averaged dissipation and mixing rates, as well as the resulting bulk mixing efficiencies, are listed in Table 3.2. Three approaches are presented to evaluate the data characterized by $L_O > \kappa\zeta$, where turbulent overturns are limited by the distance to the bottom. In those regions, the conditions for using the SKIF γ-parametrization (Tab. 2.3) are not fulfilled, as explained in section 2.5.4. The three approaches are: (a) excluding the data discussed above ("excluded"), (b) including the data and ignoring that the SKIF parametrization is not valid if $L_O > \kappa\zeta$ ("included") and (c) including the data and setting the mixing efficiency to zero if $L_O > \kappa\zeta$ ("zero mixing"). In the "excluded" case, a bulk mixing efficiency $\Gamma = \overline{\mathcal{E}}_p/\overline{\mathcal{E}}$ (section 2.5.4) of 0.42 is found in region II, which is twice as high as the mixing efficiency of the interior of 0.2 (Osborn 1980). The unrealistically high mixing efficiency can be explained by the fact that a huge part of the energy dissipation takes place directly above the bottom and does not contribute to the averaged dissipation rate $\overline{\mathcal{E}}$ (Eq. 2.11) in the "excluded" case. When including near-bottom data, as done in the approaches "included" and "zero mixing", the averaged dissipation rate is strongly increased. Local mixing rates χ_b are calculated different in the "included" and "zero mixing" case, but the difference in the irreversible increase of background potential energy due to boundary mixing $\overline{\mathcal{E}}_p$ (Eq. 2.11) and the averaged mixing rate (Tab. 3.2) is small, confirming that the contribution of the areas

characterized by $L_O > \kappa\zeta$ to the averaged mixing rate and to overall mixing is small. This is a robust result and suggests that the approaches including all near-bottom data are the more realistic approaches. The bulk mixing efficiency is in both cases slightly above the canonical value of 0.2.

Table 3.1.: BBL volumes (per along-slope unit length), BBL density intervals, and corresponding N^2_∞ values for regions II and IV, respectively, based on data from station S1. The Table is taken from Lappe and Umlauf (2016).

transect	BBL volume (10^4 m^2)		σ_θ range (kg m^{-3})		N^2_∞ (10^{-3} s^{-2})	
	region II	region IV	region II	region IV	region II	region IV
1	1.34	0.23	6.5–7.5	10.1–10.2	0.77	2.7
2	1.65	0.23	6.5–7.5	10.0–10.2	0.77	2.8
3	0.97	0.12	6.5–7.5	10.0–10.1	0.77	2.9
4	2.61	1.82	6.5–7.0	9.7–10.1	0.50	2.1
5	1.35	1.35	6.5–7.0	9.5–10.1	0.50	2.1
6	1.09	0.60	6.5–7.0	10.0–10.1	0.50	2.9
7	1.47	1.85	6.5–7.0	9.5–10.1	0.50	2.1

Table 3.2.: Average dissipation and mixing rates defined in (2.11), and bulk mixing efficiency, for regions II and IV, respectively. For each region, near-bottom data with $L_O > \kappa\zeta$ are either excluded (first row), included (second row), or assumed to provide no contribution to mixing ($\chi_b = 0$, third row). Mixing efficiencies are computed based on N^2_∞ at the central station S1 compiled in Tab. 3.1. The Table is taken from Lappe and Umlauf (2016).

region	near-bottom data	$\overline{\mathcal{E}}$ (10^{-7} W kg^{-1})	$N^2_\infty \overline{\mathcal{E}}_p$ (10^{-11} W kg^{-1} s^{-2})	$\Gamma = \overline{\mathcal{E}}_p / \overline{\mathcal{E}}$
II	excluded	2.04	5.68	0.42
	included	2.85	4.28	0.23
	zero mixing	2.85	4.07	0.22
IV	excluded	0.51	0.337	0.031
	included	0.83	0.193	0.011
	zero mixing	0.83	0.185	0.010

Besides the discussed approaches, the measurement routine introduces some further uncertainty, because the lowermost centimeters of the water column are missing in the data, as a sensor protection frame is installed and the routine to determine the bottom cuts off some useful data (also see appendix A.3). A rough estimate to take the unresolved energy dissipation in the lowest centimeters into account is to double ε in the lowermost $0.5\,\mathrm{m}$ data bin. This estimate is based on the idea that the missing dissipation can be calculated based on the law of the wall, even though the lowermost bin is not perfectly well-mixed in every MSS cast. However, it can easily be shown that more than $50\,\%$ of total energy dissipation in the lowermost data bin may occur in the unresolved region above the bottom. Based on this estimate, the bulk mixing efficiency would further reduce to $\Gamma \approx 0.15$ (Lappe and Umlauf 2016), which is still close to the value of mixing efficiency in the interior of 0.2. This result clearly show, that boundary mixing driven by bottom friction can be efficient, if the BBL is permanently restratified.

Another turbulent BBL region is located below the halocline (region IV) and is characterized by small stratification. Furthermore, dissipation rates do not reach the enhanced values found in region II (Fig.3.5). In consequence, enhanced mixing rates as known from the discussion above are missing, which can also be seen by the not existing data within the marked ellipse (Fig.3.5b). The total amount of data points and correspondingly, the covered water volume is smaller than in region II. Furthermore, the portion of data points that fulfill the condition $L_O > \kappa\zeta$ is increased by one order of magnitude in comparison to region II. However, it should be considered that region IV may extent beyond the measurement section. Nevertheless, averaged dissipation and mixing rates (Tab. 3.2) are calculated as described for region II above. It should be kept in mind that the density structure of the "representative" sub volume is more variable here, compared to region II. The lower isopycnal of the "representative" sub volume (Tab. 3.1) is set to the highest density found in the deep part of the transect for every survey and consequently does not appear in the Figures 3.3c and 3.4c. The upper isopycnal is readjusted for every survey and is determined by the vanishing BBL between region IV and III (e.g. Fig. 3.3). The density range and the covered BBL volume for region IV and the corresponding interior stratification are again listed in Table 3.1. The averaged dissipation rate is approximately one third and the averaged mixing rate $1/20$ of the reference values given by region II (compare "included" cases). As a consequence of a smaller averaged dissipation rate, a smaller bulk mixing rate and a smaller available volume (in comparison to region II), region IV provides only a small contribution to net energy dissipation and overall mixing (Lappe and Umlauf 2016).

However, region II and region IV are located in different parts of the water column and contribute to mixing in their density ranges. Region IV may have a relevance for mixing of the deep water below the halocline. The bulk mixing efficiency Γ is 0.011 for the "included" case and is much smaller than in region II. The order of magnitude of Γ corresponds to the results of Umlauf and Burchard (2011), who investigated stratified BBLs on sloping topography using idealized numerical simulations.

3.5. Basin-scale impact of boundary mixing

In the following, estimates of the ratio of interior and BBL energy dissipation and mixing are derived for the Bornholm Basin. These estimates are based on the data discussed above, which were recorded on a few consecutive days, at the center position S1 and on the slope transect T1 (Fig. 2.1) in late summer. Both observations are in principle point measurements with restricted temporal and spacial significance. The deduced estimates about the ratio of interior and BBL mixing can therefore only be rough estimates. Moreover, the dynamics in the Bornholm Basin can not be explained by the simplified Baltic Sea overturning model (Fig. 1.3) developed for the Baltic Proper, because lateral advection mainly determines the temporal evolution of the stratification (Meier 2007; Feistel et al. 2008). The contribution of diapycnal mixing is of minor importance. Hence, a complete mixing budget including, e.g. ,estimates of the vertical diffusivities, is not the aim of this study. Nevertheless, it is important to understand which mixing process, interior or BBL mixing, is dominant in the Bornholm Basin.

Lappe and Umlauf (2016) suggest that the horizontal cross sectional area $A(z)$ can be split in a contribution for the interior and BBL mixing for every depth. Using a simplified circular basin geometry (radius $r = 50\,\mathrm{km}$) they derived the ratio

$$\frac{A_{\mathrm{BBL}}}{A_i} = \frac{2h_{\mathrm{BBL}}}{r \sin\alpha}\,, \tag{3.1}$$

where A's denote the horizontal cross-sectional areas of the BBL (denoted by the subscript BBL) and the interior (subscript i), h_{BBL} the averaged BBL thickness, r the radius of the basin and α the slope angle. In combination with the averaged dissipation rates of the interior $\overline{\varepsilon}_i$ and the BBL $\overline{\varepsilon}$ (section 2.5.4), Lappe and Umlauf (2016) defined the

ratio of the energy dissipation in BBL and the interior

$$R_\varepsilon = \frac{A_{BBL}}{A_i}\frac{\overline{\mathcal{E}}}{\overline{\overline{\mathcal{E}_i}}}\,, \tag{3.2}$$

and the rate of irreversible increase of background potential energy due to mixing

$$R_p = \frac{A_{BBL}}{A_i}\frac{\Gamma}{\gamma_i}\frac{\overline{\mathcal{E}}}{\overline{\overline{\mathcal{E}_i}}}\,, \tag{3.3}$$

where γ_i is the flux coefficient of the interior, which is assumed to be constant based on the observations by van der Lee and Umlauf (2011).

Region II, which is located above the halocline, is characterized by high bulk mixing efficiencies, and is therefore the basis for further considerations. The relative area can be estimated by $A_{\mathrm{BBL}}/A_i \approx 1/25$ (Lappe and Umlauf 2016) for the Bornholm Basin using $r = 50\,\mathrm{km}$ and mean properties of region II: $h_{\mathrm{BBL}} = 2.5\,\mathrm{m}$ and $\alpha = 2.5 \times 10^{-3}$. A representative dissipation rate of the interior is obtained from averaging the dissipation rates of station S1 (see Figure 7 of van der Lee and Umlauf 2011) in the density limits (Tab. 3.1). This procedure is more or less a depth average between $40\,\mathrm{m}$ and $50\,\mathrm{m}$. The calculated average of the interior dissipation rate is $\mathcal{E}_i \approx 10^{-9}\mathrm{W\,kg^{-1}}$, which is close to the noise level of the profiler, as the average was performed in the "quiet" region between thermocline and halocline (Fig.2.2). The interior dissipation rate is about $\mathcal{E}_i \approx 8 \times 10^{-9}\,\mathrm{W\,kg^{-1}}$ in the more energetic depth range from $50\,\mathrm{m}$ to $60\,\mathrm{m}$, which includes parts of the halocline. This value is used as an upper limit for interior dissipation. However, the choice of this upper limit is to some extent arbitrary, because the mixing in the BBL region II takes place in a specific density range (Tab. 3.1) that is located above the halocline in the center. Finally, the estimates of the averaged dissipation rates $\mathcal{E}$ are listed in Table 3.2 for three approaches for region II.

The resulting estimate of the energy dissipation ratio is in the range of $R_\varepsilon = 1.4{-}11$, which would further increase if the unresolved near-bottom dissipation was included in the calculation. That means, that the majority of the energy dissipation in the Bornholm Basin takes place in the BBL of the lateral boundary. Certainly, the ratio is moving towards the contribution of interior dissipation if the increased value of the depth range from $50\,\mathrm{m}$ to $60\,\mathrm{m}$ is used. The discussed result enables a statement to the rate of irreversible increase of background potential energy due to mixing, R_p, because it only differs from R_ε in the constant Γ/γ_i (see Tab. 3.2, $\gamma_i \approx 0.2$). As a result,

boundary mixing is dominating this ratio and contributes more to overall mixing than mixing in the ”quiet” interior above the halocline.

3.6. Conclusions

Figure 3.6 summarizes the key mixing processes in the water column of the Bornholm Basin in summer, as an example of a non-tidal basin with a pycnocline. The sketch illustrates the differences between interior mixing (Fig. 3.6a) far away from the lateral boundaries investigated by van der Lee and Umlauf (2011), and mixing along the sloping boundaries (Fig. 3.6b) studied in this chapter (Lappe and Umlauf 2016).

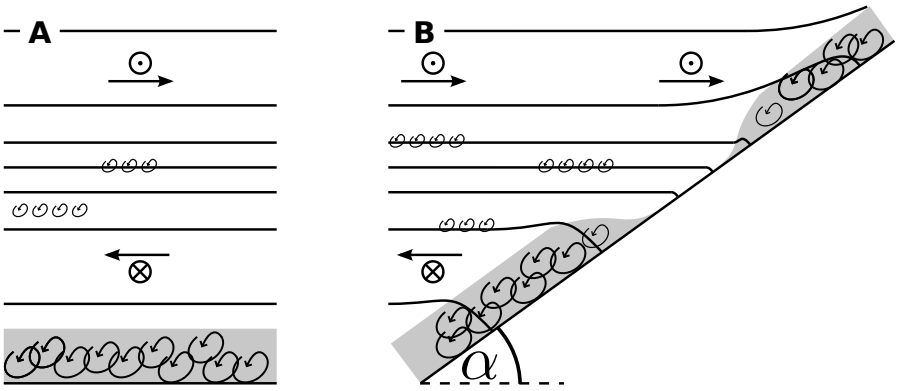

Figure 3.6.: Schematic view of mixing processes in a non-tidal basin with a pycnocline (a) in the interior of the basin, and (b) near the sloping boundary. Isopycnals are shown as black contour lines; the gray-shaded areas mark the turbulent BBL. Arrows schematically indicate the near-inertial velocities above and below the pycnocline. Figure taken from Lappe and Umlauf (2016).

The Bornholm Basin is dominated by near-inertial motions, characterized by opposite velocity directions above and below the halocline indicated by direction markers (Fig. 3.6). As a result, shear layers of several meter thickness are found in the area of the halocline and form one of the preconditions for shear instabilities and mixing. The shear layers coincide with bands of enhanced dissipation rates (van der Lee and Umlauf 2011). Theses mixing bands have a thickness of a few meters and they are temporally stable for several hours (van der Lee and Umlauf 2011). Besides these mixing bands, a pronounced turbulent boundary layer is located above the bottom, characterized by reduced stratification.

Shear bands and coinciding bands of enhanced dissipation rates are also found at some distance to the sloping boundary (Fig. 3.6). The observed motions indicate, again, a dominance of near-inertial wave motions in the velocity field very similar to the center position. The corresponding near-inertial shear bands in the area of the halocline are characterized by a thickness of several meters and are temporally stable for hours (Lappe and Umlauf 2016). The geometry, the vertical and lateral extent of shear layers and bands of enhanced dissipation rates, as well as the striking correlation between both, are similar to those found in the center of the basin (van der Lee and Umlauf 2011). Hence, it can be concluded that the same processes, scalings and parameterizations found by van der Lee and Umlauf (2011) can also be applied for the mixing bands within the halocline at the slope.

Furthermore, the lateral boundary region is characterized by energetic, frictional BBLs of a few meter thickness. The dissipation rates exceed values of $10^{-7}\,\mathrm{W\,kg^{-1}}$ and are $1-2$ orders of magnitude larger than outside the BBL. Parts of the BBL are characterized by a bulk mixing efficiency of order $\Gamma = 0.2$, suggesting that the mixing efficiency at the slope can be comparable to the mixing efficiency of the interior, if the BBL at the slope is permanently restratified. Furthermore, high mixing rates and a high mixing efficiency in the BBL leads to a dominance of the BBL mixing contribution to the basin-scale mixing rate above the halocline. This behavior contradicts the classical view of boundary layers, where mixing efficiencies are small, as the BBL is assumed to be already well-mixed.

Besides the turbulent BBL above and below the halocline, turbulence is suppressed where the halocline intersects the slope. As a consequence, neither mixing in the interior nor at the boundary is strong enough to support a significant cross-halocline transport of dissolved substances, e.g., salt and nutrients, in summer. This blocking of the cross-halocline transport has implications for the ecosystem. The BBL collapse in the halocline region is the result of (a) the suppression of turbulence by increased stratification and (b) the presence of near-inertial wave modes inflection points in this area (see, e.g., van der Lee and Umlauf 2011). The impact of near-inertial wave mode inflection points and the related reduction of near-inertial velocities and the presence of near-inertial shear within the halocline is different in the interior than at the lateral boundary. In the interior, the near-inertial shear is the reason for shear-instabilities and mixing, while reduced velocities in the near-bottom region lead to lower bottom-related shear and turbulence in comparison to the bottom regions below and above the halocline.

The results of this investigation might be relevant for other non-tidal basins with a strong pycnocline. Furthermore, the detailed investigation of the BBL indicate that vertically high resolved measurements are needed to investigate processes at the sloping boundary. To model these processes and resolve the vertical structure of the BBL numerically, extremely fine vertical grids are needed in the near-bottom region.

Chapter 4.

Boundary mixing under winter conditions

4.1. Introduction

Turbulent diapycnal mixing is an important mechanism to close the overturning circulation in the ocean (Wunsch and Ferrari 2004) as well as in marginal seas like the Baltic Sea (Reissmann et al. 2009). Mixing is generated by several processes that concern the surface layer (e.g. Moum and Smyth 2001), the interior of stratified basins (e.g. the thermocline, Gregg 1989), and the boundaries (e.g. Moum et al. 2002). Waterhouse et al. (2014) estimated that $31\,\%$ of the total energy input is dissipated at continental slopes and canyons. There are several processes that generate turbulence and mixing at lateral boundaries like the shelf regions in the ocean or sloping areas in lakes and marginal seas. These include breaking of internal waves (Lamb 2014) and internal tides (Martini et al. 2013) as well as the interaction of mesoscale eddies with boundaries (Brearley et al. 2013). Further, internal seiches, tides, or near-inertial waves can lead to alternating patterns of upslope and downslope flow that, in combination with bottom shear, are a source of persistent turbulence and mixing. During the upslope flow phase, turbulence generated by bottom friction is additionally fueled by differential advection. The upslope movement of isopycnals is delayed by frictional shear close to the bottom and, as a consequence, denser water is pushed above lighter water, resulting in convective turbulence (Lorke et al. 2005). In contrast, stratification increases during the downslope movement of isopycnals during the down slope phase. The implications of these alternating patterns of stabilization and destabilization of the BBL on the overall efficiency of mixing have been investigated in detail by Umlauf

and Burchard (2011) and Becherer and Umlauf (2011). Beyond these local effects, the presence of boundaries can also increase mixing in the surroundings, because internal waves generated by e.g. the interaction of internal tides with topography (Ledwell et al. 2000) may travel upwards and break in shear layers above the boundary.

Tides are the main energy source of boundary mixing at many locations in oceans and marginal seas. However, the non-tidal Baltic Sea is ideally suited for the investigation of processes that are usually obscured by the presence of tides. Furthermore, Holtermann et al. (2014) showed that boundary mixing is a dominant process in the Baltic Sea. The vertical spreading of an artificial tracer increased dramatically in the deep layers of the Gotland Basin as soon as the tracer reached the lateral boundaries. Direct turbulence measurements were performed by Lappe and Umlauf (2016) at a lateral boundary in the Bornholm Basin that is dominated by near-inertial wave motions (van der Lee and Umlauf 2011). Lappe and Umlauf (2016) found a persistent restratifying region in the turbulent bottom boundary layer (BBL) where mixing was efficient and exceed the contribution of interior mixing in the same density range. Their study was carried out during summer conditions, when a seasonal thermocline protects the permanent halocline from surface turbulence and velocities are dominated by vertical mode-2 near-inertial motions. The evolution of a turbulent BBL was found to be suppressed where the halocline intersects with the sloping topography and thus a significant contribution of boundary mixing to the overall transport through the halocline is unlikely. The halocline and the stratified interior are characterized by smaller turbulence levels, except for some layers of enhanced dissipation rates which correlate with near-inertial shear layers. These layers dominate mixing in the halocline (van der Lee and Umlauf 2011). Mixing was found to be more energetic in winter, but averaged buoyancy fluxes in the halocline were still small in both cases.

Here, data are presented from an extensive field campaign at the lateral boundary of the Bornholm Basin in winter. In contrast to the summer observations of Lappe and Umlauf (2016, chapter 3), the study site was characterized by typical winter stratification where the protecting effect of the thermocline is missing. The data include high resolution turbulence microstructure observations as well as time series of salinity and temperature at high vertical resolution. This investigation concentrates on the processes in the halocline and the interaction of the halocline with the slope.

4.2. Temporal variability

Winds increased from $6\,\mathrm{m\,s^{-1}}$ to $11\,\mathrm{m\,s^{-1}}$ and prevented measurements along transect T1 (Fig. 2.1), where the ship could not be aligned with the wind direction, after yearday 63.85. However, conditions still permitted measurements at station T1A (see above). There, 9 short transects (Fig. 4.1), described in more detail in section 2.2, were performed in the immediate vicinity of the station. Figures 4.1 and 4.2a shows wind speed and direction during these measurements. It illustrates that this period was characterized by a strong wind event lasting until approximately day 64.5. Time series of temperature and salinity (Fig. 4.2b,c) show a warm and saline near-bottom pool that is separated from a cold and brackish layer on top by a halocline at a depth of $60\,\mathrm{m}$. This halocline is collocated with an inverse thermocline across which temperatures increase by up to $6\,^{\circ}\mathrm{C}$. Density ratios (like in Fig. 4.12e) suggest that double-diffusive convection may occur, but is not a first order process (see below).

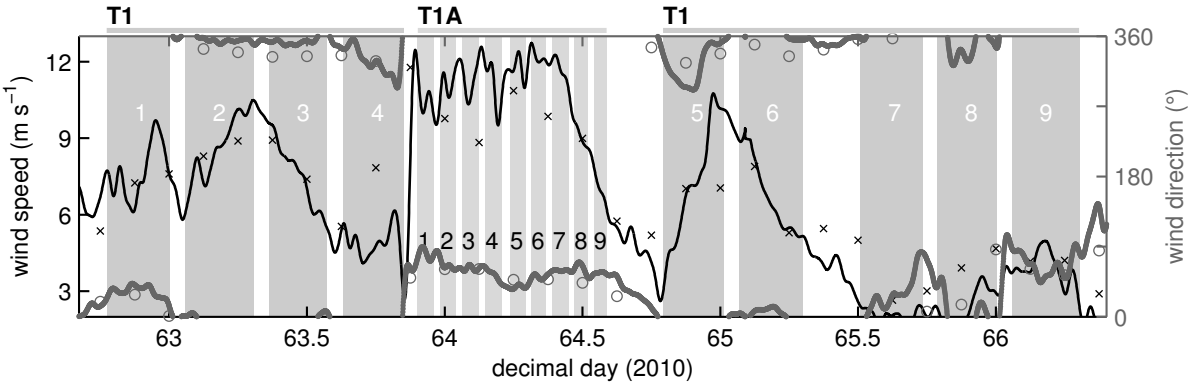

Figure 4.1.: Time series of wind speed (black) and wind direction (gray). Short-term wind predictions (markers) are complemented by on-board weather station data (lines). Gray lines on top denote the periods of ship-based measurements along transect T1 and near station T1A (Fig. 2.1). Gray-shaded areas show the times of the nine individual ship surveys along T1 and near T1A, respectively.

The buoyancy frequency squared (Figs. 4.3a, 2.2c) indicates that the water column is structured into a nearly well-mixed surface layer, a strongly stratified intermediate region that includes the halocline and a weakly stratified BBL of approximately $4\,\mathrm{m}$ thickness that is topped by a secondary pycnocline. At the beginning of the measurements, the surface layer can be further subdivided into a near-surface region of $20\,\mathrm{m}$ thickness (Fig. 4.3b), characterized by strong dissipation, and a calm layer below. Surprisingly, despite the large dissipation rates, this turbulent surface layer shows weak but persistent stratification. It is likely that restratification due to lateral density

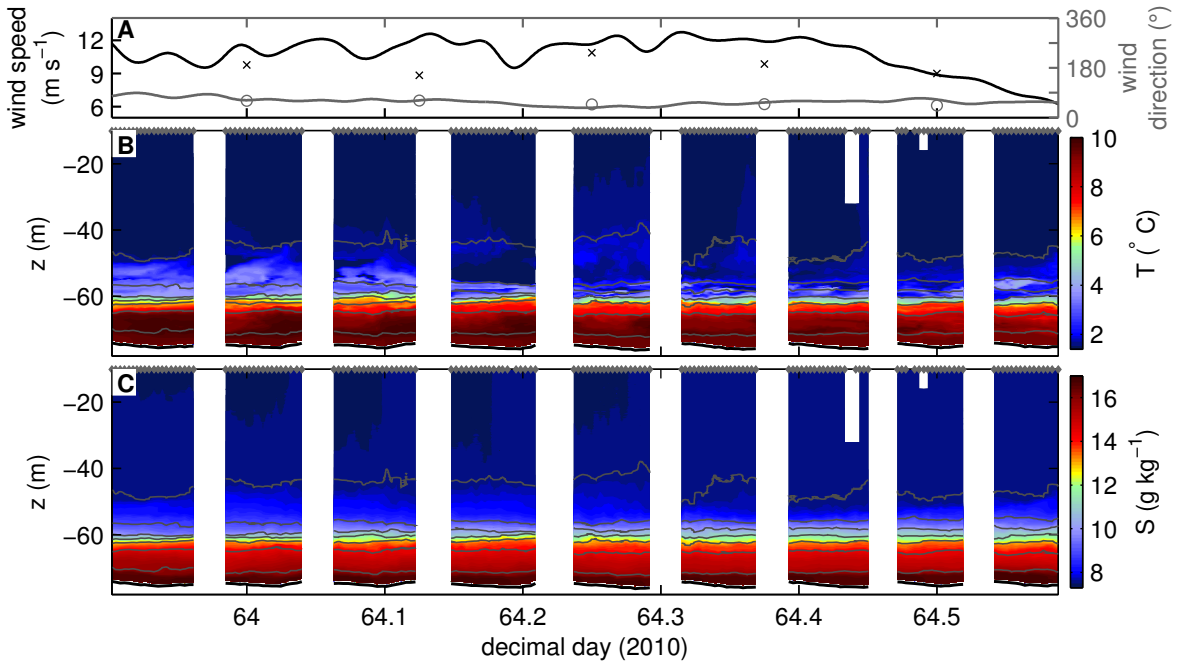

Figure 4.2.: Time series of (a) wind speed (black), wind direction (gray), (b) temperature and (c) absolute salinity at station T1A. Short-term wind predictions (markers) are complemented by on-board weather station data (lines) in (a). Gray contour lines denote isopycnals at $1\,\mathrm{kg\,m^{-3}}$ intervals, starting with $\sigma_\theta = 6\,\mathrm{kg\,m^{-3}}$ at the top in (b) and (c). The black thick line displays the bottom. Gray diamonds at the top of the panels indicate individual microstructure casts.

gradients plays a major role in this process, as suggested by the horizontal density gradients visible in the cross-slope transects discussed in more detail below (Fig. 4.6b). Interactions with mesoscale or sub-mesoscale eddies are also a possible explanation, but our single-point data are not sufficient to draw any definite conclusions regarding these issues. Persistent winds lead to a downward penetration of the turbulent surface layer, and a gradual destruction of near-surface stratification (Fig. 4.3a,b). The downward propagation of the mixing layer is stopped by a weakly stratified region at a depth of $40\,\mathrm{m}$ on yearday 64.05. This layer, which might also be formed by lateral restratification, reduces from a thickness of $15\,\mathrm{m}$ in the beginning to $5\,\mathrm{m}$ after yearday 64.3, pointing at entrainment and sharpening of the upper part of the halocline during the wind event. Additionally, laterally advected and interleaving waters determine the temperature structures in this layer (Fig. 4.2b). The cold water patches, which interleave in the short transects 2, 3 and 4 at a depth of $50\,\mathrm{m}$, show temperatures that are even colder than the surface water.

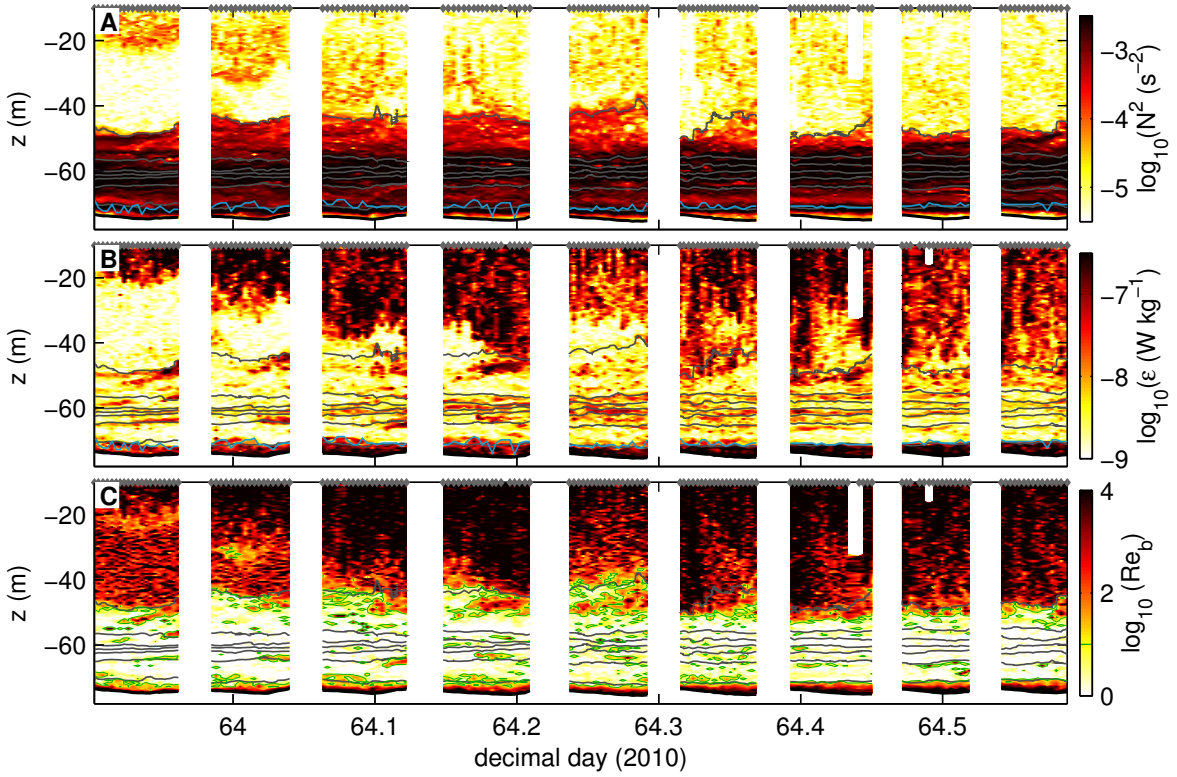

Figure 4.3.: Time series of (a) buoyancy frequency squared, (b) dissipation rate and (c) buoyancy Reynolds number at station T1A. The height of the BBL is indicated by the light blue line in (a) and (b). Green contour line denotes $Re_b = 10$ in (c). Further information is given in Fig. 4.2.

The halocline is located at a depth of approximately $60\,\mathrm{m}$ as evident from the broad maximum in the buoyancy frequency squared (Fig. 4.3a). The associated pycnocline is significantly weakened during the measurements, as most easily visible from the increasing distances between neighboring isopycnals. This isopycnal spreading occurs throughout the entire measuring period including the T1A and T1C measurements as well as microstructure profiler measurements along transect T1 (discussed in detail below). Bands and patches with enhanced dissipation rates (Fig. 4.3b) are seen to persist across multiple short ship transects at comparable depth ranges in the halocline, which is consistent with the findings of van der Lee and Umlauf (2011). These authors showed that these mixing bands correlate with near-inertial shear bands that may persist over time scales of the order of the inertial period. I do not have velocity data to conclusively show that the same mechanisms also determine mixing in our data set. However, halocline dissipation rates are strongly enhanced during the wind event, although with a temporal delay, which is consistent with boundary-generated

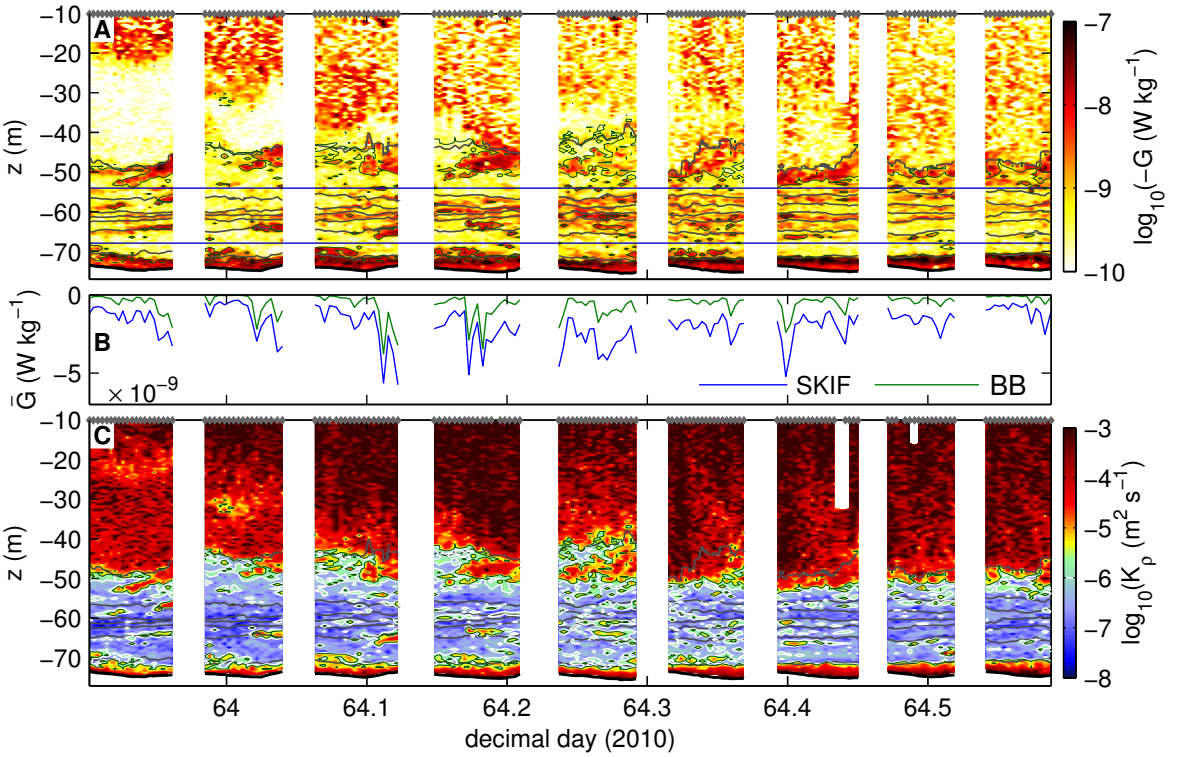

Figure 4.4.: Time series of (a) buoyancy flux, (b) vertical averaged buoyancy flux and (c) turbulent diffusivity at station T1A. The green contour line denotes $Re_b = 10$ in (a),(c). Further blue horizontal lines (in (a)) indicate the upper and lower integration limits for the calculation in (b). A white contour line is added to mark $K_\rho = 1 \times 10^{-6}\,\mathrm{m^2\,s^{-1}}$ in (c). Additional information are given in Fig. 4.2.

near-inertial waves slowly propagating towards the interior, as suggested by van der Lee and Umlauf (2011).

The buoyancy flux G and the turbulent diffusivity K_ρ are the relevant quantities to define mixing:

$$G = -\gamma\varepsilon \quad , \tag{4.1}$$

$$K_\rho = -\frac{G}{N^2} \quad . \tag{4.2}$$

The crucial parameter in the latter equations is the flux coefficient γ, which is determined here from the SKIF parametrization (Tab. 2.3 and section 2.5.2). This parametrization is based on the buoyancy Reynolds number $Re_b = \epsilon/(\nu N^2)$ and has been validated (e.g. Walter et al. 2014) for the "energetic regime" with $Re_b > 100$, in which the flux coefficient γ decreases according to a power-law relationship for increasing Re_b. This parameterization was also used in the previous chapter 3, and in similar

investigations (e.g. van der Lee and Umlauf 2011; Cyr et al. 2015). Note that the SKIF parameterization ignores the suppression of small-scale overturns by viscous and buoyancy effects for small values of Re_b, resulting in a reduction of the flux coefficient for small Re_b in particular for salinity-stratified flows, as pointed out by Bouffard and Boegman (2013) (further information is given in section 2.5.2). The time series of the buoyancy Reynolds number (Fig. 4.3c) illustrates that the stratified interior is characterized by small values, thus pointing at a potential overestimation of mixing parameters by the SKIF parametrization, except for some intermittent patches of increased buoyancy Reynolds numbers (the $Re_b = 10$ isoline is shown in Figure 4.3c and in the time series of the mixing quantities in Figs. 4.4a,c). For buoyancy Reynolds numbers smaller than $Re_b \sim 10$, the vertical turbulent fluxes are generally assumed to collapse (e.g. Shih et al. 2005; Ivey and Imberger 1991). In contrast, the surface and bottom layers show enhanced buoyancy Reynolds numbers as a consequence of weaker stratification and stronger turbulence.

Buoyancy fluxes (Fig. 4.4a) are enhanced in the surface layer because of the combined effect of strong turbulence and significant vertical stratification that may have resulted from lateral restratification as discussed above. Buoyancy fluxes are also enhanced above the bottom in the upper part of the BBL, which remains stratified. In this region, the buoyancy flux parametrization should be still appropriate because the Ozmidov scale L_O defined in (1.38) is the dominating turbulence length scale (rather than the distance to the bottom). The BBL is described in more detail below. Buoyancy fluxes are reduced in the stratified interior where dissipation rates and buoyancy Reynolds numbers are small and thus $\gamma = 0.2$ from the SKIF parametrization (Fig. 2.3). Thus, the buoyancy fluxes (Fig. 4.4a) reproduce the structures of the dissipation rates shown in Fig. 4.3b in the halocline region between approximately $50\,\mathrm{m}$ and $70\,\mathrm{m}$, including the characteristic intermittent patches of enhanced values that coincide partly with patches of increased buoyancy Reynolds numbers. This suggests that a large portion of the vertical buoyancy flux is supported by these energetic regions. In the same manner, the vertical averaged buoyancy flux $\bar{G} = (\int_a^b G(z)\,\mathrm{d}z)/h_i$ (Fig. 4.4b), where h_i is the vertical thickness of the mixing region as indicated in Fig. 4.4a by the integration limits a and b (blue lines), is dominated by these energetic regions, and $\bar{G}$ increases significantly if an energetic intermittent patch occurs. The fact that the main transport through the halocline occurs in energetic intermittent patches (Fig. 4.4a,b) is independent of the selected γ-parametrization (Table 2.3). However, the reduction of γ for small values of Re_b suggested by BB is mirrored in a strong reduction of the averaged buoyancy flux.

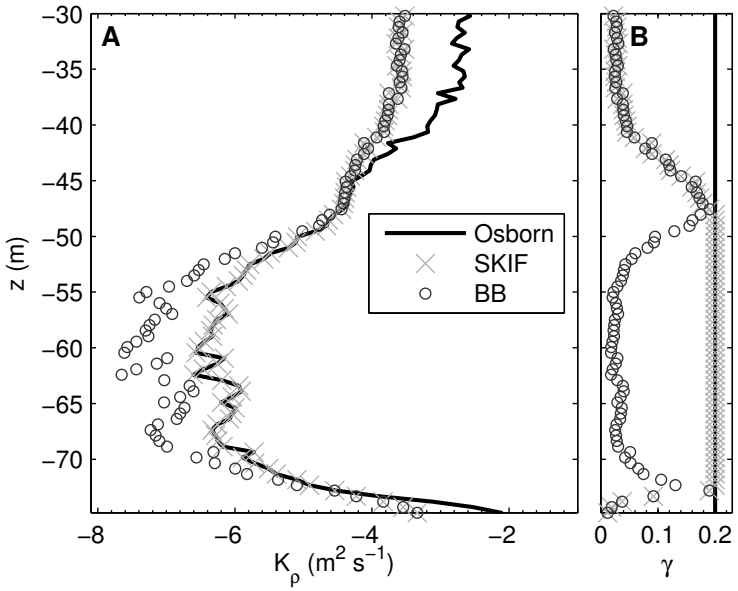

Figure 4.5.: Vertical profiles of time averaged (a) turbulent diffusivities and (b) flux coefficients for different parameterizations listed in Table 2.3.

Similar to the buoyancy flux, the turbulent diffusivity is also strongly reduced in the stratified interior (Fig. 4.4c) in comparison to the surface and bottom layers. However, values exceed the threshold of $10^{-6}\,\mathrm{m^2\,s^{-1}}$ in some energetic intermittent patches by an order of magnitude in the halocline. Following van der Lee and Umlauf (2011), a time averaged diffusivity profile, $K_\rho = -\gamma\langle\varepsilon\rangle/\langle N^2\rangle$, is determined, where the averaging operator $\langle\cdot\rangle$ here denotes the time average over all T1A profiles (Fig. 4.3a,b). The resulting diffusivity profiles for the SKIF, BB and Osborn γ-parameterizations (Tab. 2.3) are shown in Figure 4.5a. Diffusivities are enhanced in the surface layer, where the SKIF and BB profiles are an order of magnitude smaller than the Osborn profile as a result of the enhanced buoyancy Reynolds numbers (Fig. 4.3c) and the corresponding reduction in the flux coefficient (Fig. 4.5b). At the bottom of the surface layer, a thin transition region exists in the depth range from $45\,\mathrm{m}$ to $50\,\mathrm{m}$, where the three parameterizations show similar results. Within this depth range weak stratification sets in (Fig. 2.2), while the averaged ε profile starts to decrease. The transition from the energetic regime ($Re_b > 100$) to strongly buoyancy controlled regime ($Re_b < 10$) takes place immediately. The time-averaged diffusivities rarely exceed the threshold of $1 \times 10^{-6}\,\mathrm{m^2\,s^{-1}}$ in the halocline region between $55\,\mathrm{m}$ and $70\,\mathrm{m}$ for the SKIF and Osborn parameterizations, respectively. The averaged value is similar to the diffusivities of the halocline in the center of the basin (van der Lee and Umlauf 2011). Considering the potential effect of decreasing flux coefficients in the buoyancy-controlled regime

as suggested by BB results in approximately one order of-magnitude smaller flux coefficients and diffusivities in the halocline region (Fig. 4.5). This demonstrates again that the γ-parametrization is the bottle neck of the consideration of the effect of small buoyancy Reynolds numbers. Because an independent validation of the model assumptions adopted by BB is so far lacking, it remains unclear if restratification effects in salinity-stratified turbulence at low energy levels are really as strong as suggested by this model. This does, however, not affect the overall conclusion that turbulent transport across the halocline is very small.

Van der Lee and Umlauf (2011) found a weakly stratified and highly energetic BBL near the deepest point in the Bornholm Basin. It was characterized by an modulation near the inertial frequency as a result of the superposition of near-inertial waves and a background current. The T1A station is located at the lateral boundary, but still on the lower end of the transect T1. The observed BBL (Fig. 4.3) seems to be similar to the one found by van der Lee and Umlauf (2011), even so the restratification effects are likely to be larger and the time series is too short to conclusively demonstrate the mentioned oscillation.

The BBL (Fig. 4.3) is defined here as the contiguous near-bottom region of enhanced dissipation rates ($\varepsilon > 8 \times 10^{-9}\,\mathrm{W\,kg^{-1}}$) analogously to the BBL definition in section 3.3.1. The characterization of mixing inside the BBL follows the description in section 2.5.4. Similarly to Table 3.2, estimates of the averaged mixing rate $N_\infty^2 \overline{\mathcal{E}}_p$, the averaged dissipation rate $\overline{\mathcal{E}}$ and the bulk mixing efficiency Γ are derived for station T1A (Tab. 4.1). Particular attention is paid to the region close to the bottom in which the turbulence length scale is determined by the wall-layer scaling $l = \kappa\zeta$ rather than by the Ozmidov scale L_O. A general validity of the SKIF-parameterization (Table 2.3) therefore cannot be guaranteed in this region. As no generally valid expression for the computation of the mixing rate is available for this region, we investigate in the following three special cases: (a) the near-bottom region with $l < L_O$ is treated like any other region (marked as "included" in Tab. 4.1), (b) the local mixing rates are assumed to vanish ("zero mixing") where $l < Lo$, and (c) the near-bottom region is completely ignored ("excluded"). The potential density varies between $\sigma_\theta = 11.62\,\mathrm{kg\,m^{-3}}$ and $\sigma_\theta = 12.84\,\mathrm{kg\,m^{-3}}$ in the BBL and, accordingly, the stratification of the interior N_∞^2 is estimated by $1.1 \times 10^{-3}\,\mathrm{s^{-2}}$ based on the winter data of the center measurements (van der Lee and Umlauf 2011) at location $S1$ (Fig. 2.1). Against expectations, the mixing rate and the bulk mixing efficiency of station T1A are much bigger than in region IV, which describes the below halocline BBL in summer (see Tab. 3.2 above).

Table 4.1.: Average dissipation and mixing rates defined in (2.11) and bulk mixing efficiency. Near-bottom data with $L_O > \kappa\zeta$ are either excluded (first row), included (second row) or assumed to provide no contribution to mixing ($\chi_b = 0$, third row). Mixing efficiencies are computed based on N^2_∞ given in the text.

near-bottom data	$\overline{\mathcal{E}}$ (10^{-7} W kg^{-1})	$N^2_\infty \overline{\mathcal{E}}_p$ (10^{-11} W kg^{-1} s^{-2})	$\Gamma = \overline{\mathcal{E}}_p / \overline{\mathcal{E}}$
excluded	1.95	12.87	0.61
included	3.77	9.00	0.22
zero mixing	3.77	8.98	0.22

The difference is a result of the more efficient restratification in the BBL and a corresponding coincidence of stratification and enhanced dissipation rates in the upper half of the BBL during winter. This situation and the magnitude of the parameters of the actual BBL is more similar to region II (Tab. 3.2) of the summer data, which was located between halocline and thermocline.

Interpreting the results in Tab. 4.1, it should be noted that our turbulence microstructure data do not include a thin region located directly adjacent to the bottom as a result of the sensor protection cage and the tricky precise detection of the sediment-water interface in the case of muddy sediments (see also appendix A.3). The unresolved region has a thickness of approximately $10\,\mathrm{cm}$ and is, provided that the profiler does not sink into the sediments, given by the distance between sensor protection cage and sensor tip. The region above the bottom is generally characterized by strong dissipation of TKE and vanishing mixing efficiencies according to the law of the wall. Ignoring the lowest centimeters has a strong impact on the bulk parameters in Tab. 4.1 as evident from the direct comparison of the "included" and "excluded" cases. With the help of the law of the wall (1.36), the lost dissipation rate can be estimated, as described at the end of section 3.4. As a result the mixing efficiency Γ would decrease to 0.15 which is still close to the mixing efficiency $\Gamma = 0.2$ of interior mixing. The overall conclusion from this is that also under winter conditions boundary mixing may be as efficient as interior mixing.

4.3. Spatial variability

Altogether 9 cross-slope (cross-isobath) surveys along transect T1 (Figs. 2.1 and 4.1) were performed during weaker wind conditions before and after the measurements at station T1A discussed in section 4.2. Every survey had a duration of $5\,\mathrm{h}$ to $6\,\mathrm{h}$, which is a significant fraction of the inertial period of $T_f = 14.56\,\mathrm{h}$. Figure 4.6a,b offers some insight into the temperature and salinity structure during survey 2, which represents the conditions before the wind event. A brackish, cold, and $40\,\mathrm{m}$ to $60\,\mathrm{m}$ deep surface layer is located above a warmer and more saline bottom water pool separated by a halocline. This halocline (see also Fig. 4.6c or 4.7c) is approximately $15\,\mathrm{m}$ broad at the deep side of the transect and becomes narrower until it intersects as a sharp density interface with the slope at $s \approx 12\,\mathrm{km}$. This structure of the halocline does not change strongly during the measurements, although the sharp halocline starts to weaken slightly during the interruption of the measurements (between surveys 4 and 5, Fig. 4.1) during the strong wind event described above. The density structure and the velocity measurements (Fig. 4.7a,b) are consistent with the presence of an anti-cyclonic mesoscale eddy, whose signature was strongest in the first surveys.

4.3.1. Mixing in the halocline

Enhanced dissipation rates can be found in the turbulent boundary layers and in band-like structures in the stratified interior (Figs. 4.6d, 4.7d). The halocline dissipation bands are similar to those mentioned above in the time series of section 4.2 (Fig. 4.3) or in the transect data of chapter 3, e.g. Figure 3.3d. Obviously, the overall turbulence levels in the winter halocline are intensified in comparison to the summer data of chapter 3. This difference was also noticed by van der Lee and Umlauf (2011) for the central station S1 (Fig. 2.1). The most characteristic feature, however, is the persistent and up to $7\,\mathrm{km}$ long band of strongly enhanced dissipation rates within the sharp halocline evolving on the shallow side of the transect (Figs. 4.6d and 4.7d) during the first four surveys. In view of the extremely strong stratification in this region ($N^2 \approx 0.07\,\mathrm{s}^{-2}$), this is remarkable, and points at strong vertical shear. This is partly supported by the velocity measurements in Fig. 4.7a,b but the TLADCP data turned out to be too noisy to reliably resolve the shear at such small scales (the thickness of the halocline in this region is comparable to the bin size). The processes inside the pronounced halocline mixing region are explained in more detail below.

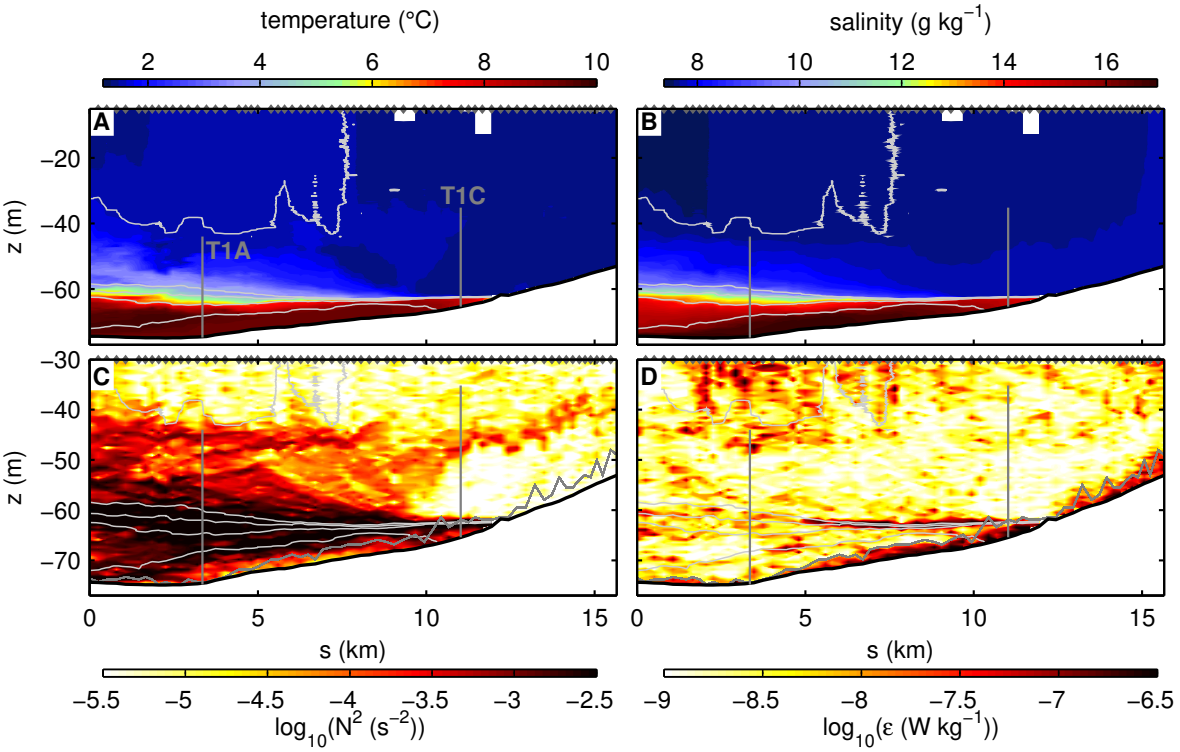

Figure 4.6.: Cross-slope transect of (a) temperature, (b) salinity, (c) buoyancy frequency squared and (d) dissipation rate. These data were collected along transect T1 during survey 2. The bottom is indicated by a thick black line. Light gray contour lines denote isopycnals at $1.5\,\mathrm{kg\,m^{-3}}$ intervals, starting with $\sigma_\theta = 6\,\mathrm{kg\,m^{-3}}$ at the top. Note that (a) and (b) have different depth ranges. The thickness of the BBL is given by a gray line in (c) and (d). Gray markers at the top of the panels indicate individual microstructure casts. Vertical gray lines illustrate the extent and the location of the CTD chain at station T1A and the temperature chain at T1C (Fig. 2.1).

Figure 4.9a shows the vertical buoyancy fluxes of survey 3 (see the other quantities in Fig. 4.7), calculated from equation (2.3) using the SKIF γ-parametrization (Table 2.3). Buoyancy Reynolds numbers (not shown) are small (~ 1) in both the stratified interior and in the sharp halocline, therefore indicating a potential overestimation of the buoyancy fluxes in salinity-stratified flows as suggested by Bouffard and Boegman (2013) and already explained in section 4.2. Nevertheless, intensified buoyancy fluxes (Fig. 4.9a) exist in the BBL and halocline regions. Especially strong mixing can also be found inside the sharp halocline on the shallow side of the transect as a consequence of the locally enhanced dissipation rates (Fig. 4.7d). As the sharp halocline covers only a part of the transect, the latter is split into an interior part at the deep end of the transect, where the halocline is broad, and an interface part characterized by a sharp density interface. The border is placed where the vertical average of

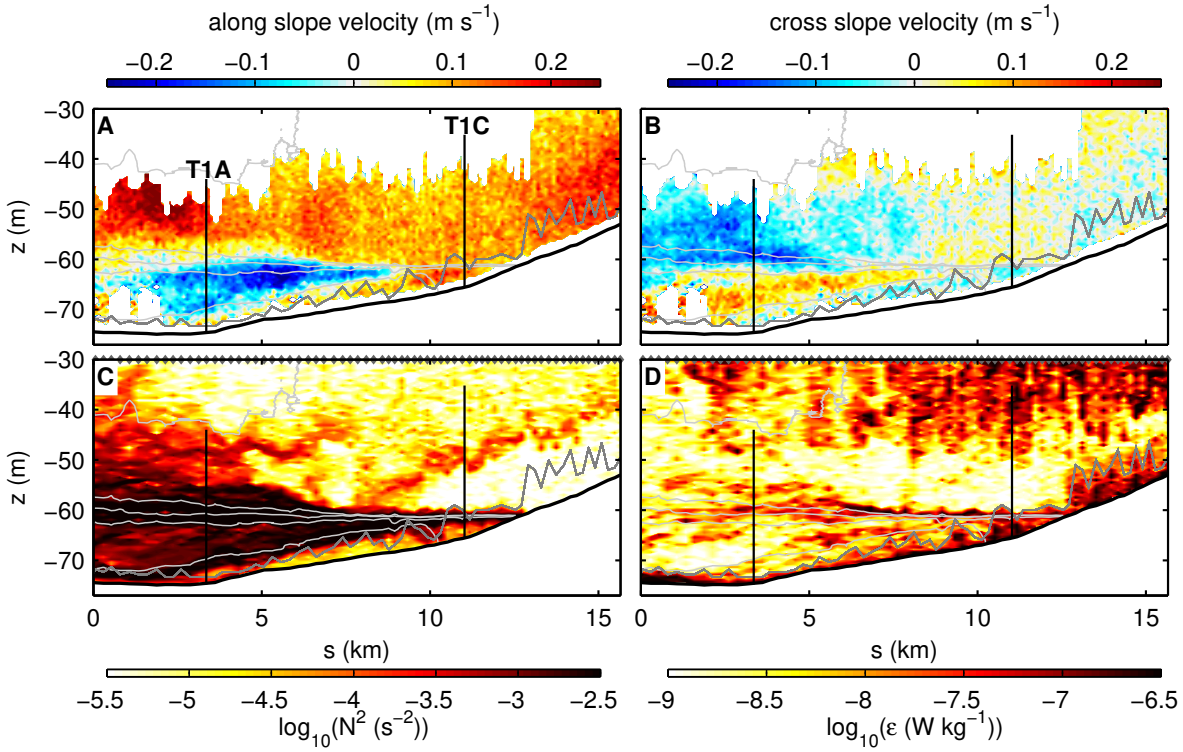

Figure 4.7.: Cross-slope transect of (a) along-slope velocity, (b) cross-slope velocity, (c) buoyancy frequency squared and (d) dissipation rate for survey 3. Further explanations to markers and lines are given in Figure 4.6.

the buoyancy frequency squared within the density range $\sigma_\theta = 7 - 11.3\,\mathrm{kg\,m^{-3}}$ exceeds the value of $N^2 = 6.3 \times 10^{-3}\,\mathrm{s^{-2}}$ for the first time, starting at $s = 0$ (as a reminder, s is the along-transect coordinate, Fig. 2.1). Both regions are separated by a dashed vertical line in Figures 4.9a–d. Figure 4.9c,d shows the vertically averaged buoyancy flux $\bar{G}$ for the region indicated by blue lines in Figure 4.9a,b. The lower limit corresponds to the $\sigma_\theta = 11.3\,\mathrm{kg\,m^{-3}}$ isopycnal, whereas the upper limit is located $2\,\mathrm{m}$ above the isoline $\sigma_\theta = 7\,\mathrm{kg\,m^{-3}}$ (the $2\,\mathrm{m}$ offset is required because stratification breaks down directly above the sharp interface, precluding any isopycnal definition of the upper integration limit). The averaged buoyancy fluxes (Figs. 4.9c,d) in the interface region exceed the fluxes in the interior region by up to two orders in magnitude. Note that the interface intersects with the lateral boundary, and therefore a clear separation of boundary and interfacial mixing is not always possible in the near-bottom region.

The cross-slope averaged buoyancy fluxes $\hat{G} = (\int_{s_1}^{s_2} \bar{G}(s)\,\mathrm{d}s)/(s_2 - s_1)$ are calculated for the interior and interface regions for surveys 1 – 4 (Tab. 4.2), and are also shown in Figure 4.9c,d. The averaged buoyancy fluxes in Table 4.2 summarize the features

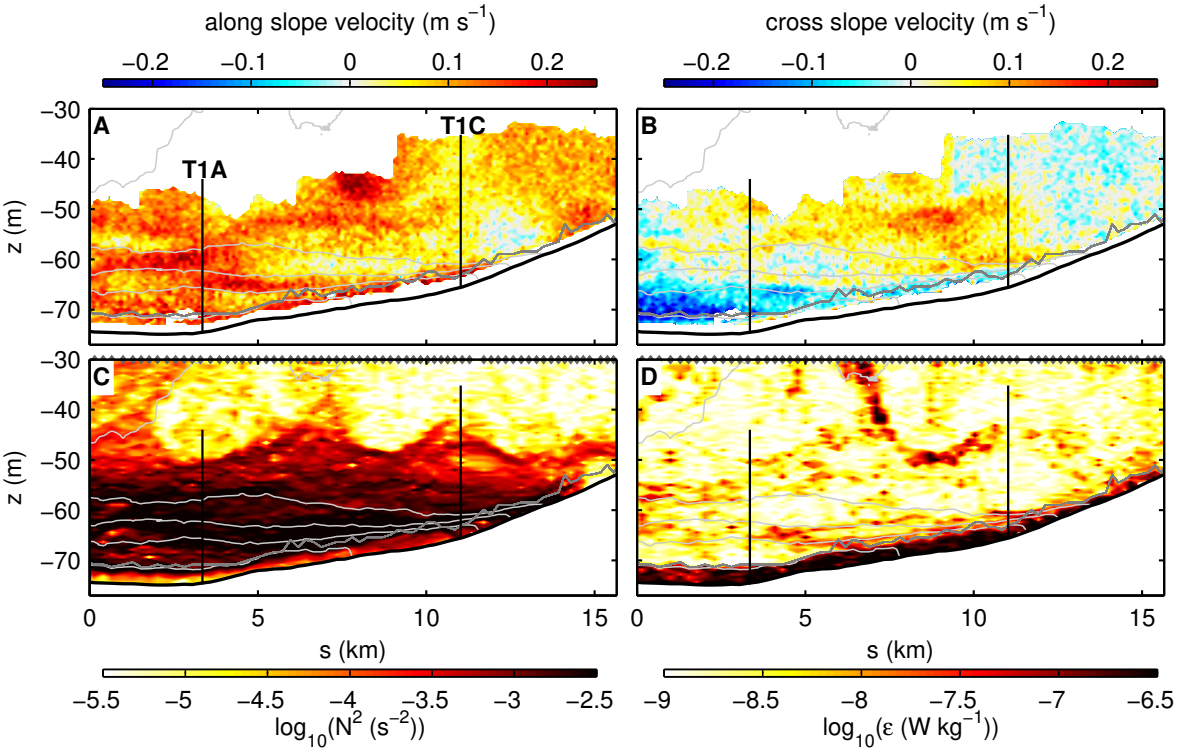

Figure 4.8.: Cross-slope transect of (a) along-slope velocity, (b) cross-slope velocity, (c) buoyancy frequency squared and (d) dissipation rate for survey 7. Further explanations are given in Figs 4.6.

Table 4.2.: Averaged buoyancy fluxes $\hat{G}$ for the cross-slope segments introduced in Fig. 4.9. The calculation based on the γ-parametrization of SKIF (Tab. 2.3) or of BB (in parenthesis).

survey	$\hat{G}$ (10^{-9} W kg^{-1})	
	interior	interface
1	3.3 (1.1)	14.9 (6.8)
2	1.8 (0.5)	25.1 (11.3)
3	3.2 (1.1)	12.9 (5.8)
4	1.6 (0.6)	8.1 (3.5)

already mentioned. The buoyancy fluxes are strongly increased in the interface region in comparison to the interior as a result of the pronounced turbulent band inside the sharp halocline. It may be speculated that the formation of this extremely thin density interface that seems to be highly amenable to instability and mixing is connected to the mesoscale eddy, which might have drained fluid from the interior of the halocline. The situation changes after the storm event when the extremely sharp density

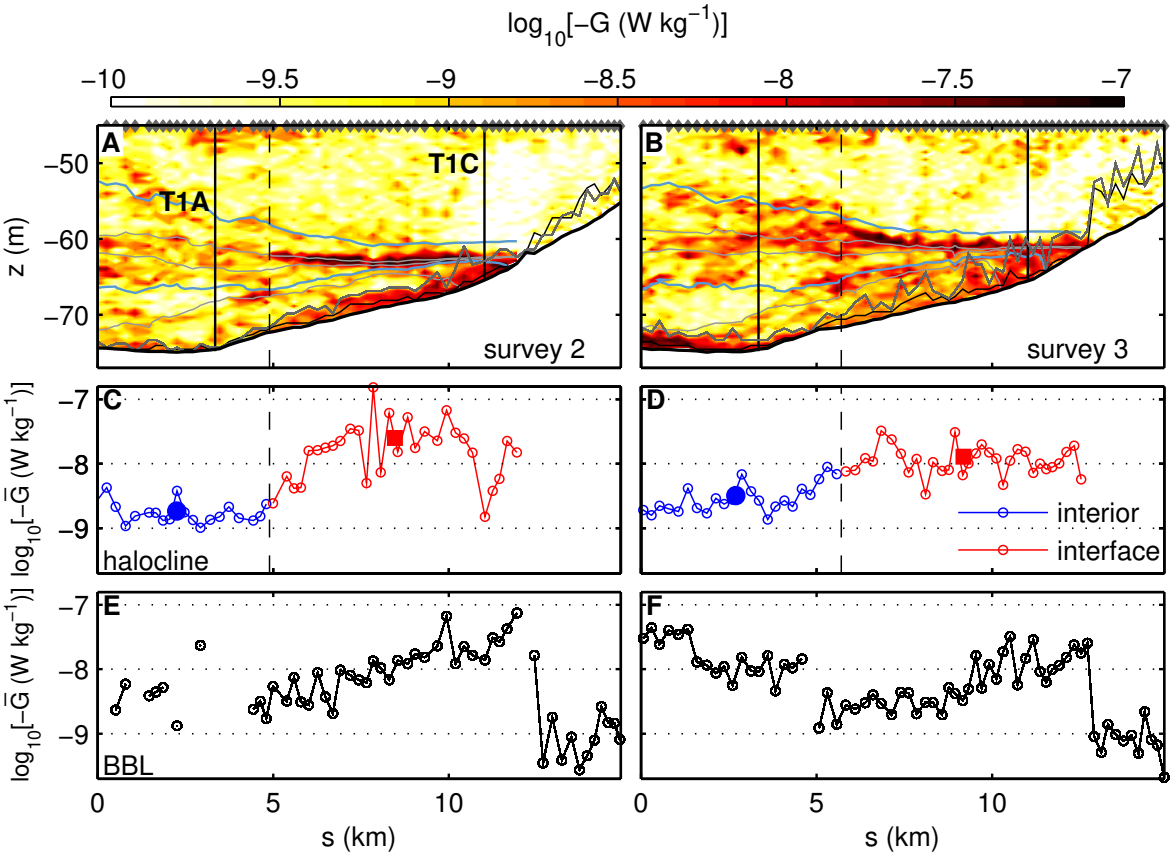

Figure 4.9.: Cross-slope transects of (a,b) buoyancy flux, the vertical averaged buoyancy flux of the halocline in (c,d) and the BBL in (e,f) for surveys 2 (lhs, left hand side) and 3 (rhs). For (a,b): Light gray lines denote isopycnals at 2 kg m^{-3} intervals, starting with $\sigma_\theta = 8$ kg m^{-3} at the top. Blue lines (2 m above the $\sigma_\theta = 7$ kg m^{-3}, and the isoline $\sigma_\theta = 11.3$ kg m^{-3}) indicate the upper and lower limit for the vertical average in (c,d). The thickness of the BBL, which is the upper limit of the vertical average in (e) and (f), and the layer that is controlled by the length scale l are denoted by a dark gray and a thin black line, respectively. Gray markers at the top of panels (a) and (b) indicate individual microstructure casts. For (c,d): The black dashed lines denote the border between the broad interior halocline and the sharper halocline close to the boundary. The large filled markers indicate the cross-slope averaged buoyancy flux $\hat{G}$ for the given graphs. $\hat{G}$'s are listed in Table 4.2 for surveys 1 – 4.

interface on the shallow side of the transect has disappeared, even though some less pronounced bands of enhanced dissipation rates in the halocline can still be identified (e.g. Fig. 4.8c,d). However, a strongly turbulent near-bottom region can still be identified throughout the transect, as discussed in more detail in the following.

As mentioned above, buoyancy fluxes are likely overestimated in the halocline based on the SKIF γ-parametrization due to restratification effects in low-Re_b salinity-

stratified flows (see section 2.5.2). Therefore, the averaged buoyancy fluxes are also listed for the BB γ-parametrization (Tab. 2.3) in Table 4.2, which takes these effects into account. As a consequence, the magnitude of the averaged fluxes decrease, but the relative magnitude of mixing between the two regions remains similar.

4.3.2. Mixing in the bottom boundary layer

A turbulent BBL, indicated by a gray line in the figures, can be identified along the whole transect in every survey (Figs. 4.6, 4.7, 4.8). In contrast to the BBL observed during summer conditions (e.g. Fig. 3.3), in winter the BBL does not collapse in the halocline region, and therefore provides a potential mechanism for vertical mixing through this pycnocline. To study the variability of the BBL, the ship surveys were grouped into those before (1 – 4) and after the wind event (surveys 5 – 9).

The investigation starts with the situation before the wind event. Besides enhanced buoyancy fluxes through the thin halocline in the interior, discussed above, buoyancy fluxes are also large within the BBL (Fig. 4.9a,b). The vertical average, $\bar{G}$, of the buoyancy flux inside the BBL is shown for both surveys 2 and 3 in Fig. 4.9e,f. Enhanced values are found in particular in the area where the thin, strongly stratified and turbulent halocline interacts with the slope. In this region where the turbulent halocline merges into the turbulent BBL, a clear separation between both mixing regions is no more possible. The most important conclusion from these observations is, however, that the BBL does not collapse at the level of the halocline. Different from the summer situation, therefore, BBL turbulence provides a mechanism for the transport of dissolved substances across the halocline. Below this region, a less stratified BBL (Figs. 4.6c, 4.7c) is found, which is characterized by up to one order of magnitude smaller vertically averaged buoyancy fluxes as discussed in more detail below. BBL buoyancy fluxes decrease strongly above the halocline within the unstratified surface layer, which is of minor interest for our investigation and ignored, consequently. Note, that averaged buoyancy flux $\bar{G}$ includes areas dominated by the length scale l (1.37), even though the validity of the SKIF parametrization (Tab. 2.3) cannot be guaranteed here.

The halocline broadens after the wind event (Fig. 4.10a), and the pronounced band of enhanced buoyancy fluxes and dissipation rates inside the halocline region (Fig. 4.10b) vanishes. Besides arbitrarily occurring turbulence patches in the interior,

a broad, continuous, and strongly turbulent BBL is now the dominant feature in the lowest part of the water column. Importantly, throughout the transect, this BBL is also characterized by strongly enhanced mixing rates $\chi_b = \gamma\varepsilon N^2$ (Fig. 4.10c) as a consequence of the coincidence of stratification and dissipation . Different from the summer situation, BBL mixing is maintained also in the strongly stratified near-bottom region, where the halocline intersects with the sloping topography of the basin. This indicates that BBL mixing supports a turbulent flux across the halocline. At the deep end of the transect, BBL restratification is weaker, and enhanced mixing rates are confined to a weak pycnocline developing at the upper edge of the BBL.

This is also mirrored in the vertically averaged buoyancy flux (Fig. 4.10d), which is strongly increased everywhere in the BBL, without any indications for a collapse inside the halocline region. The vertical averaged mixing rate $\bar{\chi}_b$ (calculation analogously to $\bar{G}$) shows the same behavior (Fig. 4.10d). To estimate the efficiency of BBL mixing, the transect is divided into $2\,\mathrm{km}$ segments for the subsequent analysis. The bulk mixing efficiency Γ defined in (2.10) is calculated for every segment based on the mixing rates and dissipation rates of the BBL as described in section 2.5.4. The first $4\,\mathrm{km}$ of the transect are characterized by an approximately flat bottom, and the bulk mixing efficiency therefore cannot be determined based on the theory for sloping topography developed above. Besides dissipation and mixing rates, the interior stratification N^2_∞ has to be approximated to determine Γ according to 2.11, which is done here by a segment-wise average over the mean density profile across the corresponding depth levels at (a) the central station S1 (S1-case) or (b) the first $4\,\mathrm{km}$ of the transect (T1-case). The resulting bulk mixing efficiency is small at the shallow end of the transect, where the BBL merges into the unstratified surface layer but close to the interior mixing efficiency of $\Gamma = 0.2$ in the upper part of the halocline (Fig. 4.10e, $s > 12\,\mathrm{km}$) for both cases. Below, bulk mixing efficiencies are smaller and strongly depend on the method used to estimate N^2_∞. The bulk mixing efficiencies of the T1-case are consistently smaller than 0.1, whereas the efficiencies of the S1-case increase again in the deeper part. Generally, the use of N^2_∞ at the deep end of the transect (T1-case) seems more consistent because of its proximity to the slope region. Irrespective of the method used to estimate N^2_∞, however, the most important conclusion of this analysis is that BBL mixing is energetic and highly efficient due to BBL restratification near sloping topography.

After discussing the BBLs of single surveys before and after the wind event, both situations can be generalized, focusing on the slope area ($s > 4\,\mathrm{km}$) and excluding the nearly well-mixed surface layer ($\sigma_\theta < 6.5\,\mathrm{kg\,m^{-3}}$). The flux coefficient γ for single

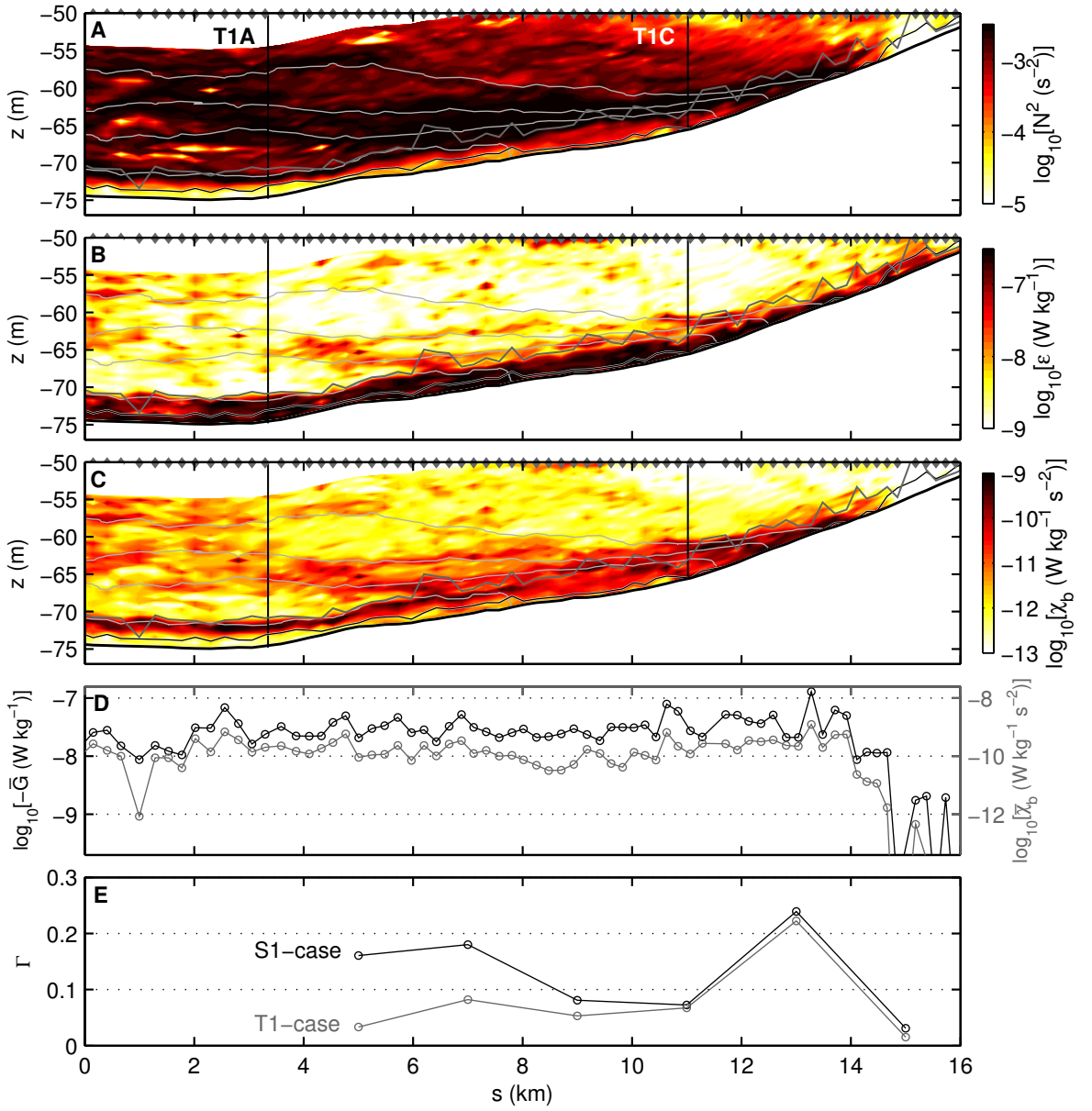

Figure 4.10.: Cross-slope transects of (a) buoyancy frequency, (b) dissipation rate, (c) mixing rate, (d) vertical averaged BBL buoyancy flux (black) and vertical averaged mixing rate (gray) and (e) BBL mixing efficiency for surveys 7. Markers and lines used in (a,b) and (c) are explained in Figs. 4.6 and 4.9. Parameters in (d) and (e) based on BBL data, defined between the bottom (thick black line in (c)) and the BBL-height (thick gray line in (c)). The mixing efficiency (e) is calculated for $2\,\mathrm{km}$ sections. N^2_∞ is interpolated based on the stratification of the central station S1 (van der Lee and Umlauf 2011, S1-case) or the stratification in the deep part of T1 ($s < 4\,\mathrm{km}$, T1-case).

data bins is again calculated by the SKIF-parametrization (Tab. 2.3). The BBL before the wind event (surveys 1 to 4) is characterized by moderate dissipation rates and also

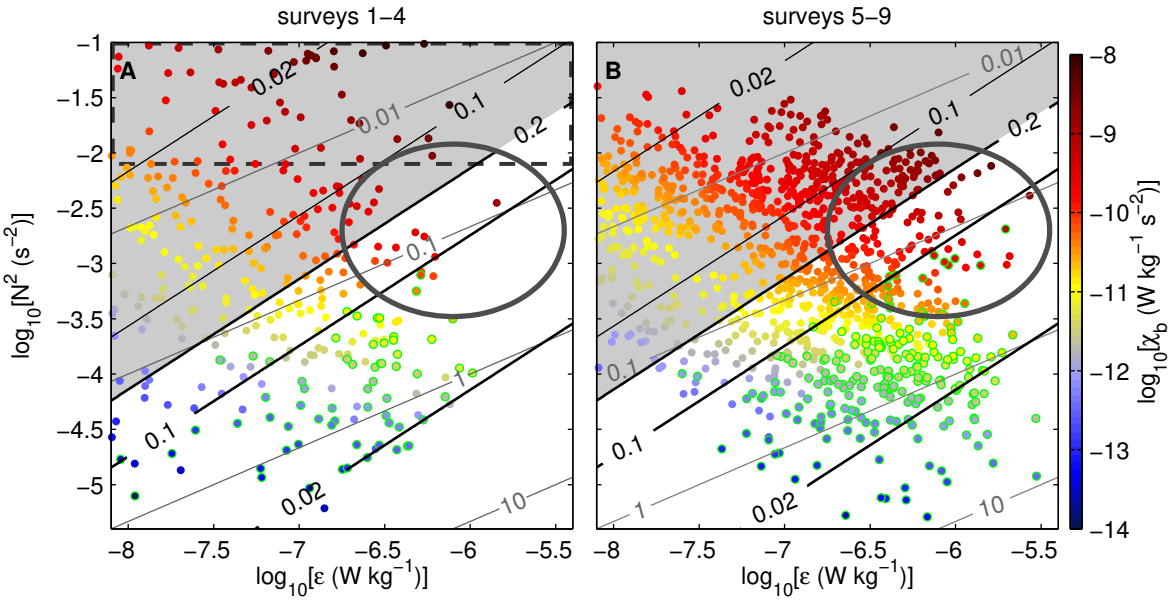

Figure 4.11.: Mixing rate χ_b inside the BBL as a function of stratification and dissipation rate for data points (a) for surveys 1 – 4 and (b) surveys 5 – 9 on transect T1. Gray lines show the Ozmidov scale L_O (in meters). Thick black lines indicate the flux coefficient γ according to SKIF (Tab. 2.3), where the gray area corresponds to $\gamma = 0.2$ (SKIF). Thin black lines inside the gray area indicate the reduced mixing efficiencies suggested by Bouffard and Boegman (2013) (Tab. 2.3) for salinity-stratified flow at low Re_b. Data points affected by wall turbulence ($L_O > \kappa\zeta$) are marked in green. Note the modified axes and color bar in comparison to Fig. 3.5.

moderate stratification (Fig. 4.11a), except for data within the gray dashed rectangle which mainly represent a region with extreme stratification where the halocline meets the BBL. Enhanced mixing rates depend on the coincidence of enhanced dissipation and stratification, which is found only occasionally. Consistent with Fig. 4.10e, the properties in the remaining region below the halocline (region BH) result in a small averaged mixing rate and a small bulk mixing efficiency (Tab. 4.3). These calculations are made for a fixed lower density limit of $12.3\,\mathrm{kg\,m^{-3}}$ to exclude the thin halocline which is characterized by the band of strongly enhanced turbulence. Note, that the upper density limit is set by the beginning of the slope area ($s > 4\,\mathrm{km}$). The averaged interior stratification is about $N^2_\infty = 2.19 \times 10^{-3}\,\mathrm{s^{-2}}$ (based on the T1-case, $N^2_\infty = 1.29 \times 10^{-3}\,\mathrm{s^{-2}}$ for the S1-case)). The mixing parameters of region *BH* are similar to region IV of the summer data (see Fig. 3.5). As a consequence, it can be concluded that region *BH* only provides a small contribution to vertical mixing in the basin below the halocline.

Table 4.3.: Average dissipation and mixing rates defined in (2.11), and bulk mixing efficiency, for BBL regions below halocline (*BH*) and inside halocline (*IH*), respectively. The bulk mixing efficiency is calculated for the T1-case (S1-case in parenthesis). For each region, near-bottom data with $L_O > \kappa\zeta$ are either excluded (first row), included (second row), or assumed to provide no contribution to mixing ($\chi_b = 0$, third row).

region	surveys	near-bottom data	$\overline{\mathcal{E}}$	$N_\infty^2 \overline{\mathcal{E}}_p$	$\Gamma = \overline{\mathcal{E}}_p / \overline{\mathcal{E}}$
			$(10^{-7}\,\mathrm{W\,kg^{-1}})$	$(10^{-11}\,\mathrm{W\,kg^{-1}\,s^{-2}})$	
BH	1 – 4	excluded	0.69	0.59	$0.04\,(0.07)$
		included	1.12	0.37	$0.01\,(0.03)$
		zero mixing	1.12	0.35	$0.01\,(0.02)$
IH	5 – 9	excluded	2.12	11.50	$0.19\,(0.25)$
		included	3.34	8.74	$0.09\,(0.12)$
		zero mixing	3.34	8.63	$0.09\,(0.12)$

After the wind event (surveys 5 – 9), the halocline has broadened and now covers the entire slope region investigated here. It is referred to as region *IH* (inside halocline) in the following. Moreover, the band of strongly enhanced dissipation rates in the halocline region does not exist any more, and a clear differentiation between interior and BBL mixing is possible everywhere. The required averaged interior stratification is again calculated for every survey and is about $N_\infty^2 = 3.04 \times 10^{-3}\,\mathrm{s^{-2}}$ (T1-case, or $N_\infty^2 = 2.25 \times 10^{-3}\,\mathrm{s^{-2}}$ for S1-case). The mixing rates in the scatter diagram (Fig. 4.11b) are displaced to stronger stratification and, due to higher near-bottom velocities (Fig. 4.8a), to enhanced dissipation rates in comparison to the situation before the wind event (Fig. 4.11a). The coincidence of both stratification and dissipation leads to enhanced mixing rates. This behavior is already known from region II (above halocline) of the summer slope (Fig. 3.5), where the most energetic mixing region was marked by a gray ellipse, which is also placed in Figure 4.11 as a guidance. Stratification in region *IH* is slightly larger than that of region II of the summer slope, which was also characterized by the halocline. There, an upslope moving branch of the summer halocline caused strong stratification. Region *IH* has a bulk mixing efficiency of 0.09 ("zero mixing" case) which is approximately half of the value of region II (Tab. 3.2), mainly due to the smaller interior stratification N_∞^2 in the latter. Note that the bulk mixing efficiency would be reduced to $\Gamma = 0.07$ if the lost dissipation in the immediate

vicinity of the sediment-water interface would have been included (see also section 3.4).

The bulk mixing efficiency of region *IH* is smaller than the interior mixing efficiency of $\Gamma = 0.2$ but still of the same order of magnitude. However, in contrast to the collapse of the BBL in the halocline region in summer, the winter BBL remains strongly turbulent even in the halocline region, and therefore provides an important mechanism for the vertical transport of dissolved substances across this density interface.

4.4. Inside the sharp halocline

4.4.1. MSS data

The halocline is characterized by a sharp interface around the T1C mooring (Figs. 4.6, 4.7) during the first surveys along transect T1. As mentioned above, this interface strongly contributes to the vertical buoyancy flux, and is therefore investigated in more detail in the following. Of special interest is the possibility of double-diffusive instability (diffusive convection) suggested by strong inverse temperature gradients observed in the vicinity of this interface (see Fig.4.12a,b). The first part of this analysis will be based on a carefully selected and representative MSS cast obtained during survey 3 close to the T1C mooring (see Fig. 2.1). It should be recalled that data from the precision CTD sensors of this instrument are available at $0.1\,\mathrm{m}$ resolution. These data are complemented by high-resolution temperature observations from a single FP07 fast thermistor with a response time of the order of $10\,\mathrm{ms}$ (referred to "mT" in the following).

As shown in Fig. 4.12, the width of the pycnocline at this location is smaller than $0.5\,\mathrm{m}$ and characterized by a salinity jump of more than $5\,\mathrm{g\,kg^{-1}}$ (Fig. 4.12c) and a simultaneous inverse temperature jump of more than $4\,^{\circ}\mathrm{C}$ (Fig. 4.12a). It is worth noting that the strongest halocline identified in the entire data set was found during survey 2 where changes of $6\,\mathrm{g\,kg^{-1}}$ and $6\,^{\circ}\mathrm{C}$ across an interface of comparable thickness were observed. The buoyancy frequency squared (Fig. 4.12d) exceeds values of $0.1\,\mathrm{s^{-2}}$, corresponding to a buoyancy period of only 20 seconds. If these data are low-pass filtered to $0.5\,\mathrm{m}$ vertical resolution (corresponding to the resolution of the dissipation rate estimates), interfacial stratification is underestimated by more than a factor of 2. The buoyancy frequency can be split into contributions from conservative

temperature Θ and absolute salinity S_A:

$$N^2 = g\left[\alpha_\Theta \frac{\mathrm{d}\Theta}{\mathrm{d}z} - \beta_\Theta \frac{\mathrm{d}S_A}{\mathrm{d}z}\right] \tag{4.3}$$

where the gravitation constant g, the thermal expansion coefficient α_Θ and the haline contraction coefficient β_Θ were introduced. The relative importance of temperature and salinity is conveniently quantified by the density ratio

$$R_\rho = \frac{\beta_\Theta \dfrac{\mathrm{d}S_A}{\mathrm{d}z}}{\alpha_\Theta \dfrac{\mathrm{d}\Theta}{\mathrm{d}z}} \tag{4.4}$$

which also allows for a classification of double-diffusive regimes in the Baltic Sea. According to Kuzmina et al. (2005) the diffusive regime of double diffusion corresponds to a density ratio in the range $1 < R_\rho < 15$. For R_ρ larger than 15, the temperature profile is still inverse, but the salinity stratification suppresses instabilities. The observed density ratios in the vicinity of the interface (Fig. 4.12e) indicate the possibility of double-diffusive convection only in the region below the halocline. However, large differences in the computed values of R_ρ based on the precision CTD sensor and the FP07 fast thermistor, respectively, suggests that our data are not particularly reliable in this region. Interestingly, despite the downward increasing temperatures, density ratios become negative in the upper part of the interface above $z = -61.5\,\mathrm{m}$, as a result of a changing density-to-temperature relation reflected in negative thermal expansion coefficient at the very low local temperatures (less than $2\,^\circ\mathrm{C}$). The water is stably stratified here. Concluding, diffusive convection cannot occur in the upper part of the interface, and is unlikely to play a role in the lower part, where the interface merges into the vigorously turbulent BBL (see above).

It therefore appears more likely that the steppy structures are generated by shear instabilities. Holmboe instabilities are favored if the shear interface is broader than the density interface (e.g. Carpenter et al. 2011), which is expected in view of the very thin density interface found in the data. It may be speculated that the steps exactly above the halocline (Fig. 4.12a) are generated by such instabilities. However, there is no indication for such instabilities in the high resolution temperature data (Fig. 4.13). The TLADCP data indicate the presence of shear, but vertical resolution and data quality are not sufficient to draw any definite conclusions.

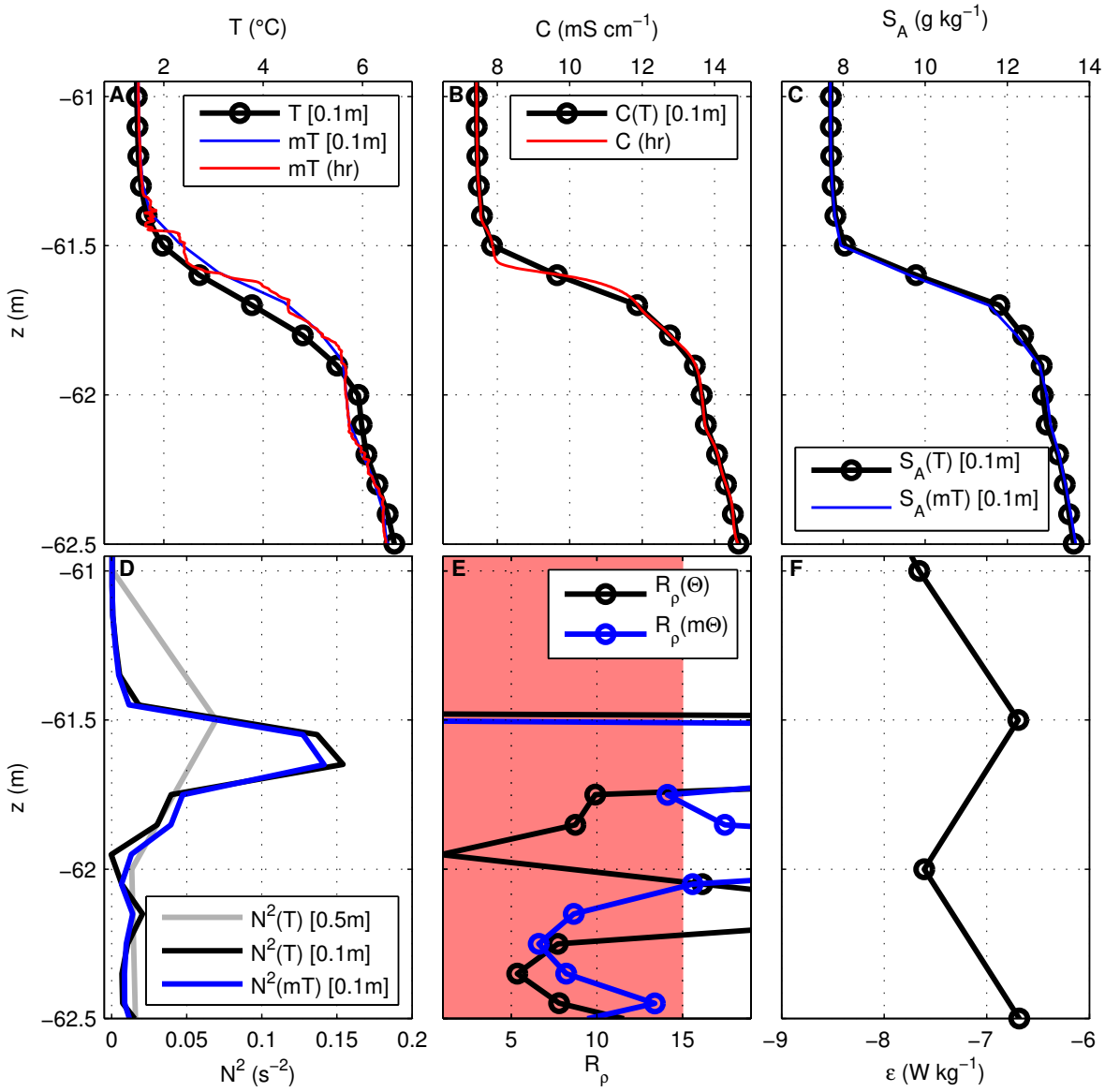

Figure 4.12.: Vertical profiles of (a) temperature T, (b) conductivity C, (c) salinity S_A, (d) buoyancy frequency squared N^2, (e) density ratio R_ρ and (f) dissipation rate ε observed by the MSS90 profiler close to position T1C during the third survey (Fig. 4.7) along transect T1. The red-shaded area marks the range where double diffusive convection may occur in (f). The abbreviations stand for: [0.1m] – $0.1\,\mathrm{m}$ resolution, hr – high resolution ($256\,\mathrm{Hz}$, see section 2.2.1).

Moreover, the sharp interface enables conclusions about the quality of data processing or the handling of the response times of the sensors. One adjustment is a vertical shift of the temperature profile during the post-processing to compensate response time differences in comparison to the conductivity sensor (section 2.2.1). The final CTD temperature profile is given in Figure 4.12a. In contrast, the FP07 profile

was shifted vertically to fit to the conductivity profile at $256\,\mathrm{Hz}$ resolution (Fig. 4.12b). This profile shows the same staircases as the FP07 profile but in minor shape. As a consequence the temperature profiles of CTD and FP07 do not overlap within the halocline. The deviation is about some centimeters and can result in rough estimates for the derived quantities in Figures 4.12c-e. This point should be the reason for the differences and inaccuracies in the density ratio profiles (Fig. 4.12e). Further investigation and evaluation is needed to improve the vertical adjustment of the temperature profile, but this is not in the scope of this study. Nevertheless the investigation of mixing parameters like the buoyancy fluxes and diffusivities in the last sections is not affected significantly, because the analysis is based on a coarser, $0.5\,\mathrm{m}$ resolution.

The dissipation rate (Fig. 4.12f) is enhanced within the halocline and exceeds the averaged dissipation rate in the center of the basin (van der Lee and Umlauf 2011) by one to two order of magnitude. The dissipation rates do not decrease towards the noise level below the halocline as they do in the center of the basin, because the interface is located $4.7\,\mathrm{m}$ above the bottom at position T1C. The velocities (Fig. 4.7a,b) indicate the presence of bottom shear as the source for the BBL turbulence. A precise separation in halocline dissipation and BBL dissipation is not possible, as already explained.

4.4.2. High resolution temperature data

A high resolution temperature chain was deployed at station T1C as explained in detail in section 2.3. The data of the lowest $15\,\mathrm{m}$ are presented in Figure 4.13a. This depth section shows the evolution of the inverse thermocline during the T1C measurements. In general, a functional interrelation between temperature and density does not exist for a salinity-stratified system. However, as discussed in the previous subsection, the sharp inverse thermocline is characterized by a jump in salinity as well (Figure 4.12a,c). Accordingly, the evolution of the temperature interface is a good proxy for the pycnocline evolution, especially during the first half of the T1C measurements, where the interface is very thin. During this period, it is reasonable to assume that the high-frequency thermocline motions described in the following reflect similar isopycnal motions. In the second half, the temperature interface becomes broader and now also includes two less stratified areas above and below. Intrusions can be observed in these areas, e.g. between the times marked by 5 and 6 at a distance of approximately $7\,\mathrm{m}$ above the bottom.

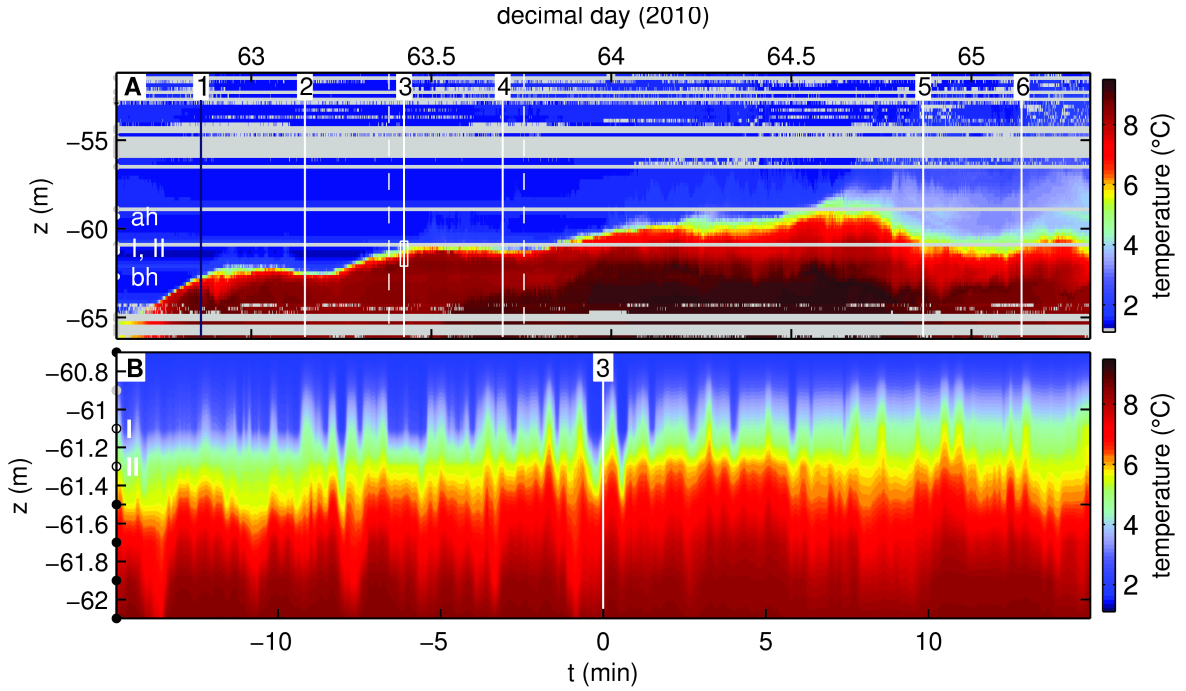

Figure 4.13.: Time series of (a) high resolution temperature and (b) an enlarged section of it. Gray areas indicate places of no data. Vertical white lines denote times when the ship passed the mooring position. The survey numbers are listed on top. Circles on the left denote sensor positions. Gray colored sensors indicate time series where more than $75\,\%$ of the data were corrupted. Power spectral densities (psd's in Fig. 4.14) based on gray markers with a black edge and labeled by ah, I, II, bh. White-dashed, vertical lines define the limits for the time series that are included in the psd calculation.

A detailed view that focuses on the interface variability is given in Figure 4.13b. It was recorded at the same time at the neighboring MSS cast presented in Figure 4.12. Fluctuations in temperature show irregular oscillations with periods of a few minutes. Isothermal displacements are typically $0.1\,\mathrm{m}$ – $0.3\,\mathrm{m}$ in the interface region. Some displacements appear abruptly and are characterized by changes in temperature of several degrees Celsius, vertically correlated over several neighboring sensors. An obvious explanation would be that the "steppy" temperature profile (Fig. 4.12a) is vertically advected in the velocity field, such that temperature steps pass by the sensors. However, a corresponding -2 slope in the temperature spectrum (Fig. 4.14) as suggested by Phillips (1971) is not observed. In contrast, the spectra inside the halocline are characterized by a -1 slope in the internal wave band for frequencies below N and a -3 slope for higher frequencies. Van Haren and Gostiaux (2009) found a similar behavior for a "steppy" temperature environment in the open Canary Basin, although their spectra decreased with a slope of -2.5 instead of -3 for higher fre-

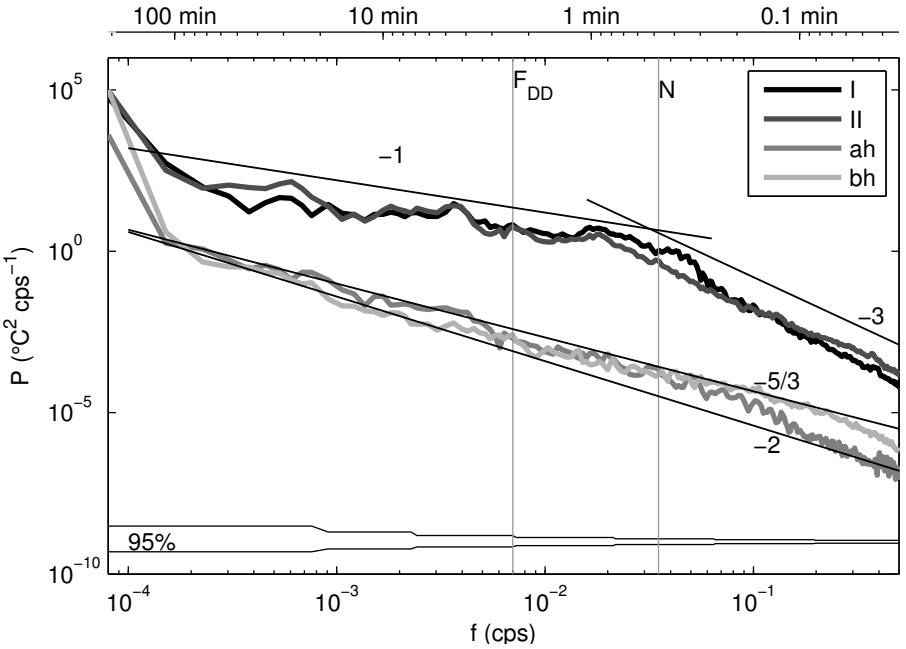

Figure 4.14.: Power spectral density of temperature data. Corresponding sensors and the limits of the time series are marked in Fig. 4.13. Vertical gray lines denote the frequency of the most unstable mode F_{DD} and the buoyancy frequency N, both for sensor I. Thin black lines indicate slopes of n, whereas n's are given beside the lines.

quencies. It should be noted, that the inertial frequency is not resolved by the chosen time series, and that the buoyancy frequency N (Fig. 4.14) is only a rough estimate based on the halocline value taken from the MSS measurement (Fig. 4.12d). Moreover, several peaks are pronounced and exceed the background shape of the spectra. The $95\,\%$ confidence interval is exceeded by the broad power spectral density peak around $4.5\,\mathrm{min}$ for the two sensors inside the interface region and broad peaks around $1\,\mathrm{min}$ and $0.3\,\mathrm{min}$ for sensor I. A classification of these peaks to individual processes is not possible. The frequency of the most unstable double diffusive mode, which is given by Turner (1973) as

$$F_{DD} = \sqrt{\frac{1-\tau}{3(Pr+1)}} N \approx \frac{1}{5} N \quad , \tag{4.5}$$

is added to the spectrum in Figure 4.14 but does not stand out (here, the diffusivity ratio is denoted as τ and the Prandtl number as Pr). This supports the conclusion above that double-diffusive does not play a relevant role in the interface region. For lower frequencies, it becomes increasingly likely that the power spectral density is

influenced by intrusions such that a direct relation between temperature and isopycnal fluctuations becomes questionable.

The spectra above and below the interface (ah and bh respectively) differ strongly from the spectra inside the halocline (I and II). The power spectral density is smaller and the spectral slope varies between $-5/3$ and -2. The background stratification of these sensors is much smaller ($\approx 1 \times 10^{-3}\,\mathrm{cps}$) and a change in the spectral slope cannot be found in contrast to the spectra of the halocline. Although the spectral slope of approximately -2 suggest staircases, their occurrence in the surface layer is implausible, because the surface layer is well-mixed and can be assumed to be homogeneous.

4.5. Conclusion

The cross-slope data is characterized by a permanent BBL covering the whole transect. The BBL regions within the halocline can be identified as places where boundary mixing is efficient. Enhanced mixing rates and bulk mixing efficiencies of 0.1 can be found. As a result, the BBL is an important place for mixing and for mixing through the halocline. A further conspicuous feature is a thin and strongly stratified halocline which can be split into two parts. The broader part is located where the transect is deepest, here stratification and dissipation rates are similar to the interior values (compare with van der Lee and Umlauf 2011). A compressed and strongly stratified halocline occurs in the vicinity of the boundary as a result of the interaction between a mesoscale eddy and the sloping boundary. Moreover, this interface is characterized by strong turbulence. Highly-resolved temperature profiles show step-like behavior within the area of the halocline. These steps and calculated density ratios indicate the presence of double diffusive convection. An analysis of temperature spectra does not confirm this assumption. However, this process would not be powerful enough to generate the dissipation rates of the sharp interface. Shear instabilities are likely to be the main process behind the turbulence. Van der Lee and Umlauf (2011) explain the relationship between layers of enhanced shear and pronounced dissipation rates within the halocline of the basin. Besides the normally assumed Kelvin-Helmholtz instabilities, Holmboe instabilities may also occur, because it can be estimated that the shear interface is broader than the thin halocline. Indeed, velocity measurements did not allow satisfying shear calculation.

In the discussion of diapycnal mixing, buoyancy fluxes are the crucial physical mixing quantities outside the BBL. The investigation of halocline buoyancy fluxes leads to two final statements. Firstly, enhanced buoyancy fluxes appear inside the virtually arbitrarily occurring layers of pronounced dissipation rates. These layers clearly increase the vertical-averaged buoyancy fluxes within the halocline. Regarding this, a pronounced version of such a layer occurs within the thin and strongly stratified halocline interface. This layer vanishes completely, as soon as the halocline broadens. Thus, there is no direct linkage between stratification and turbulence. Shear instabilities are needed to generate turbulence as a background process. The second statement concerns the magnitudes of the buoyancy fluxes, which are overestimated using a flux coefficient of $\gamma = 0.2$ in the area of the halocline. The corresponding balance between dissipation rate and buoyancy flux is not an appropriate assumption in strongly salinity-stratified systems. Turbulent, vertical-advected water parcels are not mixed at the new location, they are mostly restratified (Bouffard and Boegman 2013).

Chapter 5.

Summary and Outlook

5.1. Summary

The main focus of this thesis was to investigate the role of boundary mixing in non-tidal basins. The investigation was based on two season-specific cross-slope data sets from the Bornholm Basin, which included high resolution CTD, microstructure shear and velocity data along an approximately $15\,\mathrm{km}$ long transect. Turbulent areas were found in the interior as well as at the sloping boundary of the transect.

The summer data set was characterized by the presence of the permanent halocline and a seasonal thermocline, which resulted in a three-layered structure of the water column and a dominating mode-2 near-inertial wave motion. The turbulent BBL had a height of a few meters, interrupted by a section of suppressed turbulence where the halocline interacts with the sloping boundary. A reduction of turbulence generating bottom shear and the damping effect of stratification add up to this BBL gap. In consequence, there is no contribution to diapycnal mixing though the halocline by the BBL in summer. The cross-halocline transport is exclusively done by arbitrarily occurring near-inertial wave shear layers in the interior as explained by van der Lee and Umlauf (2011). Above the halocline, the importance of BBL mixing increases, because this boundary layer section is highly turbulent and permanently being restratified by an upslope moving upper branch of the halocline during the observations. It was shown, based on the theory of Umlauf et al. (2015), that this specific BBL, which combines strong stratification and enhanced dissipation rates, is characterized by high mixing rates, where the bulk mixing efficiency even exceeds the mixing efficiency $\Gamma = 0.2$ (Osborn 1980) of the interior. This is a remarkable result and contradicts the usual

assumption that boundary mixing is not efficient since it mainly stirs already mixed water (Garrett 1979). The contribution to mixing of this BBL region exceeds the contribution of the interior in the same density range. As a result, near-inertial wave induced boundary mixing can be efficient and an important contribution to diapycnal mixing in a basin.

The winter data set was characterized by the permanent halocline, which separated the well-mixed, brackish surface layer from the saline bottom pool. Consequently, the investigation of mixing was restricted to the halocline and the BBL within and below the halocline. Velocities were dominated by mode-1 near-inertial wave motions (van der Lee and Umlauf 2011). Turbulence levels were enhanced within the halocline during the winter in comparison to the summer. This observation is consistent with the findings of van der Lee and Umlauf (2011) for the center of the basin; it is a consequence of the increased occurrence of storms and correspondingly enhanced energy levels in the internal wave field. In contrast to summer, the BBL is characterized by enhanced stratification and turbulence inside the halocline. The calculated mixing rates and bulk mixing efficiencies indicate the importance of boundary mixing for the diapycnal mixing and, opposite to the summer measurements, also for mixing through the halocline in the Bornholm Basin. Further, a very thin ($< 0.5\,\mathrm{m}$), up to $7\,\mathrm{km}$ long and strong stratified halocline was found as a consequence of a mesoscale eddy interacting with the sloping boundary. This interface was further characterized by an enhanced shear layer and pronounced turbulence. The averaged buoyancy flux within this interface exceeds the averaged buoyancy flux of the broader halocline found in the deeper part of the transect by one order of magnitude. This feature illustrates the importance of arbitrarily occurring layers of enhanced dissipation and buoyancy fluxes within the halocline to transport salt and other tracers though the halocline.

Furthermore, this investigation also discussed the reduction of the flux coefficients γ in small buoyancy Reynolds number flows. This effect is not negligible in the Baltic Sea, because it concerns most of the halocline. The already small buoyancy fluxes were reduced by up to one order of magnitude comparing the often used SKIF-parametrization with the more recent BB-parametrization (Tab. 2.3). The main reason is the process of restratification in salinity-stratified systems. However this reduction does not contradict the importance of the arbitrarily occurring turbulent shear layers as places where the diapycnal transport inside the halocline is done.

5.2. Outlook

Several questions and challenges appear by the investigation of the cross-slope data and the discussion of boundary mixing. In the following, points for future work are listed.

Both summer and winter cross-slope investigations showed locations of enhanced mixing, but it is still unclear how representative these findings are for the respective season. A limitation of the data is the spatial restriction to a specific slope in the southeast of the basin and the short time series that cover only a few inertial cycles. An investigation of further smoother and steeper slopes as well as longer time series would be important to verify and extent the conclusions made. The following questions are raised in respect to the observations: Is the BBL which vanishes inside the halocline and which shows highly efficient mixing in the winter water of section 3.3.1 a feature found accidentally, a characteristic of the observed slope or a typical feature in the Bornholm Basin? How often does a very thin and turbulent halocline (section 4.4) occur near the boundary? Is the interaction of a mesoscale eddy and a sloping boundary a necessary condition for such a sharp interface?

The properties of the sharp interface in the winter data were discussed in section 4.4. It was also stated that the vertical resolution of e.g. N^2 of the sharp interface is limited by the adjustment of the temperature and conductivity profiles. The adjustment is an important step to consider the different sensor response times. An inaccurate adjustment leads to spikes in the salinity or other derived quantity profiles. The profiles in Figure 4.12 indicate a good but still improvable vertical adjustment of the temperature sensor. Peter Holtermann (IOW) and Hartmut Prandtke (ISW) are working on a slide that allows a precise movement of the MSS sensors in a laboratory fluid. An investigation of a well-defined interface would give a reliable statement about the response times of the sensors. The post-processing of the MSS data would be improved by the outcome of these measurements and may increase the vertical resolution of derived quantities.

The cross-slope data includes the vessel-mounted ADCP velocities, as is done in many studies. A specialty here was the usage of a towed and lowered ADCP to record velocities close to the bottom, where the VMADCP is already blind. The measurements were performed in parallel to the MSS measurements and the operation of MSS and TLADCP works excellent in shallower waters. As a consequence, the TLADCP was

also used in more recent field studies. The TLADCP and the VMADCP give a good impression of the velocity structure. Nevertheless, the data are of limited suitability for shear discussions, because the VMADCP and especially the TLADCP data are very noisy. A moored ADCP covering the halocline is recommended. Corresponding ADCPs were deployed and fished by a trawler in both investigations. Further, a temporarily, and spatially, highly resolved velocity profiler would be a useful device to investigate the halocline in more detail. Corresponding data were collected with Aquadopps (Nortek) during ILWAO-II cruises in 2014 and 2015. These records may enable the investigation of internal waves also at the high-frequency edge.

The buoyancy flux is a main quantity in the discussion of mixing and is still not validated well enough. The critical point is the parametrized determination of the flux coefficient (see also Tab. 2.3). The SKIF-parametrization was used in several studies and is well validated close to the boundaries, where stratification decreases, turbulence increases and the buoyancy Reynolds numbers are enhanced (> 100). Nevertheless, direct buoyancy flux measurements like in Walter et al. (2014) could verify the used SKIF-parametrization also for the salinity stratified environment in the Baltic Sea. In contrast, the SKIF-parametrization seems not to be the ideal parametrization for the strongly stratified halocline, where buoyancy Reynolds numbers are small and a restratification of turbulently-advected water parcels (Bouffard and Boegman 2013) takes place. The usage of the BB-parametrization reduces the buoyancy fluxes by one order of magnitude in comparison to SKIF. A good validation of the coefficient flux parameterizations in the Baltic Sea based on direct buoyancy flux measurements methods is important to study the cross-halocline fluxes in more detail!

Appendix A.

Data analysis

A.1. Dissipation rates and spectra

The dissipation rate of turbulent kinetic energy is one of the main physical quantities in this thesis. It is displayed in several figures, like 3.3d or 4.3b, and is used to calculate quantities like the bulk mixing efficiency, the buoyancy flux, or the Ozmidov length scale, please see chapter 4. Therefore, theory and implementation of the algorithm used to estimate dissipation rates in this thesis are discussed in detail in this section.

A.1.1. Spectra

The turbulent kinetic energy tke is defined as:

$$tke = \frac{1}{2}\langle u_i u_i \rangle = \int_0^\infty E(k)\,\mathrm{d}k. \tag{A.1}$$

It is the half of the mean square of the velocity fluctuations u_i (variance of velocity) or, likewise, the integral of the scalar energy spectrum $E(k)$, where k is the modulus of the wave vector $\boldsymbol{k}$. The energy spectrum is defined as

$$E(k,t) = \frac{1}{2}\int \phi_{ii}(\mathbf{k},t)\,\mathrm{d}\sigma, \tag{A.2}$$

where $\mathrm{d}\sigma$ is a surface element of a sphere with the radius k and t is the time. The spectrum tensor

$$\phi_{ij}(\mathbf{k},t) = \frac{1}{(2\pi)^3} \iiint_{-\infty}^{\infty} R_{ij}(\mathbf{r},t)\mathrm{e}^{-i\mathbf{k}\cdot\mathbf{r}}\,\mathrm{d}\mathbf{r}, \tag{A.3}$$

is the Fourier transform of the correlation tensor $R_{ij}(\mathbf{r}) \equiv \overline{u_i(\mathbf{x},t)u_j(\mathbf{x}+\mathbf{r},t)}$, where $\mathbf{x}$ is the coordinate vector and $\mathbf{r}$ is a distance vector. The time dependence of the sprectra is ignored in the following. As shown by Olbers et al. (2012) p.337 for isotropic turbulence can be reduced to

$$\phi_{ij}(\mathbf{k}) = \frac{E(k)}{4\pi k^4}\left(k^2\delta_{ij} - k_i k_j\right), \text{ with } \quad \delta_{ij}\begin{cases} 1 & i=j \\ 0 & \text{otherwise} \end{cases} \quad . \tag{A.4}$$

In addition, Olbers et al. (2012) p. 337 emphasize: *The scalar energy spectrum $E(k)$ is the preferred variable for a discussion of isotropic turbulent flows*.
In practice, it is often only possible to measure one-dimensional spectra of the form (Pope 2000)

$$F_{ij}(k_1) \equiv \frac{1}{\pi}\int_{-\infty}^{\infty} R_{ij}(\mathbf{e}_1 r_1)\mathrm{e}^{ik_1 r_1}\,\mathrm{d}r_1 \quad . \tag{A.5}$$

The longitudinal and transverse spectra F_{11} and F_{22} for and real signal are needed for our purpose:

$$F_{11}(k_1) = \frac{1}{\pi}\int_{-\infty}^{\infty} R_{11}(\mathbf{e}_1 r_1)\mathrm{e}^{ik_1 r_1}\,\mathrm{d}r_1 = \frac{2}{\pi}\int_0^{\infty} R_{11}(\mathbf{e}_1 r_1)\cos\left(k_1 r_1\right)\,\mathrm{d}r_1 \quad , \tag{A.6}$$

$$F_{22}(k_1) = \frac{1}{\pi}\int_{-\infty}^{\infty} R_{22}(\mathbf{e}_1 r_1)\mathrm{e}^{ik_1 r_1}\,\mathrm{d}r_1 = \frac{2}{\pi}\int_0^{\infty} R_{22}(\mathbf{e}_1 r_1)\cos\left(k_1 r_1\right)\,\mathrm{d}r_1 \quad . \tag{A.7}$$

The corresponding inverse Fourier transformations are given as:

$$R_{11}(\mathbf{e}_1 r_1) = \int_0^{\infty} F_{11}(k_1)\cos\left(k_1 r_1\right)\,\mathrm{d}k_1 \quad , \tag{A.8}$$

$$R_{22}(\mathbf{e}_1 r_1) = \int_0^{\infty} F_{22}(k_1)\cos\left(k_1 r_1\right)\,\mathrm{d}k_1 \quad . \tag{A.9}$$

The spectrum F_{22} (F_{11}) can be obtained by a profiler which measures velocity fluctuations transverse (longitudinal) to its moving direction. Please note, that the first component of the coordinate system is rotated in the direction of the moving profiler. The spectra F_{22} and F_{33} are identical for isotropic turbulence (as a result F_{33} is not

listed) and $F_{ij} = 0$ if $i \neq j$. It is important to mention, that turbulence is almost not isotropic in the ocean. Assuming an eddy that is generated by a shear flow has a preferred orientation. This initial eddy generate smaller eddies and so on. In this energy cascade from large to small scales the information of the initial direction is lost. It can be assumed that turbulence is isotropic for these small scales. At the end of the cascade the energy is dissipated into internal energy.
The one-dimensional longitudinal and transverse spectra are related to the spectrum tensor via (Pope 2000)

$$F_{11}(k_1) = 2 \iint_{-\infty}^{\infty} \phi_{11} \, \mathrm{d}k_2 \, \mathrm{d}k_3 \quad , F_{22}(k_1) = 2 \iint_{-\infty}^{\infty} \phi_{22} \, \mathrm{d}k_2 \, \mathrm{d}k_3 \quad . \tag{A.10}$$

It is also possible to relate it to the energy spectrum, assuming isotropic turbulence, as shown by Pope (2000) (p.226f):

$$F_{11}(k_1) = \int_{k_1}^{\infty} \frac{E(k)}{k} \left(1 - \frac{k_1^2}{k^2}\right) \, \mathrm{d}k \quad , \tag{A.11}$$

$$E(k) = \frac{1}{2} k^3 \frac{\mathrm{d}}{\mathrm{d}k} \left(\frac{1}{k} \frac{\mathrm{d}F_{11}(k)}{\mathrm{d}k}\right) \quad , \tag{A.12}$$

$$F_{22}(k_1) = \frac{1}{2} \left(F_{11}(k_1) - k_1 \frac{\mathrm{d}F_{11}(k_1)}{\mathrm{d}k_1}\right) \quad . \tag{A.13}$$

A.1.2. Dissipation rate

The dissipation rate is defined as:

$$\varepsilon = \int_0^{\infty} 2\nu k^2 E(k) \, \mathrm{d}k \tag{A.14}$$

for isotropic turbulence, where ν is the molecular viscosity, k the wave number and $E(k)$ the scalar energy spectrum. This definition was derived with the help of the Fourier transformation of the velocity covariance equation (Olbers et al. (2012), p. 339ff; Batchelor (1953), section 5.1.). The dissipation rate can be expressed in terms

of the longitudinal one-dimensional spectrum F_{11}

$$\begin{aligned}
\varepsilon &= \int_0^\infty 2\nu k^2 E(k)\,\mathrm{d}k \\
&= \int_0^\infty 2\nu k^2 \frac{1}{2} k^3 \frac{\mathrm{d}}{\mathrm{d}k}\left(\frac{1}{k}\frac{\mathrm{d}F_{11}(k)}{\mathrm{d}k}\right)\,\mathrm{d}k \\
&= \int_0^\infty \nu k^5 \frac{\mathrm{d}}{\mathrm{d}k}\left(\frac{1}{k}\frac{\mathrm{d}F_{11}(k)}{\mathrm{d}k}\right)\,\mathrm{d}k \\
&= \left[\nu k^5 \frac{1}{k}\frac{\mathrm{d}F_{11}(k)}{\mathrm{d}k}\right]_0^\infty - \int_0^\infty \nu 5k^4 \frac{1}{k}\frac{\mathrm{d}F_{11}(k)}{\mathrm{d}k}\,\mathrm{d}k \\
&= 0 - 5\nu \int_0^\infty k^3 \frac{\mathrm{d}F_{11}(k)}{\mathrm{d}k}\,\mathrm{d}k \\
&= -\left[5\nu k^3 F_{11}(k)\right]_0^\infty + \int_0^\infty 5\nu 3k^2 F_{11}\,\mathrm{d}k \\
&= 15\nu \int_0^\infty k^2 F_{11}\,\mathrm{d}k
\end{aligned} \tag{A.15}$$

by using (A.12). Taking into account that F_{11} vanishes for an infinite wave number, see for example Tennekes and Lumley (1972) on page 255. In case of isotropic turbulence, a single one-dimensional spectrum is sufficient to describe the turbulence.

The dissipation rate in (A.15) is calculated via the longitudinal one-dimensional spectrum F_{11}. Thus velocity fluctuations in direction of the movement u_1 are measured. In view of a vertical falling profiler (like the MSS90-L), which measures horizontal velocity fluctuations u_2, a dependency of the transverse one-dimensional spectrum is needed. A corresponding relation that combines both one-dimensional spectra for isotropic turbulence is given by Batchelor (1953) (in his section 6.4)

$$\int_0^\infty k_1^2 F_{11}(k_1)\,\mathrm{d}k_1 = \frac{1}{2}\int_0^\infty k_1^2 F_{22}(k_1)\,\mathrm{d}k_1 \quad , \tag{A.16}$$

which can easily be proven by using (A.13). The equation (A.15) can be rewritten into

$$\varepsilon = \frac{15}{2}\nu \int_0^\infty k_1^2 F_{22}(k_1)\,\mathrm{d}k_1 \tag{A.17}$$

$$= \frac{15}{2}\nu \left\langle \left(\frac{\partial u_2}{\partial x_1}\right)^2 \right\rangle \tag{A.18}$$

by using equations (A.16), (A.9) and the relation

$$\left\langle \left(\frac{\partial u_2}{\partial x_1} \right)^2 \right\rangle = - \left[\frac{\partial^2 R_{22}(\mathbf{e}_1 r_1)}{\partial r_1^2} \right]_{r_1=0} \tag{A.19}$$

which describes a property of a derivative of a stationary random function (e.g. Appendix A.3.2 of Olbers et al. 2012). As final step Parsevals theorem is used. It states that a variance can be written as the integral of the spectrum. Therefore, as a result, the dissipation rate of turbulent kinetic energy in isotropic turbulence is defined as:

$$\varepsilon = \frac{15}{2} \nu \int_0^\infty S(k_1) \, \mathrm{d}k_1 \quad , \tag{A.20}$$

where the vertical shear spectrum $S(k_1)$ is introduced.

A.1.3. Turbulence profiler

Our turbulence profiler MSS90-L includes two microstructure shear probes. The measuring principle is summarized and explained by Prandke (2005). The main idea is that horizontal velocity fluctuations deflect the dip of the shear probe. Furthermore, the deflection is translated to a voltage by a piezoceramic element according to the relation given by Prandke (2005):

$$E = 2\sqrt{2} \rho G S_{\mathrm{rms}} u V \quad , \tag{A.21}$$

where the density ρ, the voltage gain G, the profiler falling speed V and the horizontal velocity u are introduced. This relation can be directly transformed to an equation for the vertical shear:

$$\frac{\partial u}{\partial z} = \frac{1}{2\sqrt{2} \varrho G S_{\mathrm{rms}} V^2} \frac{\partial E}{\partial t} \tag{A.22}$$

using Taylors "frozen-turbulence" assumption, which states that the turbulent field does not change during the passage of the profiler, and therefore the time derivative can be translated to a vertical derivative:

$$\frac{\partial u}{\partial z} = \frac{1}{V} \frac{\partial u}{\partial t} \quad . \tag{A.23}$$

Both equations (A.21) and (A.23) are based on the assumption that $u \ll V$.
During the post-processing the determined shear is cut in segments and the dissipation rate is calculated for every segment by an integral of the vertical shear spectrum, using equation (A.20). This procedure is explained in section 2.2.1.

A.2. Speed of sound correction

The speed of sound is needed to assign the incoming acoustic signal to equally-distributed length segments, based on the run time of the signal. Subsequently, an average velocity is calculated for every segment. In the following, a simple example is constructed to demonstrate the influence of the salinity on the speed of sound and the resulting length and velocity estimates. For a representative surface layer temperature of $16\,^{\circ}\mathrm{C}$, which is seen by the vessel mounted ADCP (VMADCP), the speed of sound for salinities of $35\,\mathrm{g\,kg^{-1}}$ (representing the standard value used by the ADCPs) and $10\,\mathrm{g\,kg^{-1}}$ (representing a realistic value for the Baltic Sea) is: v_{35} =1509 $\mathrm{m\,s^{-1}}$ and v_{10} =1480 $\mathrm{m\,s^{-1}}$. This difference in speed of sound leads to an overestimation of the distance to the sea ground of approximately $1.5\,\mathrm{m}$. The relation is more complicated in the real water column, because both temperature and salinity vary strongly as discussed in the following.
The MSS profiler provides high resolution CTD data that are used here to calculate the speed of sound in the water column, and correct the values computed by the internal ADCP processing software that are based on constant temperature and salinities.
The distance

$$s_{i,i+1}^{\mathrm{ADCP}} = z_i^{\mathrm{ADCP}} - z_{i+1}^{\mathrm{ADCP}} \tag{A.24}$$

between two neighboring ADCP z bins (number i and the following $i+1$), is calculated by the equation

$$s_{i,i+1}^{\mathrm{ADCP}} = \frac{1}{2} c_s^{\mathrm{ADCP}} t_{i,i+1} \quad , \tag{A.25}$$

where $t_{i,i+1}$ is the traveling time of a signal (twice the distance $s_{i,i+1}$) and the ADCP calculated speed of sound c_s^{ADCP}. The traveling time

$$t_{i,i+1} = \frac{2 s_{i,i+1}}{c_{s,(i,i+1)}} \tag{A.26}$$

is the observable, which is the result of a sound moving the unknown distance $2s_{i,i+1}$ with an unknown velocity $c_{s,(i,i+1)} = c_s(T, S, P)$ (function of temperature, salinity and pressure). Using equation (A.25) and (A.26), the correct distance can be written as a function of the ADCP distance:

$$s_{i,i+1} = \frac{c_{s,(i,i+1)}}{c_s^{\mathrm{ADCP}}} s_{i,i+1}^{\mathrm{ADCP}} \quad . \tag{A.27}$$

The left hand side of equation (A.27) can be replaced by $s_{i,i+1} = z_i^{\mathrm{ADCP}} - z_{i+1,\mathrm{new}}^{\mathrm{ADCP}}$ and together with (A.24) equation (A.27) can be easily rewritten into

$$z_{i+1,\mathrm{new}}^{\mathrm{ADCP}} = -\frac{c_{s,(i,i+1)}}{c_s^{\mathrm{ADCP}}} \left(z_i^{\mathrm{ADCP}} - z_{i+1}^{\mathrm{ADCP}} \right) + z_i^{\mathrm{ADCP}} \tag{A.28}$$

to get the corrected z bin depth $z_{i+1,\mathrm{new}}^{\mathrm{ADCP}}$. Afterwards, all z bins that are below $z_{i+1,\mathrm{new}}^{\mathrm{ADCP}}$ were adjusted by the distance $\Delta z = z_{i+1,\mathrm{new}}^{\mathrm{ADCP}} - z_{i+1}^{\mathrm{ADCP}}$. Iteratively, this procedure is performed for every z bin, see also figure A.1 .
The speed of sound values, calculated from MSS measurements, were averaged between the currently considered z bins for every iteration as shown in the sketch (fig. A.1). A few technical details are mentioned in the following notes:

- The $2\,\mathrm{min}$ averaged ADCP data and the MSS profiles are not measured simultaneously. That is why the speed of sound velocities of the ADCP neighboring MSS profile were interpolated to the ADCP time.
- The ADCP data before (after) the first (last) MSS profile is corrected by using the first (last) MSS profile of the MSS transect.
- Vertical ADCP and MSS profiles have different length. If no MSS data is available near the surface (bottom), a averaged speed of sound value is calculated based on the first (last) MSS data of the profile.

The procedure is performed for the VMADCP and the TLADCP separately, hence, leading to different bottom depths for VMADCP and TLADCP. The TLADCP data is shifted vertically to fit to the VMADCP bottom in order to correct for this difference.

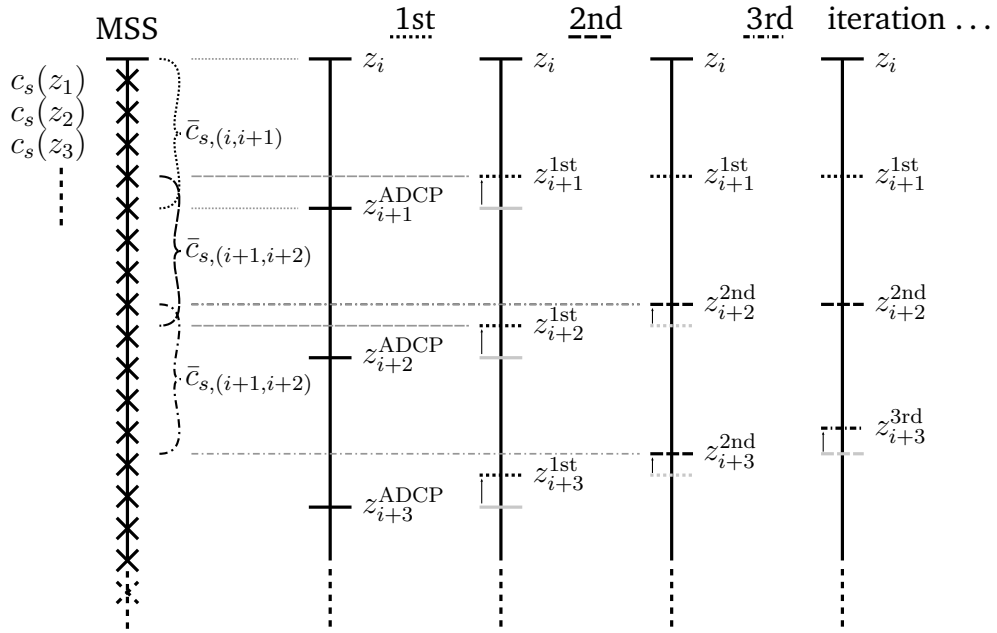

Figure A.1.: On the left: MSS profile with a speed of sound c_s for MSS z bin (cross). Besides the measured ADCP profile with velocity values at every z bin. During the first iteration, all c_s values inside the dotted curly bracket are averaged and used to correct the distance between z_i and z_{i+1}^{ADCP}. Afterwards, all z-bins below are shifted by the same distance. As a next step the distance between the already shifted z-bins z_{i+1}^{1st} and z_{i+2}^{1st} is corrected as described before, starting with averaging c_s values covered by the dashed curly bracket. The iteration ends if the bottom bin of the ADCP is reached.

A.3. Discussion of unresolved near bottom dissipation

The vertical integral of the dissipation rates in the bottom boundary layer (BBL) based on microstructure data generally underestimates the correct value because the sensor protection cage leads to a near-bottom data gap of $9\,\mathrm{cm}$. Further, an automatic routine is used to determine the bottom. At first a rough estimate of the bottom is made with the help of the pressure sensor. The down cast is cut as soon as the pressure stays constant. This profile still contains the sinking into the ground for muddy conditions. Therefore, as a next step, the last section of the acceleration sensor is analyzed. A second estimate of the bottom is made by determining the value that exceed 6 times the root mean square of the acceleration data. This second estimate would be fine for rocky conditions, but cuts the data some centimeters below the bottom for muddy conditions. To solve this the data is cut a little bit above. This leads to a further gap in the data of $6\,\mathrm{cm}$ in the worst case. Both data gaps results in a height of approximately $15\,\mathrm{cm}$ for rocky underground.

The validity of the law of the wall (LOW) is assumed near the boundary in order to estimate dissipation rates in the first centimeters above the bottom. According to the LOW, the dissipation rate is

$$\varepsilon_{\mathrm{LOW}}(h_{ab}) = \frac{u_*^3}{\kappa(h_{ab}+h_0)} \quad , \tag{A.29}$$

where the friction velocity u_*, the von Kármán constant κ, the height above bottom h_{ab} and the roughness parameter h_0 are introduced.
The mean dissipation rate of a vertical bin, which has a height of Δh, is defined as

$$\frac{1}{\Delta h}\int_{h_{ab}-\Delta h/2}^{h_{ab}+\Delta h/2} \varepsilon(z)\,\mathrm{d}z \equiv \overline{\varepsilon}(h_{ab}) \quad . \tag{A.30}$$

Both dissipation rates $\varepsilon_{\mathrm{LOW}}(h_{ab})$ and $\overline{\varepsilon}(h_{ab})$ are approximately equal for a bin height of 0.5 m as long as the comparison starts some centimeters above the bottom. It should be noted that the determination of the bin averaged dissipation rate for the dataset is based on integrated shear spectra followed by averaging to get 0.5 m bins. This routine is different to A.30. Nevertheless, the dissipation rates in the BBL should be representative. Furthermore, they should be able to reproduce bin averaged dissipation rates in the BBL. The vertical integrated dissipation rate E is given by

$$E(h_a) = \int_0^{h_a} \varepsilon_{\mathrm{LOW}}\,\mathrm{d}h_{ab} = \frac{u_*^3}{\kappa}\ln\left(X(h_a)\right) \qquad \text{with } X(h_a) = \frac{h_a+h_0}{h_0} \tag{A.31}$$

for an arbitrary height h_a in the LOW bottom boundary layer. While comparing the vertical integrated dissipation rates for a near bottom unresolved distance h_{unres} to the vertical integrated dissipation rate of the whole LOW bottom boundary layer characterized by the height h_{Lbbl}, it leads to

$$\frac{E(h_{\mathrm{unres}})}{E(h_{\mathrm{Lbbl}})} = \frac{\ln\left(X(h_{\mathrm{unres}})\right)}{\ln\left(X(h_{\mathrm{Lbbl}})\right)} \quad . \tag{A.32}$$

In the case of an unresolved $15\,\mathrm{cm}$ data gap above the bottom, a roughness parameter of $1\times10^{-3}\,\mathrm{m}$ and a LOW bottom boundary layer of $1\,\mathrm{m}$ (or $2\,\mathrm{m}$) the unresolved centimeters were responsible for 73 % (or 66 %) of the whole LOW bottom boundary layer dissipation.

Bibliography

J. P. Antenucci and J. Imberger. Energetics of long internal gravity waves in large lakes. *Limnol. Oceanogr.*, 46(7):1760–1773, 2001. doi: 10.4319/lo.2001.46.7.1760.

J. R. Apel. *Principles of Ocean Physics*, volume 38 of *International Geophysics Series*. Academic Press, London, 4 edition, 1995.

L. Arneborg. Mixing efficiencies in patchy turbulence. *J. Phys. Oceanogr.*, 32(5):1496–1506, 2002.

L. Arneborg, V. Fiekas, L. Umlauf, and H. Burchard. Gravity current dynamics and entrainment: A process study based on observations in the Arkona Basin. *J. Phys. Oceanogr.*, 37(8):2094–2113, 2007. doi: 10.1175/JPO3110.1.

W. Balzer. Organic-Matter Degradation and Biogenic Element Cycling in a Nearshore Sediment (Kiel-Bight). *Limnol. Oceanogr.*, 29(6):1231–1246, 1984.

G. K. Batchelor. *The theory of homogeneous turbulence*. Cambridge university press, 1953.

J. Becherer and L. Umlauf. Boundary mixing in lakes. 1. Modeling the effect of shear-induced convection. *J. Geophys. Res.*, 116:C10017, 2011. doi: 10.1029/2011JC007119.

S. Bergström and B. Carlsson. RIVER RUNOFF TO THE BALTIC SEA - 1950-1990. *Ambio*, 23(4-5):280–287, 1994.

C. Bluteau, N. Jones, and G. Ivey. Turbulent mixing efficiency at an energetic ocean site. *J. Geophys. Res.*, 118(9):4662–4672, 2013. doi: 10.1002/jgrc.20292.

D. Bouffard and L. Boegman. A diapycnal diffusivity model for stratified environmental flows. *Dyn. Atmos. Oceans*, 61-62:14–34, JUN 2013. doi: 10.1016/j.dynatmoce.2013.02.002.

J. A. Brearley, K. L. Sheen, A. C. N. Garabato, D. A. Smeed, and S. Waterman. Eddy-Induced Modulation of Turbulent Dissipation over Rough Topography in the Southern Ocean. *Journal of Physical Oceanography*, 43(11):2288–2308, 2013. doi: 10.1175/JPO-D-12-0222.1.

I. Bychkova, S. Viktorov, and D. Shumakher. The relationship between large-scale atmospheric circulation and processes involved in the origin of coastal upwelling in the Baltic Sea(O sviazi krupnomasshtabnoi atmosfernoi tsirkuliatsii i protsessov vozniknoveniia pribrezhnogo apvellinga v Baltiiskom more). *Meteorologiia i Gidrologiia*, pages 91–98, 1988.

J. R. Carpenter, E. W. Tedford, E. Heifetz, and G. A. Lawrence. Instability in Stratified Shear Flow: Review of a Physical Interpretation Based on Interacting Waves. *Applied Mechanics Reviews*, 64(6):061001, 2011. doi: 10.1115/1.4007909.

L. Clément, E. Frajka-Williams, K. L. Sheen, J. A. Brearley, and A. C. N. Garabato. Generation of Internal Waves by Eddies Impinging on the Western Boundary of the North Atlantic. *J. Phys. Oceanogr.*, 46(4):1067–1079, 2016. doi: 10.1175/JPO-D-14-0241.1.

G. T. Csanady. Large-scale motion in the Great Lakes. *J. Geophys. Res.*, 16:4151–4162, 1967.

F. Cyr, D. Bourgault, and P. S. Galbraith. Behavior and mixing of a cold intermediate layer near a sloping boundary. *Ocean Dynamics*, 65(3):357–374, MAR 2015. doi: 10.1007/s10236-014-0799-1.

K. A. Davis and S. G. Monismith. The modification of bottom boundary layer turbulence and mixing by internal waves shoaling on a barrier reef. *J. Phys. Oceanogr.*, 41(11):2223–2241, 2011. doi: 10.1016/j.csr.2012.12.010.

C. de Lavergne, G. Madec, J. L. Sommer, A. J. G. Nurser, and A. C. N. Garabato. The Impact of a Variable Mixing Efficiency on the Abyssal Overturning. *J. Phys. Oceanogr.*, 46(2):663–681, 2016. doi: 10.1175/JPO-D-14-0259.1.

W. K. Dewar. A fishy mix. *Nature*, 460(7255):581–582, 2009. doi: 10.1038/460581a.

J. Dunckley, J. Koseff, J. Steinbuck, S. Monismith, and A. Genin. Comparison of mixing efficiency and vertical diffusivity models from temperature microstructure. *J. Geophys. Res.*, 117(C10), 2012. doi: 10.1029/2012JC007967.

R. Feistel and S. Feistel. Die Ostsee als thermodynamisches System. *Irreversible Prozesse und Selbstorganisation*, page 79, 2006.

R. Feistel, G. Nausch, and E. Hagen. Unusual Baltic inflow activity in 2002-2003 and varying deep-water properties. *Oceanologia*, 48(S):21–35, 2006.

R. Feistel, G. Nausch, and N. Wasmund, editors. *State and Evolution of the Baltic Sea, 1952-2005. A detailed 50-year survey of meteorology and climate, physics, chemistry, biology, and marine environment*. Wiley-Interscience, Hoboken, NJ, USA, 2008.

S. Feistel, R. Feistel, D. Nehring, W. Matthäus, G. Nausch, and M. Naumann. Hypoxic and anoxic regions in the Baltic Sea. *Meereswiss. Ber.*, 100, 2016.

W. Fennel. Inertial waves and inertial oscillations in channels. *Cont. Shelf Res.*, 9(5): 403–426, 1989. doi: 10.1016/0278-4343(89)90007-1.

W. Fennel and H. U. Lass. *Analytical Theory of Forced Oceanic Waves*. Akademie-Verlag, Berlin, 1989.

W. Fennel, H. Radtke, M. Schmidt, and T. Neumann. Transient upwelling in the central Baltic Sea. *Cont. Shelf Res.*, 30(19):2015–2026, 2010. doi: 10.1016/j.csr.2010.10.002.

I. Fer. Scaling turbulent dissipation in an Arctic fjord. *Deep-Sea Res. II*, 53(1–2):77–95, 2006. doi: 10.1016/j.dsr2.2006.01.003.

I. Fer and K. Widell. Early spring turbulent mixing in an ice-covered Arctic fjord during transition to melting. *Cont. Shelf Res.*, 27:1980–1999, 2007. doi: 10.1016/j.csr.2007.04.003.

C. Garrett. Comment on 'Some evidence for boundary mixing in the deep ocean' by Laurence Armi. *J. Geophys. Res.*, 84(C8):5095–5096, 1979. doi: 10.1029/JC084iC08p05095.

C. Garrett. Marginal mixing theories. *Atmosphere-Ocean*, 29(2):313–339, 1991.

T. Gerkema, J. T. F. Zimmerman, L. R. M. Maas, and H. van Haren. Geophysical and astrophysical fluid dynamics beyond the traditional approximation. *Reviews of Geophysics*, 46(2):RG2004, 2008. doi: 10.1029/2006RG000220.

M. C. Gregg. Scaling turbulent dissipation in the thermocline. *J. Geophys. Res.*, 94 (C7):9686–9698, 1989. doi: 10.1029/JC094iC07p09686.

HELCOM. Environment of the Baltic Sea area 1994-1998. *Baltic Sea Environment Proceedings*, 82B, 2002.

S. Hille, G. Nausch, and T. Leipe. Sedimentary deposition and reflux of phosphorus (P) in the Eastern Gotland Basin and their coupling with P concentrations in the water column. *Oceanologia*, 47(4):663–679, 2005.

P. Holtermann and L. Umlauf. The Baltic Sea Tracer Release Experiment. 2. Mixing processes. *J. Geophys. Res.*, 117:C01022, 2012. doi: 10.1029/2011JC007445.

P. Holtermann, L. Umlauf, T. Tanhua, O. Schmale, G. Rehder, and J. Waniek. The Baltic Sea Tracer Release Experiment. 1. Mixing rates. *J. Geophys. Res.*, 117:C01021, 2012. doi: 10.1029/2011JC007439.

P. Holtermann, H. Burchard, U. Gräwe, K. Klingbeil, and L. Umlauf. Deep-water dynamics and boundary mixing in a non-tidal stratified basin. A modeling study of Baltic Sea. *J. Geophys. Res.*, 119:1465–1487, 2014. doi: 10.1002/2013JC009483.

L. H. Holthuijsen. *Waves in Oceanic and Coastal Waters:*. Cambridge University Press, Cambridge, 001 2007. doi: 10.1017/CBO9780511618536.

G. N. Ivey and J. Imberger. On the nature of turbulence in a stratified fluid. Part I: The energetics of mixing. *J. Phys. Oceanogr.*, 21:650–658, 1991.

G. N. Ivey, K. B. Winters, and J. R. Koseff. Density stratification, turbulence, but how much mixing? *Annu. Rev. Fluid Mech.*, 40:169–184, 2008. doi: 10.1146/annurev.fluid.39.050905.110314.

P. R. Jackson and C. R. Rehmann. Experiments on Differential Scalar Mixing in Turbulence in a Sheared, Stratified Flow. *J. Phys. Oceanogr.*, 44(10):2661–2680, 2014. doi: 10.1175/JPO-D-14-0027.1.

S. M. Kelly, J. D. Nash, K. I. Martini, M. H. Alford, and E. Kunze. The Cascade of Tidal Energy from Low to High Modes on a Continental Slope. *J. Phys. Oceanogr.*, 42(7):1217–1232, JUL 2012. doi: 10.1175/JPO-D-11-0231.1.

P. K. Kundu and I. M. Cohen. *Fluid Mechanics*. Academic Press, London, UK, 4$^{\text{th}}$ edition, 2008.

P. K. Kundu, S.-Y. Chao, and J. P. McCreary. Transient coastal currents and inertio-gravity waves. *Deep-Sea Res. A*, 30(10):1059–1082, 1983. doi: 10.1016/0198-0149(83)90061-4.

E. Kunze, C. MacKay, E. McPhee-Shaw, K. Morrice, J. Girton, and S. Terker. Turbulent Mixing and Exchange With Interior Waters on Sloping Boundaries. *J. Phys. Oceanogr.*, 42(6):910–927, 2012. doi: 10.1175/JPO-D-11-075.1.

N. Kuzmina, B. Rudels, T. Stipa, and V. Zhurbas. The structure and driving mechanisms of the Baltic intrusions. *J. Phys. Oceanogr.*, 35(6):1120–1137, 2005. doi: 10.1175/JPO2749.1.

K. G. Lamb. Internal Wave Breaking and Dissipation Mechanisms on the Continental Slope/Shelf. *Ann. Rev. Fluid Mech.*, 46(1):231–254, 2014. doi: 10.1146/annurev-fluid-011212-140701.

C. Lappe and L. Umlauf. Efficient boundary mixing due to near-inertial waves in a nontidal basin: Observations from the Baltic Sea. *J. Geophys. Res.*, 121, 2016. doi: 10.1002/2016JC011985.

H.-U. Lass and V. Mohrholz. On the dynamics and mixing of inflowing salt-water in the Arkona Sea. *J. Geophys. Res.*, 108:3042, doi: 10.1029/2002JC001,465, 2003.

H.-U. Lass, H. Prandke, and B. Liljebladh. Dissipation in the Baltic Proper during winter stratification. *J. Geophys. Res.*, 108(C6):3187, 2003. doi:10.1029/2002JC001401.

J. R. Ledwell, E. T. Montgomery, K. L. Polzin, L. C. St. Laurent, R. W. Schmitt, and J. M. Toole. Evidence for enhanced mixing over rough topography in the abyssal ocean. *Nature*, 403(6766):179–182, 2000. doi: 10.1038/35003164.

A. Lehmann and K. Myrberg. Upwelling in the Baltic Sea - A review. *J. Mar. Sys.*, 74 (S, SI):S3–S12, DEC 15 2008. doi: 10.1016/j.jmarsys.2008.02.010. 6th Baltic Sea Science Congress/Joint Meeting of the Baltic Marine Biologists/Baltic Oceanographers/Baltic Sea Geologists, Univ Rostock, Rostock, GERMANY, MAR 19-23, 2007.

A. Lorke, F. Peeters, and A. Wüest. Shear-induced convective mixing in bottom boundary layers on slopes. *Limnol. Oceanogr.*, 50(5):1612–1619, 2005.

J. A. MacKinnon and M. C. Gregg. Near-inertial waves on the New England Shelf: The role of evolving stratification, turbulent dissipation, and bottom drag. *J. Phys. Oceanogr.*, 35(12):2408–2424, 2005.

K. I. Martini, M. H. Alford, E. Kunze, S. M. Kelly, and J. D. Nash. Internal Bores and Breaking Internal Tides on the Oregon Continental Slope. *J. Phys. Oceanogr.*, 43 (1):120–139, JAN 2013. doi: 10.1175/JPO-D-12-030.1.

W. Matthäus and H. Franck. Characteristics of Major Baltic Inflows - A Statistical-Analysis. *Cont. Shelf Res.*, 12(12):1375–1400, DEC 1992. doi: 10.1016/0278-4343(92)90060-W.

H. E. M. Meier. Modeling the pathways and ages of inflowing salt- and freshwater in the Baltic Sea. *Estuarine, Coastal and Shelf Science*, 74(4):610–627, 2007.

H. E. M. Meier, R. Feistel, J. Piechura, L. Arneborg, H. Burchard, V. Fiekas, N. Golenko, N. Kuzmina, V. Mohrholz, C. Nohr, V. Paka, J. Sellschopp, A. Stips, and V. Zhurbas. Ventilation of the Baltic Sea deep water: A brief review of present knowledge from observations and models. *Oceanologia*, 48:133–164, 2006.

V. Mohrholz, M. Naumann, G. Nausch, S. Krueger, and U. Graewe. Fresh oxygen for the Baltic Sea - An exceptional saline inflow after a decade of stagnation. *J. Mar. Sys.*, 148:152–166, AUG 2015. doi: 10.1016/j.jmarsys.2015.03.005.

J. Moum and W. Smyth. Upper ocean mixing processes. *Encyclopedia of Ocean Sciences*, 6:3093–3100, 2001.

J. N. Moum, M. C. Gregg, R.-C. Lien, and M. E. Carr. Comparison of turbulent kinetic energy dissipation rate estimates from two ocean microstructure profilers. *J. Atmos. Ocean. Tech.*, 12(2):346–366, 1995. doi: 10.1175/1520-0426(1995)012.

J. N. Moum, D. R. Caldwell, J. D. Nash, and G. D. Gunderson. Observations of boundary mixing over the continental slope. *J. Phys. Oceanogr.*, 32(7):2113–2130, 2002.

J. N. Moum, A. Perlin, K. Klymak, M. D. Levine, and T. Boyd. Convectively-driven mixing in the bottom boundary layer. *J. Phys. Oceanogr.*, 34(10):2189–2202, 2004. doi: 10.1175/1520-0485(2004)034.

W. H. Munk. Internal waves and small-scale processes. In B. A. Warren and C. Wunsch, editors, *Evolution of Physical Oceanography*, pages 264–291. The MIT Press, Cambridge, MA, USA, 1981.

D. Olbers, J. Willebrand, and C. Eden. *Ocean Dynamics*. Springer, Berlin Heidelberg, 2012.

T. R. Osborn. Estimates of the local rate of vertical diffusion from dissipation measurements. *J. Phys. Oceanogr.*, 10(1):83–89, 1980. doi: 10.1175/1520-0485(1980)010.

T. R. Osborn and C. S. Cox. Oceanic fine structure. *Geophys. Fluid Dyn.*, 3:321–345, 1972.

O. M. Phillips. On Spectra Measured in an Undulating Layered Medium. *J. Phys. Oceanogr.*, 1(1):1–6, 1971. doi: 10.1175/1520-0485(1971)001⟨0001:OSMIAU⟩2.0.CO;2.

O. M. Phillips, J.-H. Shyu, and H. Salmun. An experiment on boundary mixing: Mean circulation and transport rates. *J. Fluid Mech.*, 173:473–499, 1986.

M. Plikshs, M. Kalejs, and G. Grauman. The influence of environmental conditions and spawning stock size on the year-class strength of the eastern Baltic cod. *ICES CM*, 1:22, 1993.

S. B. Pope. *Turbulent Flows*. Cambridge University Press, Cambridge, UK, 2000.

H. Prandke. Microstructure sensors. In H. Z. Baumert, J. H. Simpson, and J. Sündermann, editors, *Marine Turbulence: Theories, Observations and Models*, pages 101–109. Cambridge University Press, Cambridge, UK, 2005.

J. Reissmann, H. Burchard, R. Feistel, E. Hagen, H.-U. Lass, V. Mohrholz, G. Nausch, L. Umlauf, and G. Wieczorek. Vertical mixing in the Baltic Sea and consequences for eutrophication – A review. *Progr. Oceanogr.*, 82(1):47–80, 2009. doi: 10.1016/j.pocean.2007.10.004.

H. Salehipour and W. R. Peltier. Diapycnal diffusivity, turbulent Prandtl number and mixing efficiency in Boussinesq stratified turbulence. *JFM*, 775:464–500, 2015. doi: 10.1017/jfm.2015.305.

H. Schinke and W. Matthäus. On the causes of major Baltic inflows — an analysis of long time series. *Cont. Shelf Res.*, 18:67–97, 1998.

O. Schmale, S. Krause, P. Holtermann, N. C. Power Guerra, and L. Umlauf. Dense bottom gravity currents and their impact on pelagic methanotrophy at oxic/anoxic transition zones. *Geophys. Res. Lett.*, 43(10):5225–5232, 2016. doi: 10.1002/2016GL069032.

K. L. Sheen, J. A. Brearley, A. C. Naveira Garabato, D. A. Smeed, L. S. Laurent, M. P. Meredith, A. M. Thurnherr, and S. N. Waterman. Modification of turbulent dissipation rates by a deep Southern Ocean eddy. *Geophys. Res. Lett.*, 42(9):3450–3457, 2015. doi: 10.1002/2015GL063216.

L. H. Shih, J. R. Koseff, G. N. Ivey, and J. H. Ferziger. Parameterization of turbulent fluxes and scales using homogenous sheared stably stratified turbulence simulations. *J. Fluid Mech.*, 525:193–214, 2005. doi: 10.1017/j.csr.2006.07.004.

W. Smyth, D. Hebert, and J. Moum. Local ocean response to a multiphase westerly wind burst .2. Thermal and freshwater responses. *J. Geophys. Res.*, 101(C10): 22513–22533, OCT 15 1996. ISSN 0148-0227. doi: 10.1029/96JC02006.

A. Stigebrandt. A model for the vertical circulation of the Baltic deep water. *J. Phys. Oceanogr.*, 17(10):1772–1785, 1987. doi: 10.1175/1520-0485(1987)017.

C. P. Summerhayes, D. Kroon, A. Rosell-Mele, R. W. Jordan, H.-J. Schrader, R. Hearn, J. Villanueva, J. O. Grimali, and G. Eglinton. Variability in the Benguela Current upwelling system over the past 70,000 years. *Prog. Oceanogr.*, 35(3):207–251, 1995. doi: 10.1016/0079-6611(95)00008-5.

B. Sutherland. *Internal Gravity Waves*. Cambridge University Press, 2010. ISBN 9780521839150.

H. Tennekes and J. L. Lumley. *A First Course in Turbulence*. MIT Press, Cambridge M.A., USA, 1972.

S. A. Thorpe. *The Turbulent Ocean*. Cambridge University Press, Cambridge, UK, 2005.

J. S. Turner. *Buoyancy Effects in Fluids*. Cambridge at the University Press, 1973.

L. Umlauf and L. Arneborg. Dynamics of rotating shallow gravity currents passing through a channel. Part I: Observation of transverse structure. *J. Phys. Oceanogr.*, 39(10):2385–2401, 2009. doi: 10.1175/2009JPO4159.1.

L. Umlauf and H. Burchard. Diapycnal transport and mixing efficiency in stratified boundary layers near sloping topography. *J. Phys. Oceanogr.*, 41(2):329–345, 2011. doi: 10.1175/2010JPO4438.1.

L. Umlauf, W. D. Smyth, and J. N. Moum. The energetics of bottom Ekman layers during buoyancy arrest. *J. Phys. Oceanogr.*, 45:3099——3117, 2015. doi: 10.1175/JPO-D-15-0041.1.

E. Vahtera, D. J. Conley, B. Gustafsson, H. Kuosa, H. Pitkänen, O. P. Savchuk, T. Tamminen, M. Viitasalo, M. Voss, N. Wasmund, and F. Wulff. Internal ecosystem feedbacks enhance nitrogen-fixing cyanobacteria blooms and complicate management in the Baltic Sea. *AMBIO*, 36(2):186–194, 2007. doi: 10.1579/0044-7447(2007)

36[186:IEFENC]2.0.CO;2.

H. M. van Aken. The onset of seasonal stratification in shelf seas due to differential advection in the presence of a salinity gradient. *Cont. Shelf Res.*, 5:475–485, 1986.

E. M. Van der Lee and L. Umlauf. Internal-wave mixing in the Baltic Sea: Near-inertial waves in the absence of tides. *J. Geophys. Res.*, 116:C10016, 2011. doi: 10.1029/2011JC007072.

E. M. van der Lee and L. Umlauf. Internal-wave mixing in the Baltic Sea: Near-inertial waves in the absence of tides. *J. Geophys. Res.*, 116:C10016, 2011. doi: 10.1029/2011JC007072.

H. Van Haren and L. Gostiaux. High-resolution open-ocean temperature spectra. *J. Geophys. Res.*, 114(C5), 2009. doi: 10.1029/2008JC004967.

H. van Haren, M. Laan, D.-J. Buijsman, L. Gostiaux, M. G. Smit, and E. Keijzer. NIOZ3: Independent Temperature Sensors Sampling Yearlong Data at a Rate of 1 Hz. *IEEE Journal of Oceanic Engineering*, 34(3):315–322, JUL 2009. doi: 10.1109/JOE.2009.2021237.

R. K. Walter, M. E. Squibb, C. B. Woodson, J. R. Koseff, and S. G. Monismith. Stratified turbulence in the nearshore coastal ocean: Dynamics and evolution in the presence of internal bores. *J. Geophys. Res.*, 119(12):8709–8730, 2014. doi: 10.1002/2014JC010396.

N. Wasmund, G. Nausch, L. Postel, Z. Witek, M. Zalewski, S. Gromisz, E. Łysiak-Pastuszak, I. Olenina, R. Kavolyte, A. Jasinskaite, et al. *Trophic status of coastal and open areas of the south-eastern Baltic Sea based on nutrient and phytoplankton data from 1993-1997*. Inst. für Ostseeforschung, 2000.

A. F. Waterhouse, J. A. MacKinnon, J. D. Nash, M. H. Alford, E. Kunze, H. L. Simmons, K. L. Polzin, L. C. S. Laurent, O. M. Sun, R. Pinkel, L. D. Talley, C. B. Whalen, T. N. Huussen, G. S. Carter, I. Fer, S. Waterman, A. C. N. Garabato, T. B. Sanford, and C. M. Lee. Global Patterns of Diapycnal Mixing from Measurements of the Turbulent Dissipation Rate. *J. Phys. Oceanogr.*, 44(7):1854–1872, 2014. doi: 10.1175/JPO-D-13-0104.1.

K. B. Winters, P. N. Lombard, J. J. Riley, and E. A. D'Asaro. Available potential energy and mixing in density-stratified fluids. *J. Fluid Mech.*, 289:115–128, 1995. doi: 10.1017/S002211209500125X.

C. Wunsch and R. Ferrari. Vertical mixing, energy, and the general circulation of the oceans. *Annu. Rev. Fluid Mech.*, 36:281–314, 2004. doi: 10.1146/annurev.fluid.36.050802.122121.

Selbstständigkeitserklärung

Ich versichere hiermit an Eides statt, dass ich die vorliegende Arbeit selbstständig angefertigt und ohne fremde Hilfe verfasst habe, keine außer den von mir angegebenen Hilfsmitteln und Quellen dazu verwendet habe und die den benutzten Werken inhaltlich und wörtlich entnommenen Stellen als solche kenntlich gemacht habe.

Rostock, 26.02.2018